ISSN 1949-8470 (online)

World Journal of *Radiology*

World J Radiol 2012 March 28; 4(3): 63-125

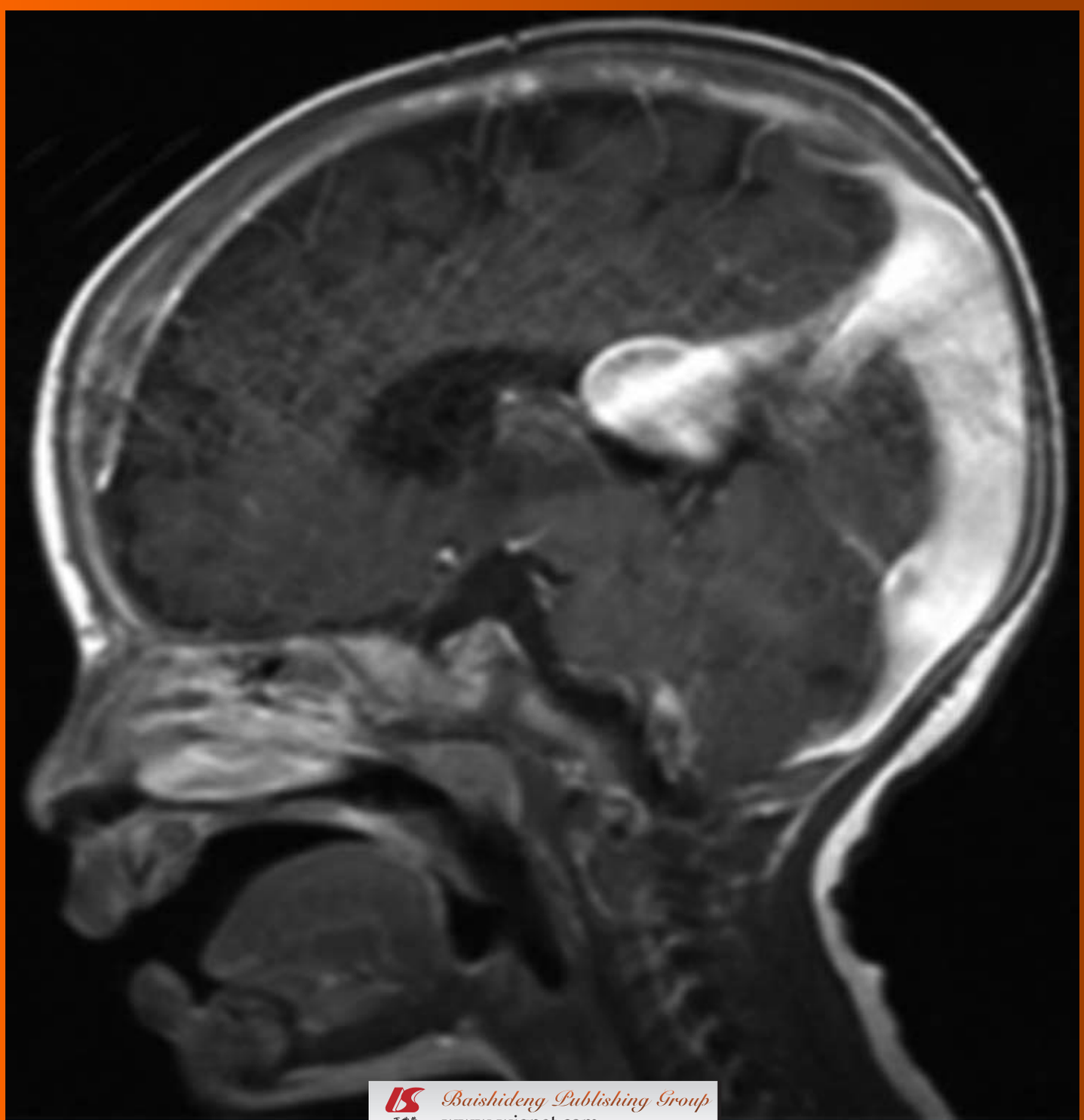

Baishideng Publishing Group
www.wjgnet.com

WJR World Journal of Radiology

A peer-reviewed, online, open-access journal of Radiology

Editorial Board

2009-2013

The *World Journal of Radiology* Editorial Board consists of 319 members, representing a team of worldwide experts in radiology. They are from 40 countries, including Australia (3), Austria (4), Belgium (5), Brazil (3), Canada (9), Chile (1), China (25), Czech (1), Denmark (1), Egypt (4), Estonia (1), Finland (1), France (6), Germany (17), Greece (8), Hungary (1), India (9), Iran (5), Ireland (1), Israel (4), Italy (28), Japan (14), Lebanon (1), Libya (1), Malaysia (2), Mexico (1), Netherlands (4), New Zealand (1), Norway (1), Saudi Arabia (3), Serbia (1), Singapore (2), Slovakia (1), South Korea (16), Spain (8), Switzerland (5), Thailand (1), Turkey (20), United Kingdom (16), and United States (82).

France

Alain Chapel, *Fontenay-Aux-Roses*
Nathalie Lassau, *Villejuif*
Youlia M Kirova, *Paris*
Géraldine Le Duc, *Grenoble Cedex*
Laurent Pierot, *Reims*
Frank Pilleul, *Lyon*
Pascal Pommier, *Lyon*

Germany

Ambros J Beer, *München*
Thomas Deserno, *Aachen*
Frederik L Giesel, *Heidelberg*
Ulf Jensen, *Kiel*
Markus Sebastian Juchems, *Ulm*
Kai U Juergens, *Bremen*
Melanie Kettering, *Jena*
Jennifer Linn, *Munich*
Christian Lohrmann, *Freiburg*
David Maintz, *Münster*
Henrik J Michaely, *Mannheim*
Oliver Micke, *Bielefeld*
Thoralf Niendorf, *Berlin-Buch*
Silvia Obenauer, *Duesseldorf*
Steffen Rickes, *Halberstadt*
Lars V Baron von Engelhardt, *Bochum*
Goetz H Welsch, *Erlangen*

Greece

Panagiotis Antoniou, *Alexandroupolis*
George C Kagadis, *Rion*
Dimitris Karacostas, *Thessaloniki*
George Panayiotakis, *Patras*
Alexander D Rapidis, *Athens*
C Triantopoulou, *Athens*
Ioannis Tsalafoutas, *Athens*
Virginia Tsapaki, *Anixi*
Ioannis Valais, *Athens*

Hungary

Peter Laszlo Lakatos, *Budapest*

India

Anil Kumar Anand, *New Delhi*
Surendra Babu, *Tamilnadu*
Sandip Basu, *Bombay*
Kundan Singh Chufal, *New Delhi*
Shivanand Gamanagatti, *New Delhi*
Vimoj J Nair, *Haryana*
R Prabhakar, *New Delhi*
Sanjeeb Kumar Sahoo, *Orissa*

Iran

Vahid Reza Dabbagh Kakhki, *Mashhad*
Mehran Karimi, *Shiraz*
Farideh Nejat, *Tehran*
Alireza Shirazi, *Tehran*
Hadi Rokni Yazdi, *Tehran*

Ireland

Joseph Simon Butler, *Dublin*

Israel

Amit Gefen, *Tel Aviv*
Eyal Sheiner, *Be'er-Sheva*
Jacob Sosna, *Jerusalem*
Simcha Yagel, *Jerusalem*

Italy

Mohssen Ansarin, *Milan*
Stefano Arcangeli, *Rome*
Tommaso Bartalena, *Imola*
Sergio Casciaro, *Lecce*
Laura Crocetti, *Pisa*
Alberto Cuocolo, *Napoli*
Mirko D'Onofrio, *Verona*
Massimo Filippi, *Milan*
Claudio Fiorino, *Milano*
Alessandro Franchello, *Turin*
Roberto Grassi, *Naples*
Stefano Guerriero, *Cagliari*
Francesco Lassandro, *Napoli*
Nicola Limbucci, *L'Aquila*
Raffaele Lodi, *Bologna*
Francesca Maccioni, *Rome*
Laura Martincich, *Candiolo*
Mario Mascalchi, *Florence*
Roberto Miraglia, *Palermo*
Eugenio Picano, *Pisa*
Antonio Pinto, *Naples*
Stefania Romano, *Naples*
Luca Saba, *Cagliari*
Sergio Sartori, *Ferrara*
Mariano Scaglione, *Castel Volturno*
Lidia Strigari, *Rome*
Vincenzo Valentini, *Rome*

Japan

Shigeru Ehara, *Morioka*
Nobuyuki Hamada, *Chiba*
Takao Hiraki, *Okayama*
Akio Hiwatashi, *Fukuoka*
Masahiro Jinzaki, *Tokyo*
Hiroshi Matsuda, *Saitama*
Yasunori Minami, *Osaka*
Jun-Ichi Nishizawa, *Tokyo*
Tetsu Niwa, *Yokohama*
Kazushi Numata, *Kanagawa*
Kazuhiko Ogawa, *Okinawa*
Hitoshi Shibuya, *Tokyo*
Akira Uchino, *Saitama*
Haiquan Yang, *Kanagawa*

Lebanon

Aghiad Al-Kutoubi, *Beirut*

Libya

Anuj Mishra, *Tripoli*

Malaysia

R Logeswaran, *Cyberjaya*
Kwan-Hoong Ng, *Kuala Lumpur*

Mexico

Heriberto Medina-Franco, *Mexico City*

Netherlands

Jurgen J Fütterer, *Nijmegen*
Raffaella Rossin, *Eindhoven*
Paul E Sijens, *Groningen*

New Zealand

W Howell Round, *Hamilton*

Norway

Arne Sigmund Borthne, *Lørenskog*

Saudi Arabia

Mohammed Al-Omran, *Riyadh*
Ragab Hani Donkol, *Abha*
Volker Rudat, *Al Khobar*

Serbia

Djordjije Saranovic, *Belgrade*

Singapore

Uei Pua, *Singapore*
Lim CC Tchoyoson, *Singapore*

Slovakia

František Dubecký, *Bratislava*

South Korea

Bo-Young Choe, *Seoul*
Joon Koo Han, *Seoul*
Seung Jae Huh, *Seoul*
Chan Kyo Kim, *Seoul*
Myeong-Jin Kim, *Seoul*
Seung Hyup Kim, *Seoul*
Kyoung Ho Lee, *Gyeonggi-do*
Won-Jin Moon, *Seoul*
Wazir Muhammad, *Daegu*
Jai Soung Park, *Bucheon*
Noh Hyuck Park, *Kyunggi*
Sang-Hyun Park, *Daejeon*
Joon Beom Seo, *Seoul*
Ji-Hoon Shin, *Seoul*
Jin-Suck Suh, *Seoul*
Hong-Gyun Wu, *Seoul*

Spain

Eduardo J Aguilar, *Valencia*
Miguel Alcaraz, *Murcia*
Juan Luis Alcazar, *Pamplona*
Gorka Bastarrika, *Pamplona*
Rafael Martínez-Monge, *Pamplona*
Alberto Muñoz, *Madrid*
Joan C Vilanova, *Girona*

Switzerland

Nicolau Beckmann, *Basel*
Silke Grabherr, *Lausanne*
Karl-Olof Lövblad, *Geneva*
Tilo Niemann, *Basel*
Martin A Walter, *Basel*

Thailand

Sudsriluk Sampatchalit, *Bangkok*

Turkey

Olus Api, *Istanbul*
Kubilay Aydin, *İstanbul*
Işıl Bilgen, *Izmir*
Zulkif Bozgeyik, *Elazig*
Barbaros E Çil, *Ankara*
Gulgun Engin, *Istanbul*
M Fatih Evcimik, *Malatya*
Ahmet Kaan Gündüz, *Ankara*
Tayfun Hakan, *Istanbul*
Adnan Kabaalioglu, *Antalya*
Fehmi Kaçmaz, *Ankara*
Musturay Karcaaltincaba, *Ankara*
Osman Kizilkilic, *Istanbul*
Zafer Koc, *Adana*
Cem Onal, *Adana*
Yahya Paksoy, *Konya*
Bunyamin Sahin, *Samsun*
Ercument Unlu, *Edirne*
Ahmet Tuncay Turgut, *Ankara*
Ender Uysal, *Istanbul*

United Kingdom

K Faulkner, *Wallsend*
Peter Gaines, *Sheffield*
Balaji Ganeshan, *Brighton*
Nagy Habib, *London*
Alan Jackson, *Manchester*
Pradesh Kumar, *Portsmouth*
Tarik F Massoud, *Cambridge*
Igor Meglinski, *Bedfordshire*
Robert Morgan, *London*
Ian Negus, *Bristol*
Georgios A Plataniotis, *Aberdeen*
N J Raine-Fenning, *Nottingham*
Manuchehr Soleimani, *Bath*
MY Tseng, *Nottingham*
Edwin JR **van Beek,** *Edinburgh*
Feng Wu, *Oxford*

United States

Athanassios Argiris, *Pittsburgh*
Stephen R Baker, *Newark*
Lia Bartella, *New York*
Charles Bellows, *New Orleans*
Walter L Biffl, *Denver*
Homer S Black, *Houston*
Wessam Bou-Assaly, *Ann Arbor*
Owen Carmichael, *Davis*
Shelton D Caruthers, *St Louis*
Yuhchyau Chen, *Rochester*
Melvin E Clouse, *Boston*
Ezra Eddy Wyssam Cohen, *Chicago*
Aaron Cohen-Gadol, *Indianapolis*
Patrick M Colletti, *Los Angeles*
Kassa Darge, *Philadelphia*
Abhijit P Datir, *Miami*
Delia C DeBuc, *Miami*
Russell L Deter, *Houston*
Adam P Dicker, *Phil*
Khaled M Elsayes, *Ann Arbor*
Steven Feigenberg, *Baltimore*
Christopher G Filippi, *Burlington*
Victor Frenkel, *Bethesda*
Thomas J **George Jr,** *Gainesville*
Patrick K Ha, *Baltimore*
Robert I Haddad, *Boston*
Walter A Hall, *Syracuse*
Mary S Hammes, *Chicago*
John Hart Jr, *Dallas*
Randall T Higashida, *San Francisco*
Juebin Huang, *Jackson*
Andrei Iagaru, *Stanford*
Craig Johnson, *Milwaukee*
Ella F Jones, *San Francisco*
Csaba Juhasz, *Detroit*
Riyad Karmy-Jones, *Vancouver*
Daniel J **Kelley,** *Madison*
Amir Khan, *Longview*
Euishin Edmund Kim, *Houston*
Vikas Kundra, *Houston*
Kennith F Layton, *Dallas*
Rui Liao, *Princeton*
CM Charlie Ma, *Philadelphia*
Nina A Mayr, *Columbus*
Thomas J Meade, *Evanston*
Steven R **Messé,** *Philadelphia*
Nathan Olivier Mewton, *Baltimore*
Feroze B Mohamed, *Philadelphia*
Koenraad J Mortele, *Boston*
Mohan Natarajan, *San Antonio*
John L Nosher, *New Brunswick*
Chong-Xian Pan, *Sacramento*
Dipanjan Pan, *St Louis*
Martin R Prince, *New York*
Reza Rahbar, *Boston*
Carlos S Restrepo, *San Antonio*
Veronica Rooks, *Honolulu*
Maythem Saeed, *San Francisco*
Edgar A Samaniego, *Palo Alto*
Kohkan Shamsi, *Doylestown*
Jason P Sheehan, *Charlottesville*
William P Sheehan, *Willmar*
Charles Jeffrey Smith, *Columbia*
Monvadi B Srichai-Parsia, *New York*
Dan Stoianovici, *Baltimore*
Janio Szklaruk, *Houston*
Dian Wang, *Milwaukee*
Jian Z Wang, *Columbus*
Shougang Wang, *Santa Clara*
Wenbao Wang, *New York*
Aaron H Wolfson, *Miami*
Gayle E Woloschak, *Chicago*
Ying Xiao, *Philadelphia*
Juan Xu, *Pittsburgh*
Benjamin M Yeh, *San Francisco*
Terry T Yoshizumi, *Durham*
Jinxing Yu, *Richmond*
Jianhui Zhong, *Rochester*

WJR World Journal of Radiology

Contents

Monthly Volume 4 Number 3 March 28, 2012

World Journal of Radiology
Volume 4 Number 3 March 28, 2012

Contents

NAME OF JOURNAL
World Journal of Radiology

ISSN
ISSN 1949-8470 (online)

LAUNCH DATE
December 31, 2009

FREQUENCY
Monthly

EDITING
Editorial Board of *World Journal of Radiology,*
Room 903, Building D, Ocean International Center,
No. 62 Dongsihuan Zhonglu, Chaoyang District,
Beijing 100025, China
Telephone: +86-10-59080039
Fax: +86-10-85381893
E-mail: wjr@wjgnet.com
http://www.wjgnet.com

EDITOR-IN-CHIEF
Filippo Cademartiri, MD, PhD, FESC, FSCCT, Professor, Cardio-Vascular Imaging Unit-Giovanni XXIII Hospital, Via Giovanni XXIII, 7-31050-Monastier di Treviso (TV), Italy

EDITORIAL OFFICE
Jian-Xia Cheng, Director
World Journal of Radiology
Room 903, Building D, Ocean International Center,
No. 62 Dongsihuan Zhonglu, Chaoyang District,
Beijing 100025, China
Telephone: +86-10-59080039
Fax: +86-10-85381893
E-mail: wjr@wjgnet.com
http://www.wjgnet.com

PUBLISHING
Baishideng Publishing Group Co., Limited,
Room 1701, 17/F, Henan Building,
No.90 Jaffe Road, Wanchai, Hong Kong, China
Fax: +852-31158812
Telephone: +852-58042046

PUBLICATION DATE
March 28, 2012

INSTRUCTIONS TO AUTHORS
Full instructions are available online at http://www.wjgnet.com/1949-8470/g_info_20100316162358.htm.

ONLINE SUBMISSION
http://www.wjgnet.com/1949-8470office

World Journal of Radiology

Online Submissions: http://www.wjgnet.com/1949-8470office
wjr@wjgnet.com
doi:10.4329/wjr.v4.i3.63

World J Radiol 2012 March 28; 4(3): 63-74
ISSN 1949-8470 (online)

EDITORIAL

Magnetic resonance diffusion-perfusion mismatch in acute ischemic stroke: An update

Feng Chen, Yi-Cheng Ni

Feng Chen, Yi-Cheng Ni, Department of Radiology, Catholic University of Leuven, Campus Gasthuisberg, Herestraat 49, 3000 Leuven, Belgium
Feng Chen, Department of Radiology, Zhongda Hospital, Southeast University, Nanjing 210009, Jiangsu Province, China
Author contributions: Chen F contributed to the concepts, study design, literature research, data acquisition, data analysis and interpretation, manuscript drafting and revision, and final approval of the version to be published; Ni YC contributed to the literature analysis and interpretation, manuscript drafting and revision, and final approval of the version to be published.
Correspondence to: Feng Chen, MD, PhD, Department of Radiology, Gasthuisberg, University of Leuven, Herestraat 49, Box 7003, 3000 Leuven, Belgium. chenfengbe@yahoo.com.cn
Telephone: +32-16-330165 Fax: +32-16-343765
Received: September 6, 2011 Revised: February 22, 2012
Accepted: March 1, 2012
Published online: March 28, 2012

Abstract

The concept of magnetic resonance perfusion-diffusion mismatch (PDM) provides a practical and approximate measure of the tissue at risk and has been increasingly applied for the evaluation of hyperacute and acute stroke in animals and patients. Recent studies demonstrated that PDM does not optimally define the ischemic penumbra; because early abnormality on diffusion-weighted imaging overestimates the infarct core by including part of the penumbra, and the abnormality on perfusion weighted imaging overestimates the penumbra by including regions of benign oligemia. To overcome these limitations, many efforts have been made to optimize conventional PDM. Various alternatives beyond the PDM concept are under investigation in order to better define the penumbra. The PDM theory has been applied in ischemic stroke for at least three purposes: to be used as a practical selection tool for stroke treatment; to test the hypothesis that patients with PDM pattern will benefit from treatment, while those without mismatch pattern will not; to be a surrogate measure for stroke outcome. The main patterns of PDM and its relation with clinical outcomes were also briefly reviewed. The conclusion was that patients with PDM documented more reperfusion, reduced infarct growth and better clinical outcomes compared to patients without PDM, but it was not yet clear that thrombolytic therapy is beneficial when patients were selected on PDM. Studies based on a larger cohort are currently under investigation to further validate the PDM hypothesis.

Key words: Diffusion; Ischemic; Magnetic resonance imaging; Mismatch; Penumbra; Perfusion; Stroke

Peer reviewer: Rivka R Colen, Dr., Department of Radiology, Brigham and Women's Hospital/Harvard Medical School, 150 Brookline Ave Apt 703, Boston, MA 02215, United States

Chen F, Ni YC. Magnetic resonance diffusion-perfusion mismatch in acute ischemic stroke: An update. *World J Radiol* 2012; 4(3): 63-74 Available from: URL: http://www.wjgnet.com/1949-8470/full/v4/i3/63.htm DOI: http://dx.doi.org/10.4329/wjr.v4.i3.63

INTRODUCTION

The concept of ischemic penumbra was originally introduced by Astrup *et al*[1] in 1981, and was defined as an area of reduced cerebral blood flow (CBF) with electrical failure but preserved ion homeostasis and transmembrane electrical potentials. Since then, some other definitions for the ischemic penumbra have been proposed based on energy metabolism, CBF thresholds and protein synthesis[2]. Because the target of thrombolytic therapy in acute stroke is the brain tissue at risk of infarction, the most clinically relevant definition of the penumbra indicates the ischemic tissue but still viable and salvageable if local perfusion is efficiently restored[3,4]. It is widely acknowl-

edged that the mismatch of abnormality volume between perfusion-weighted imaging (PWI) and diffusion-weighted imaging (DWI) of magnetic resonance imaging (MRI), has previously and frequently been applied as an imaging equivalent of the ischemic penumbra[5,6]. The concept of perfusion-diffusion mismatch (PDM) provides a practical and approximate measure of the tissue at risk and has been increasingly applied for the evaluation of acute stroke in animals[7-10] and patients[3,4,6,11].

However, this conventional PDM has been challenged[3,12] by recent studies. It has been evolved into the conviction that PDM does not optimally define the ischemic penumbra. Sufficient data have demonstrated that early abnormality on DWI overestimates the infarct core by including part of the penumbra; and the visible lesion on PWI overestimates the penumbra by including regions of benign oligemia[4,12-14], in which the mild reductions in tissue perfusion do not actually place the tissue at risk[4] (Figure 1). This is reflected in clinical results, where the area of final infarction is normally smaller than the maximum perfusion deficit from PWI[15].

OPTIMAL DEFINITION OF PERFUSION-DIFFUSION MISMATCH

Identification of the PDM is believed to be of considerable therapeutic importance and provides a guideline in patient triage for thrombolytic therapy[16,17]. However, there exist fundamental controversies in defining a PDM. For instance, there is a lack of consensus regarding what constitute the pairs of mismatch[18,19] and which PWI-derived parameter best defines the hypoperfused region or predicts lesion growth[11,19-23].

Some authors suggested that cerebral blood volume (CBV) or CBF is the most reliable parameter to predict final infarct size[20,24-26]. However, a recent meta-analysis reported varied CBF thresholds for discrimination between infarct core, penumbra and oligemia[27]. Although it has been accepted by most imaging groups that a parameter from the time domain is the most accurate, there is still no agreement as to which is superior, i.e., time to peak (TTP)[21,22,28] or mean transit time (MTT)[11,18,19,29-31]. However, both semiquantitative TTP and MTT tend to overestimate the ischemic lesion volume because of collateral flow[32,33].

Technically, there are two methods to measure the PDM. One method is to visually rate the PWI-derived parametric maps and DWI as generated by commercial MRI console software. Another method is to quantify the PWI maps and DWI by offline postprocessing based on region-of-interest volumetric calculation. In this quantitative approach, PDM is defined as a ratio of perfusion: diffusion lesion volume of > 1.2, or as a difference of > 10-50 mL volumes of abnormality between PWI and DWI[34-36]. Some researchers considered that qualitative visual evaluation of PDM performed equally with the quantitative PDM measurements. But Campbell *et al*[36] reported that the visual assessment of PDM at console is insufficiently reliable for use in clinical trials due to the great interobserver variability. In addition, Butcher *et al*[37,38] found that variability in planimetric PDM measurements arises primarily from differences in PWI volume assessment; because the perfusion-derived readouts may vary greatly due to different examiners and kynatic models applied[38]. Ma *et al*[39] also found that volumetric analysis consistently underestimates the PDM volume. All those mentioned reasons combine to make visual PDM substantially different to quantitative PDM. Better ways are sought to improve the measurement of PDM. These include the semi-automated[40] or fully automated processing of PDM with dedicated software[41-43] and the more precise co-registration method for DWI and PWI[35,39,44].

Although the new concept of PDM has been proposed, currently there is a lack of reliable measures to separate the penumbra part from infarct core on DWI and the benign oligemia from real penumbra on PWI in clinical practice. Many efforts have been made to optimize conventional PDM as described below in order to better define the penumbra.

Serial measurements of perfusion-diffusion mismatch

Since the PDM is strictly time dependent, the moment to acquire PWI is particularly critical in the clinic[45,46]. It has been shown that the mismatch may exist up to 3 d or even later in patients after symptom onset[47-51] and most cases of PDM (75%) occurred within the first 6 h after stroke onset in patients[47]. Recent clinical studies indicated that the presence and extent of reperfusion and collaterals were key factors affecting the evolution of PDM patterns and outcomes of patient with acute stroke[47,52-56]. Therefore, serial measurements of PDM have been proved to be useful in real-time monitoring of PDM evolution, and might be beneficial for rescuing more stroke patients[48-50,57,58].

Threshold method for defining perfusion-diffusion mismatch

Recent studies suggested that using a threshold derived from PWI or DWI appeared to provide more accurate discrimination between benign oligemia and penumbra or reversible lesion and infarct core[27,59-61]. Rohi *et al*[62] reported that cutoff values of relative CBF < 0.59 and MTT > 1.63 were optimal in distinguishing the benign oligemia and real penumbra. Oppenheim *et al*[63] suggested that the apparent diffusion coefficient (ADC) values best excluded penumbra ($7.82 \pm 0.82\times10^{-4}$ mm^2/s) from benign oligemia ($8.23 \pm 0.41\times10^{-4}$ mm^2/s). Prospective investigations are currently undergoing to validate these thresholding techniques with automated software programs[59].

Other approaches for defining perfusion-diffusion mismatch

Many other approaches have been tried to optimize the definition of PDM. Chen *et al*[64] presented initial experiences of utilizing arterial spin labeling PWI in pediatric ischemic stroke patients. Tsang *et al*[65] reported that sodium intensity remains unchanged in PDM tissue, indicating preservation of ionic homeostasis. Based on intravoxel

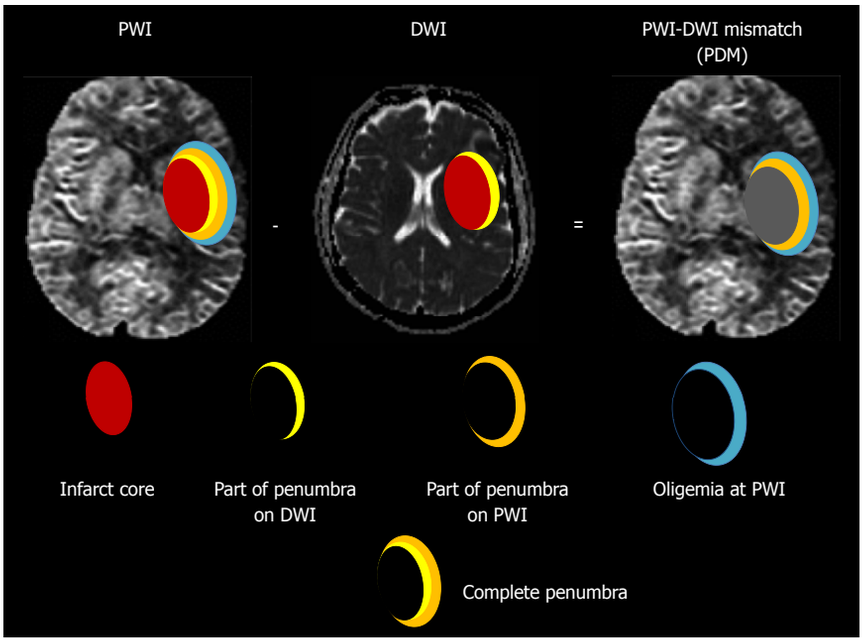

Figure 1 Modern concept of ischemic penumbra. Early abnormality on diffusion weighted imaging (DWI) equals the infarct core plus a part of the tissue at risk (penumbra); and the perfusion deficiency on perfusion weighted imaging (PWI) includes the infarct core plus penumbra and region of benign oligemia. PWI-DWI mismatch (PDM) does not optimally define the ischemic penumbra.

incoherent motion MRI, Suzuki *et al*[66] used an independent component analysis, a higher-order statistical signal processing technique, to obtain a perfusion map from a set of diffusion-weighted images based on assumed difference in ADC values. In this way, the PDM can be identified without the PWI data.

POTENTIAL ALTERNATIVES FOR PERFUSION-DIFFUSION MISMATCH

pH-weighted imaging-perfusion-weighted imaging or diffusion-weighted imaging mismatch

According to Astrup's classic definition of penumbra, the anaerobic metabolism and the formation of lactate lead to a decrease in pH in the area of the penumbra. Sun *et al*[67,68] detected the pH-dependent amide proton transfer between endogenous mobile proteins/peptides and tissue water, and obtained pH-weighted imaging (pHWI) during acute ischemia. This modality allowed them to subdivide the PDM into regions with and without tissue acidosis. It was found that the pHWI-deficit area at 3 h was constant during the hyperacute phase of stroke onset; the outer boundary of the hypoperfused area that shows a decrease in pH without DWI abnormality may better correspond to the classic ischemic penumbra area than the PWI deficit. The PWI-pHWI mismatch would then match to benign oligemia, and the pHWI-DWI mismatch to the minimal penumbral area.

Magnetic resonance thermometry-diffusion-weighted imaging mismatch

Elevated temperatures, or pyrexia, in the body or even in brain tissues are common in acute cerebral ischemic stroke[69,70]. Pyrexia is associated with a worse outcome after stroke, e.g., increased infarct size than normothermia in animal models. In contrast, hypothermia reduced ischemic lesion volume on DWI and may improve functional outcome[71]. Brain temperature (T) can be measured non-invasively with magnetic resonance spectroscopy imaging (MRSI). For each voxel, cerebral temperature can be calculated from the apparent chemical shift of the N-acetylaspartate (NAA) peak, using the following formula: T = 37 ℃ + 100 (NAA_{peak} - 2.035), where a chemical shift of 2.035 ppm was found in healthy control subjects with an assumed brain temperature of 37 ℃. Using this approach, Karaszewski B *et al*[71] found that the tissues were hotter in "potential penumbra" (marginally abnormal on DWI or just outside the edge of the DWI lesion) than the "likely infarct core" (definitely abnormal on DWI). The "likely infarct core", in turn, was hotter than normal brain tissues. Therefore, MRSI provides a promising approach in the study of temperature after stroke and to monitor interventions[69-71].

Based blood oxygen level-dependent magnetic resonance imaging-based penumbra

This is based on the finding that oxygen extraction fraction (OEF) is significantly increased in the ischemic penumbra[72]. Deoxyhemoglobin (deoxy-Hb) can be used as an indicator of OEF that can be visualized by T2*-based blood oxygen level-dependent (BOLD) imaging. Geisler *et al*[73] applied quantitative T2*-based BOLD imaging (T2') in patients with acute stroke. They found that a signal reduction in the T2' images presumably corresponding with an increase of deoxy-Hb was attributable to an increase of OEF. They also detected shortened T2' values adjacent to the ADC lesion in the region later evolving into infarction, which represents the essential penumbra, and a significant T2' signal loss in the region of a benign oligemia. Therefore, this negative BOLD MRI technique provided an additional metabolic parameter in the better description of the ischemic penumbra[74,75].

Positron emission tomography-based estimation of penumbra

For positron emission tomography (PET), penumbra was defined as the region with increased OEF and termed "misery perfusion" for this purpose. Normally, cerebral perfusion was assessed by H2(15)O-PET and tissue damage was estimated by 11C-flumazenil. The determination of absolute values of thresholds for penumbra in patients, however, is difficult since the necessary calculation requires arterial blood sampling. The reported values for the threshold of morphological damage and of the upper limit of penumbra vary considerably (14~22 mL/100 g per minute) by different authors[72]. Studies demonstrated that PET and PDM were related to the tissue with increased OEF as an indicator of penumbra. PWI was limited in estimating flow and yielded values comparable to H2(15)O-PET only in the range between 20 and 30 mL/100 g per minute[76]. In a coregistered PET and DWI study, the characteristic changes of both infarction and penumbra were defined with PET in areas of abnormal DWI[77,78], with a value of OEF > 150% suggesting the real penumbra[60].

PET is still considered the gold standard and is the first line technique employed for detection of penumbra and irreversibly damaged tissue, but it is not a readily available methodology[78,79].

Magnetic resonance angiography-diffusion-weighted imaging mismatch

The magnetic resonance angiography (MRA)-DWI mismatch was defined as an MRA score of 3 (for the intracranial internal carotid artery (ICA) and M1 segment of the MCA, 1 = normal; 2 = reduced flow; and 3 = occlusion) and a DWI lesion volume < 25 mL, or an MRA score of 2 and a DWI lesion volume < 15 mL[80]. Kim *et al*[80] found that the MRA-DWI mismatch was more prevalent in the intracranial large artery atherosclerotic stroke group than in other stroke subtypes. Ma *et al*[81] reported that baseline MRA was helpful in categorizing acute ischemic stroke patients into subgroups and should be used in advance of PDM acquisition, because patients may not need thrombolytic therapy if they do not have initial vessel occlusion found by MRA. Another advantage of baseline MRA is the favorable response in patients with arterial occlusion visualized by MRA to increasing doses of thrombolytic agents such as desmoteplase[82].

Diffusion-weighted imaging - T2W mismatch

It is well accepted that a DWI lesion does not represent the real infarct core because it includes part of the tissue at risk or penumbra. Since the DWI may show initial reduction with no abnormal change on T2W or fluid-attenuated inversion-recovery (FLAIR) images in hyperacute stroke, a DWI-T2W mismatch was proposed to represent the ischemic penumbra. The DWI-T2W mismatch was defined as a hyperintense lesion on DWI (low ADC) with no hyperintense lesion on T2WI or FLAIR, and no hypointense lesion on T1WI. This method may be particularly beneficial to patients with undefined time windows or beyond 3 h after symptom onset and without PWI data[83,84].

However, recent progress in DWI suggested that the reversal of the tissue at risk included in DWI abnormality was uncommon in ischemic stroke patients. The volume of reversed lesion on DWI was small and would rarely affect therapy decisions based on PDM theory[85,86]. Therefore, DWI is generally considered a reliable indicator for predicting ultimate infarction with or without reperfusion[81,85-89].

Clinical-diffusion mismatch

Since MR-perfusion has limited utilities in many hospitals due to technical reasons[90], the clinical-diffusion mismatch (CDM) model was proposed as an alternative method for PDM. The CDM is technically less challenging because it does not require PWI[91]. In order to measure the CDM, Alberta Stroke Programme Early Computed Tomography Score (ASPECTS) methodology was applied to the MRI sequences in an analogous topographical technique as used for computed tomography (CT)[92]. The CDM was defined as a score of National Institute of Health Stroke Score (NIHSS) $\geqslant$ 8 and DWI-ASPECTS $\geqslant$ 8 or DWI (lesion volume) $\leqslant$ 25 mL. It has been suggested that NIHSS $\geqslant$ 8 is a clinical indicator of a large volume of ischemic brain tissue, and had a high rate of early neurological deterioration and lesion growth[93]. However, there was a discrepancy between CDM and PDM[94]. Iwanaga *et al*[95] found no increased benefit from tissue plasminogen activator (tPA) in patients with CDM, because the positive effects of reperfusion were similar in patients with and without CDM.

Computed tomography-derived mismatch

Infarct core measured on CT was usually segmented based on a CBV threshold of 56% relative to the opposite side. A previous study compared DWI and CBV lesion volumes using thresholds of 46%, 56% and 66% of the contralateral normal side as well as a 2 mL/100 g absolute threshold. The results indicated that the DWI and CBV correlation was optimal using the 56% threshold[96]. Another study[97] reported that ischemic penumbra was determined based on a MTT threshold of 150% relative to the contralateral side. Percent volume mismatch was defined as [(MTT - CBV)/CBV] × 100%. In addition to CBV and MTT, some researchers proposed the use of rCBF to calculate the CT mismatch[98].

Instead of using computed tomography perfusion maps (CTP), Wang *et al*[99] suggested the use of CTP source images (CTP-SI) to define a CTP mismatch. Here, the CTP mismatch was defined as a delayed perfusion between arterial phase CTP-SI ASPECTS and venous phase CTP-SI ASPECTS. The presence of such a delayed perfusion can be used as an indicator for thrombolysis.

In a retrospective study, Messé *et al*[100] tested a mismatch between ischemic changes on head CT and clinical examination findings (CT-NIHSS mismatch), but his results did not show any correlation between the CT-NIHSS mismatch and MRI PDM.

APPLICATIONS OF PERFUSION-DIFFUSION MISMATCH

The PDM theory was introduced in the late 1990s[85]. Despite its limitations in imaging ischemic penumbra, this paradigm has been widely used in preclinical research and clinical trials[16,17]. The PDM model combined with other MRI techniques such as T2WI, FLAIR and MRA have been employed for various purposes[12].

First, it was used as a practical selection tool for stroke treatment[101-106]. Only those with appropriate PDM patterns will be enrolled for therapy, like clinical trials of Desmoteplase in Acute Ischemic Stroke Trial (DIAS)[107], Dose Escalation of Desmoteplase for Acute Ischemic Stroke[101], and DIAS 2[104]. However, the results were not repeatable[82,108-110] in those trials, although better outcomes were found with higher doses of desmoteplase corresponding to the frequency of reperfusion.

Second, to test the hypothesis that patients with PDM pattern will benefit from treatment, while those without mismatch pattern will not, all patients were treated no matter their phases and pretreatment PDM patterns[12,111]. Clinical trials like The Diffusion and Perfusion Imaging Evaluation For Understanding Stroke Evolution (DEFUSE) and Echoplanar Imaging Thrombolytic Evaluation Trial (EPITHET) were conducted for this purpose. However, the results were not very straightforward. In DEFUSE, no clear pattern of response was found to reperfusion treatment with tPA between patients with PDM and patient without. In EPITHET, although the infarct growth was smaller in patients treated with tPA, the difference was not statistically significant compared to the controls. Furthermore, the outcomes were better in all patients and PDM patients treated with tPA, but the difference was also not statistically significant[82,85,101,112].

Third, PDM was applied as a surrogate measure for stroke outcome. Some studies suggested that the abnormality from PWI can be used to predict the lesion growth or final infarct volume[113-115]. However, this has been challenged due to the evolving PDM concept[89,116]; because the regions of benign oligemia included in the PWI abnormality did not finally develop into infarction[4,12,68], and patients without PDM were equally likely to have lesion growth as those with PDM and should also be enrolled in acute stroke treatment[89,117]. A reduced volume of PDM can be used as an indicator of improvement of stroke severity in a combined anti-stroke study[89] and of potential for recovery of functions[118]. Since an acute ischemic lesion was detected with PDM in about 60% of patients with transient ischemic attack (TIA), PDM may play a role in the triage of acute TIA and brain infarction[118]. PDM can also be applied as an indication for performing interventional procedures like clot removal therapy by aspiration and extraction[110], urgent carotid artery stenting for acute stroke patients[108], and transluminal balloon angioplasty for patients with cerebral vasospasm[109]. In a report by Heidenreich *et al*[119] the presumptive treatment plan was changed after PDM-based evaluation in 26% (25/97) of patients with hyperacute stroke. Studies also revealed that the relation between the anatomic location and PDM may have some indications for the progression or prognosis in patients with hyperacute and acute stroke. For instance, the ischemia stroke was found to progress and have more severe TTP abnormalities in the central part of the MCA territory including the inferior frontal gyrus, superior temporal gyrus, insula, and underlying hemispheric white matter[120]. The loss of PDM volume (evolving into infarction) was increased in the insula area[120], and target mismatch was more frequent in the cortex with better outcomes if reperfusion was timely established[121]. In addition, the severity of leukoaraiosis was associated with the loss of PDM and seems to be a predictor of infarct growth[122].

MAIN PATTERNS OF PDM AND THEIR CLINICAL RELEVANCE

As the target of thrombolytic therapy of acute stroke, the PDM is normally defined as a mismatch ratio of PWI/DWI $\geqslant$ 1.2, reflecting the presence of clinically significant mismatch[106,123,124]. However, recent studies suggested the use of a larger ratio of 1.8 to 2.6, because a larger mismatch was associated with a higher response rate in the condition of reperfusion therapy[125,126].

Although the PWI/DWI mismatch $\geqslant$ 1.2 is the predominant pattern in PDM discrepancies[47], many other PDM patterns have been recently reported and their relevance to subtypes of stroke has not been fully elucidated[20,47,52,127,128]. Discrepancies between the extent of abnormality on PWI and DWI are supposed to depend predominantly on time from stroke onset to MRI scanning[45,46,52]. The topographic profiles of these PDM patterns were summarized as follows and in Table 1.

Type I, perfusion-weighted imaging > diffusion-weighted imaging

This pattern is the main type (49%-70%) of PDM and defined as the target mismatch[125] or positive mismatch[51] for reperfusion therapy (Figure 2). Bang *et al*[125] reported that this pattern is more common in white patients compared with Asian ethnicity with medium-sized lesions on DWI. This pattern was also defined as the classical type of PDM by Ma *et al*[121,129], i.e., a DWI lesion within a hypoperfused territory on PWI. In their study, a larger mismatch volume in a cortical location was considered an important factor relevant to the classical pattern, and the presence of distal hyperintense vessels on FLAIR (a potential MRI marker for collaterals) was found to be associated with a large PDM[130]. But this classic pattern may evolve into a fragmented non-classical PDM pattern over time (up to 48 h), i.e., the dissociation of PWI and DWI lesions. They even found that the types of PDM patterns have little effect on infarct growth, clinical outcomes and the benefit of thrombolytic agent; this suggests that mismatch topography is less important at least during the hyperacute phase of stroke. An animal study also found that the PDM pattern may have evolved over time from

Table 1 Patterns of discrepancy between perfusion-weighted imaging and diffusion-weighted imaging

	Pattern	Incidence %		Main etiology	Indications	Potential interventions
		< 6 h	Total			
Ⅰ	PWI > DWI[20,47,51-53,114,121,125,127-130,135], target mismatch	57~86	49~70	Large-artery atherosclerosis, cardioembolism, cryptogenic	Larger lesion on PWI and DWI. Part of tissue at risk and oligemia. Infarct may growth without effective therapy. More common in white patients	Reperfusion therapy: Thrombolytic therapy or angioplasty, stenting
Ⅱ	PWI = DWI[20,52,125,131]	~17	~28	Cryptogenic, large-artery atherosclerosis, cardioembolism, lacunar infarction	No additional tissue at risk. Collateral flow limits the infarct volume to that depicted at DWI. Most common in patients with diabetes	Neuroprotection
Ⅲ	PWI < DWI[51,52,114,123,132], inverse mismatch	~29	6~34	Cryptogenic, cardioembolism, large-artery atherosclerosis, lacunar infarction	Smaller lesion on PWI and DWI. Partial reperfusion may occur at the time of MR scan	Neuroprotection
Ⅳ	PWI (-), DWI (+)[47,114,125]	~8	~24	Single small MCA branch occlusion, small subclinical infarct	Full reperfusion may occur or due to collaterals at the time of MR scan. More common in Asian patients	Neuroprotection
Ⅴ	PWI (+), DWI (-)[47,80,128,133,134], total mismatch	~8	~3	Migraine, TIA	Pure perfusion deficit (tissue at risk but not committed to infarction)	Reperfusion therapy
Ⅵ	PWI (-), DWI (-)[20,135]	~14	~18	Migraine, TIA	No abnormality on both PWI and DWI. Normal or hypoperfusion on PET	No interventional therapy
Ⅶ	PWI or DWI > 100 mL[82,112], malignant mismatch			Large-artery atherosclerosis	Poor outcome, strongly associated with reperfusion-related brain hemorrhage	Exclusion of therapy

(+): There is abnormality; (-): No abnormality; PWI: Perfusion weighted imaging; DWI: Diffusion weighted imaging; MCA: Middle cerebral artery; TIA: Transient ischemic attack; PET: Positron emission tomography.

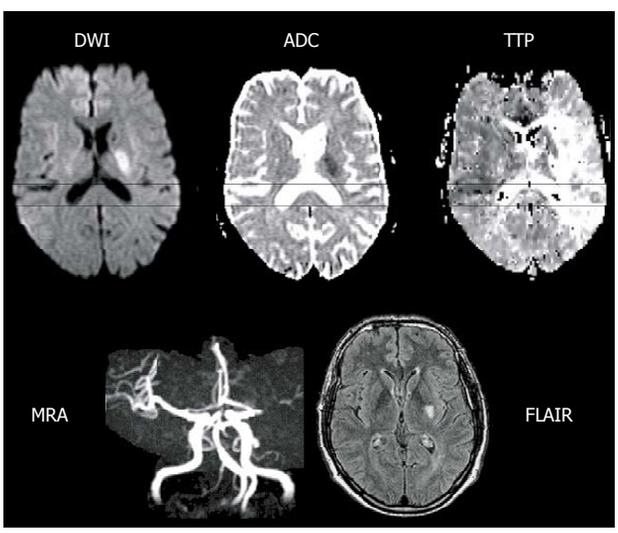

Figure 2 Main pattern of perfusion-diffusion mismatch, perfusion-weighted imaging > diffusion-weighted imaging, in a patient with acute stroke. Extensive area of prolonged time to peak (TTP) and small diffusion-weighted imaging (DWI) lesion in deep middle cerebral artery (MCA) territory, with a complete proximal MCA occlusion on magnetic resonance angiography (MRA) (reprint from Muir KW *et al Lancet Neurol* 2006; 5: 755-68 with permission). ADC: Apparent diffusion coefficient; FLAIR: Fluid-attenuated inversion-recovery.

the so-called classic pattern (PWI > DWI) during initial hours through to a match pattern (PWI = DWI) around 6-12 h to a reverse mismatch (PWI < DWI) at a later time up to 3 d after stroke onset[51].

Type Ⅱ, perfusion-weighted imaging = diffusion-weighted imaging

This match pattern means that no additional tissue at risk or penumbra was found, because collateral flow may limit the infarct core evolving into the hypoperfused area on PWI[131] (Figure 3). Contrary to that, Bang *et al*[125] reported that this no target mismatch was the most common type in patients with diabetes. The possible mechanism may be attributed to the early and longstanding hyperglycemia and increased lactate production. All of these may lead to occlusion of small perforators, collateral failure, impaired autoregulation, and consequent loss of penumbra.

Type Ⅲ, perfusion-weighted imaging < diffusion-weighted imaging

Since the abnormality volume on PWI is smaller than that on DWI, it is considered an inverse or negative mismatch[51]. The mechanism for this pattern may be attributed to the partial reperfusion which occurred at the time of the MRI scan (Figure 4). Fiebach *et al*[123] found that this inverse mismatch was frequent in small subcortical ischemic stroke and infarct core may develop beyond the initial hypoperfusion area. In another study, Ma *et al*[132] found that in 11 of 34 (32%) patients with negative mismatch (PWI < DWI) assessed by the volumetric subtraction technique, all had positive mismatch (PWI > DWI) identified when the more precise coregistration analysis was performed. They named it "hidden mismatch", which provided an explanation for the previous illogical finding that infarct expansion seems to occur even in the presence of inverse mismatch (PWI < DWI). The "hidden mismatch" observation indicated the possible benefit of treatment for patients even with inverse mismatch[51,123,132].

Type Ⅳ, perfusion-weighted imaging (-), diffusion-weighted imaging (+)

This pattern shows only an infarct lesion on DWI with absence of perfusion deficiency on PWI due to single small artery occlusion or presence of small subclinical

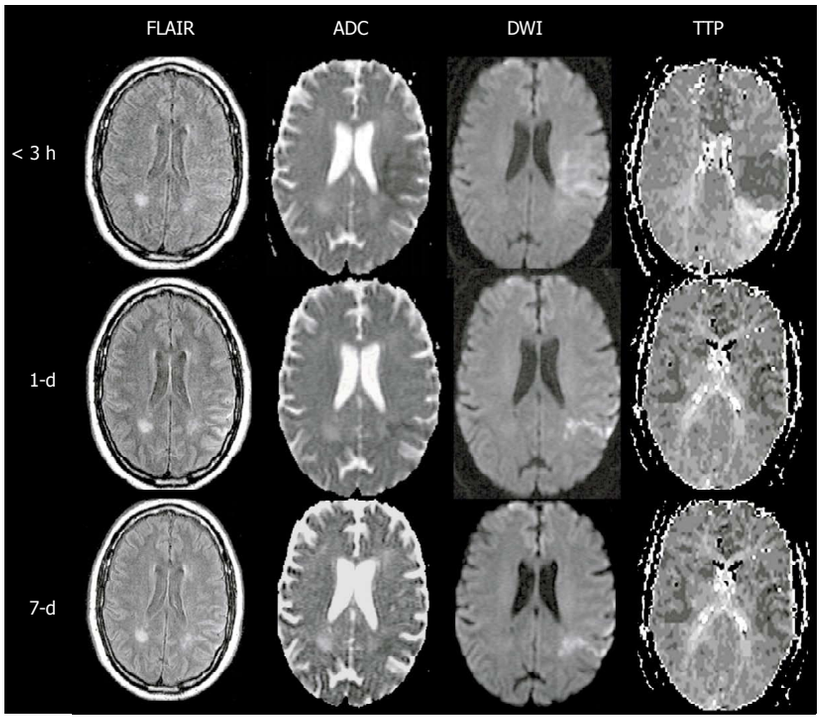

Figure 3 Main pattern of perfusion-diffusion mismatch, perfusion-weighted imaging = diffusion-weighted imaging, in a patient with acute stroke. < 3 h: Fuzzy diffusion-weighted imaging (DWI) lesion in left middle cerebral artery territory matching an area of diminished time to peak, indicating local hyperperfusion and spontaneous recanalization had occurred prior to imaging at 3 h after onset (note the prolonged time to peak at the posterior edge of the DWI lesion, suggesting distal branch occlusion); 1-d: The next day, perfusion has essentially normalized as well as the DWI lesion, save for a narrow posterior streak, suggesting the spontaneous recanalization saved the at-risk tissue from progressing to infarction; 7-d: At day 7, there has been no return of the DWI lesion, indicating the tissue was effectively salvaged (reprint from Muir KW *et al* *Lancet Neurol* 2006; 5: 755-768 with permission). PWI: Perfusion-weighted imaging; ADC: Apparent diffusion coefficient; TTP: Time to peak; FLAIR: Fluid-attenuated inversion-recovery.

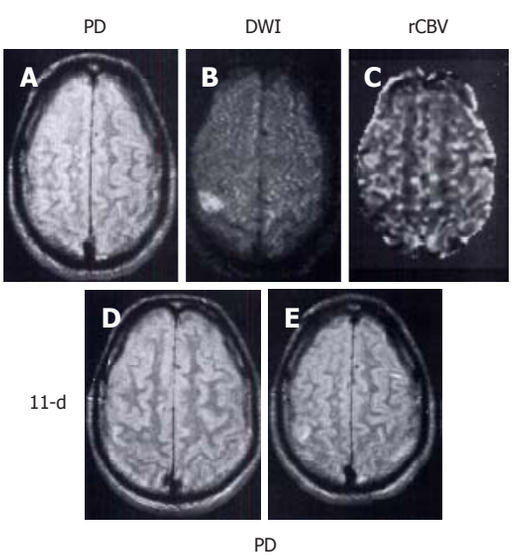

Figure 4 Main pattern of perfusion-diffusion mismatch: perfusion-weighted imaging < diffusion-weighted imaging, in a patient with acute stroke. Patient's left-sided weakness was partially resolved 3 h after the onset of symptoms. A: Proton density (PD) weighted fast spin-echo image shows no abnormality; B: Diffusion-weighted imaging (DWI) shows a focal cortical ischemic abnormality; C: Relative cerebral blood volume (rCBV) map demonstrates a smaller lesion with decreased rCBV compared to the same abnormality as depicted in B; D, E: Follow-up PD images acquired 11 d later show a new tiny hyperintense infarct in the area of initially observed lesion on B and C. Note that the initial DWI lesion is larger than the final infarct volume. The patient's symptoms resolved completely after 2 d (reprint from Sorensen *et al Radiology* 1996; 199: 391-401 with permission).

infarct. This type is more common in Asian patients, because intracranial atherosclerosis and small arterial occlusions were common causes of strokes in Asians and Blacks. Consequently, very small or even absence of the hypoperfusion region was seen in this pattern[125].

Type V, perfusion-weighted imaging (+), diffusion-weighted imaging (-)

This pattern is also termed total mismatch, i.e. negative DWI and extensive perfusion defects. Recent studies seem to suggest that total mismatch does not necessarily progress to infarction, but may suggest stroke pathogenesis and site of current arterial occlusion. Patients with total mismatch usually have a favorable outcome after recanalization with or without thrombolysis. It also provided evidence of brain ischemia in patients with a clinical diagnosis of migraine or TIA[80,133,134].

Type VI, perfusion-weighted imaging (-), diffusion-weighted imaging (-)

In this type, there is no abnormality on both DWI and PWI. This pattern was normally found in patients with migraine headaches. Patients' symptoms were associated with localized or "spreading hypoperfusion" along the cerebral cortex as confirmed by PET, and may be resolved completely within 1-48 h[20,135]. Therefore, the observed hypoperfusion most likely belongs to a type of mild oligemia that cannot even be detected with PWI.

Type VII, perfusion-weighted imaging or diffusion-weighted imaging > 100 mL

The DEFUSE clinical trial defined PWI or DWI volume $\geqslant$ 100 mL as a malignant mismatch. A number of studies indicated that patients with the malignant mismatch pattern were more likely to have a poor outcome (modified Rankin Scale score 5 to 6) with reperfusion than without and were strongly associated with reperfusion-related brain hemorrhage due to the severe ischemic brain and microvessel injury. Exclusion of patients with malignant mismatch could improve the safety and efficacy of reperfusion therapies[82,112].

CONCLUSION

Although the PDM is not yet perfectly matched with the ischemic penumbra, it has been widely recognized as a crude but practical approximation of an imaging equivalent of the pathological ischemic penumbra[5,6,51]. There is still a lack of consensus regarding the best definition and optimal measurement for PDM. Conclusions draw from recent clinical trials including DEFUSE and EPITHET suggested that patients with PDM documented more reperfusion, reduced infarct growth and better clinical outcomes compared to patients without PDM[82,85,125,136,137], but it is not yet clear that thrombolytic therapy is beneficial when patients are selected on PDM[82]. Studies based on a larger cohort are currently under investigation to further validate the PDM hypothesis[82]. Given the limitation of current PDM theory, studies in other potential alternatives or imaging biomarkers beyond the PDM concept may help in the management of ischemic stroke patients[82,85,138].

REFERENCES

1 **Astrup J**, Siesjö BK, Symon L. Thresholds in cerebral ischemia - the ischemic penumbra. *Stroke* 1981; **12**: 723-725
2 **Fisher M**. The ischemic penumbra: identification, evolution and treatment concepts. *Cerebrovasc Dis* 2004; **17** Suppl 1: 1-6
3 **Fisher M, Ginsberg M. Current concepts of the ischemic** penumbra: introduction. *Stroke* 2004; **35** (Suppl 1): **2657-2658**
4 **Kidwell CS**, Alger JR, Saver JL. Evolving paradigms in neuroimaging of the ischemic penumbra. *Stroke* 2004; **35**: 2662-2665
5 **Hoehn M**, Nicolay K, Franke C, van der Sanden B. Application of magnetic resonance to animal models of cerebral ischemia. *J Magn Reson Imaging* 2001; **14**: 491-509
6 **Warach S**. Measurement of the ischemic penumbra with MRI: it's about time. *Stroke* 2003; **34**: 2533-2534
7 **Kohno K,** Hoehn-Berlage M**, Mies G. Relationship between** diffusion-weighted MR images, cerebral blood flow, and energy state in experimental brain infarction. *Magn Reson Imaging* 1995**; 13:** 73-80
8 **Müller TB**, Haraldseth O, Jones RA, Sebastiani G, Godtliebsen F, Lindboe CF, Unsgård G. Combined perfusion and diffusion-weighted magnetic resonance imaging in a rat model of reversible middle cerebral artery occlusion. *Stroke* 1995; **26**: 451-457**; discussion 451-457**
9 **Hoehn-Berlage M,** Norris DG**, Kohno K, Mies G, Leibfritz** D, **Hossmann KA. Evolution of regional changes in appar**ent diffusion coefficient during focal ischemia of rat brain: the relationship of quantitative diffusion NMR imaging to reduction in cerebral blood flow and metabolic disturbances. *J Cereb Blood Flow Metab* 1995**; 15:** 1002-**1011**
10 **Lo EH**, Pierce AR, Mandeville JB, Rosen BR. **Neuroprotection with NBQX in rat focal cerebral ischemia. Effects** on ADC probability distribution functions and diffusion-perfusion relationships. *Stroke* 1997; **28**: 439-446; discussion 446-447
11 **Schlaug G**, Benfield A, Baird AE, Siewert B, Lövblad KO, Parker RA, Edelman RR, Warach S. The ischemic penumbra: operationally defined by diffusion and perfusion MRI. *Neurology* 1999; **53**: 1528-1537
12 **Kidwell CS**, Alger JR, Saver JL. Beyond mismatch: evolving paradigms in imaging the ischemic penumbra with multimodal magnetic resonance imaging. *Stroke* 2003; **34**: 2729-2735
13 **Hussain MS**, Bhagat YA, Liu S, Scozzafava J, Khan KA, Dillon WP, Shuaib A. DWI lesion volume reduction following acute stroke treatment with transient partial aortic obstruction. *J Neuroimaging* 2010; **20**: 379-381
14 **Heiss WD**. The concept of the penumbra: can it be translated to stroke management? *Int J Stroke* 2010; **5**: 290-295
15 **Henninger N,** Bouley **J, Nelligan JM, Sicard KM, Fisher M.** Normobaric hyperoxia delays perfusion/diffusion mismatch evolution, reduces infarct volume, and differentially affects neuronal cell death pathways after suture middle cerebral artery occlusion in rats. *J Cereb Blood Flow Metab* 2007**; 27:** 1632-**1642**
16 **Provenzale JM**, Jahan R, Naidich TP, Fox AJ. Assessment of the patient with hyperacute stroke: imaging and therapy. *Radiology* 2003; **229**: 347-359
17 **Sunshine JL**, Tarr RW, Lanzieri CF, Landis DM, Selman WR, Lewin JS. Hyperacute stroke: ultrafast MR imaging to triage patients prior to therapy. *Radiology* 1999; **212**: 325-332
18 **Butcher KS,** Parsons **MW, Davis S, Donnan G. PWI/DWI** mismatch: better definition required. *Stroke* **2003; 34:** e215-**e216; author reply e215-e216**
19 **Butcher KS**, Parsons M, MacGregor L, Barber PA, Chalk J, Bladin C, Levi C, Kimber T, Schultz D, Fink J, Tress B, Donnan G, Davis S. Refining the perfusion-diffusion mismatch hypothesis. *Stroke* 2005; **36**: 1153-1159
20 **Sorensen AG**, Buonanno FS, Gonzalez RG, Schwamm LH, Lev MH, Huang-Hellinger FR, Reese TG, Weisskoff RM, Davis TL, Suwanwela N, Can U, Moreira JA, Copen WA, Look RB, Finklestein SP, Rosen BR, Koroshetz WJ. Hyperacute stroke: evaluation with combined multisection diffusion-weighted and hemodynamically weighted echo-planar MR imaging. *Radiology* 1996; **199**: 391-401
21 **Neumann-Haefelin T**, Wittsack HJ, Wenserski F, Siebler M, Seitz RJ, Mödder U, Freund HJ. **Diffusion- and perfusion-**weighted MRI. The DWI/PWI mismatch region in acute stroke. *Stroke* 1999; **30**: 1591-1597
22 **Grandin CB**, Duprez TP, Smith AM, Oppenheim C, Peeters A, Robert AR, Cosnard G. Which MR-derived perfusion parameters are the best predictors of infarct growth in hyperacute stroke? Comparative study between relative and quantitative measurements. *Radiology* 2002; **223**: 361-370
23 **Kane I**, Carpenter T, Chappell F, Rivers C, Armitage P, Sandercock P, Wardlaw J. Comparison of 10 different magnetic resonance perfusion imaging processing methods in acute ischemic stroke: effect on lesion size, proportion of patients with diffusion/perfusion mismatch, clinical scores, and radiologic outcomes. *Stroke* 2007; **38**: 3158-3164
24 **Schaefer PW**, Hunter GJ, He J, Hamberg LM, Sorensen AG, Schwamm LH, Koroshetz WJ, Gonzalez RG. Predicting cerebral ischemic infarct volume with diffusion and perfusion MR imaging. *AJNR Am J Neuroradiol* 2002; **23**: 1785-1794
25 **Lee S,** Kim **D, Jeong E, Yoon P, Cha S, Lee J. Temporal** changes in reversible cerebral ischemia on perfusion- and diffusion-weighted magnetic resonance imaging: the value of relative cerebral blood volume maps. *Neuroradiology* 2002**;** 44**; 103-108**
26 **Simonsen CZ**, Røhl L, Vestergaard-Poulsen P, Gyldensted C, Andersen G, Østergaard L. Final infarct size after acute stroke: prediction with flow heterogeneity. *Radiology* 2002; **225**: 269-275
27 **Bandera E**, Botteri M, Minelli C, Sutton A, Abrams KR, Latronico N. Cerebral blood flow threshold of ischemic penumbra and infarct core in acute ischemic stroke: a systematic review. *Stroke* 2006; **37**: 1334-1339
28 **Sobesky J**, Zaro Weber O, Lehnhardt FG, Hesselmann V, Thiel A, Dohmen C, Jacobs A, Neveling M, Heiss WD. Which time-to-peak threshold best identifies penumbral flow? A comparison of perfusion-weighted magnetic resonance imaging and positron emission tomography in acute ischemic stroke. *Stroke* 2004; **35**: 2843-2847
29 **Koga M**, Reutens DC, Wright P, Phan T, Markus R, Pedreira

B, Fitt G, Lim I, Donnan GA. The existence and evolution of diffusion-perfusion mismatched tissue in white and gray matter after acute stroke. *Stroke* 2005; **36**: 2132-2137
30 **Parsons MW**, Barber PA, Chalk J, Darby DG, Rose S, Desmond PM, Gerraty RP, Tress BM, Wright PM, Donnan GA, Davis SM. Diffusion- and perfusion-weighted MRI response to thrombolysis in stroke. *Ann Neurol* 2002; **51**: 28-37
31 **Kane I**, Hand PJ, Rivers C, Armitage P, Bastin ME, Lindley R, Dennis M, Wardlaw JM. A practical assessment of magnetic resonance diffusion-perfusion mismatch in acute stroke: observer variation and outcome. *J Neurol* 2009; **256**: 1832-1838
32 **Hamberg LM**, Hunter GJ, Maynard KI, Owen C, Morris PP, Putman CM, Ogilvy C, González RG. Functional CT perfusion imaging in predicting the extent of cerebral infarction from a 3-hour middle cerebral arterial occlusion in a primate stroke model. *AJNR Am J Neuroradiol* 2002; **23**: 1013-1021
33 **Fiehler J**, von Bezold M, Kucinski T, Knab R, Eckert B, Wittkugel O, Zeumer H, Röther J. Cerebral blood flow predicts lesion growth in acute stroke patients. *Stroke* 2002; **33**: 2421-2425
34 **Luby M**, Ku KD, Latour LL, Merino JG, Hsia AW, Lynch JK, Warach S. Visual perfusion-diffusion mismatch is equivalent to quantitative mismatch. *Stroke* 2011; **42**: 1010-1014
35 **Nagakane Y**, Christensen S, Brekenfeld C, Ma H, Churilov L, Parsons MW, Levi CR, Butcher KS, Peeters A, Barber PA, Bladin CF, De Silva DA, Fink J, Kimber TE, Schultz DW, Muir KW, Tress BM, Desmond PM, Davis SM, Donnan GA. EPITHET: Positive Result After Reanalysis Using Baseline Diffusion-Weighted Imaging/Perfusion-Weighted Imaging Co-Registration. *Stroke* 2011; **42**: 59-64
36 **Campbell BC**, Christensen S, Foster SJ, Desmond PM, Parsons MW, Butcher KS, Barber PA, Levi CR, Bladin CF, Donnan GA, Davis SM. Visual assessment of perfusion-diffusion mismatch is inadequate to select patients for thrombolysis. *Cerebrovasc Dis* 2010; **29**: 592-596
37 **Butcher K**, Parsons M, Allport L, Lee SB, Barber PA, Tress B, Donnan GA, Davis SM. Rapid assessment of perfusion-diffusion mismatch. *Stroke* 2008; **39**: 75-81
38 **Ay H**, Arsava EM, Vangel M, Oner B, Zhu M, Wu O, Singhal A, Koroshetz WJ, Sorensen AG. Interexaminer difference in infarct volume measurements on MRI: a source of variance in stroke research. *Stroke* 2008; **39**: 1171-1176
39 **Canal N**, Frattola L, Smirne S. The metabolism of cyclic-3′-5′-adenosine monophosphate (cAMP) in diseased muscle. *J Neurol* 1975; **208**: 259-265
40 **James JR**, Yoder KK, Osuntokun O, Kalnin A, Bruno A, Morris ED. A supervised method for calculating perfusion/diffusion mismatch volume in acute ischemic stroke. *Comput Biol Med* 2006; **36**: 1268-1287
41 **Lansberg MG,** Lee J, Christensen S, Straka M, De Silva DA, Mlynash M, Campbell BC, Bammer R, Olivot JM, Desmond P, Davis SM, Donnan GA, Albers GW. RAPID automated patient selection for reperfusion therapy: a pooled analysis of the Echoplanar Imaging Thrombolytic Evaluation Trial (EPITHET) and the Diffusion and Perfusion Imaging Evaluation for Understanding Stroke Evolution (DEFUSE) Study. *Stroke* 2011; **42:** 1608-1614
42 **Straka M**, Albers GW, Bammer R. Real-time diffusion-perfusion mismatch analysis in acute stroke. *J Magn Reson Imaging* 2010; **32**: 1024-1037
43 **Hotter B**, Pittl S, Ebinger M, Oepen G, Jegzentis K, Kudo K, Rozanski M, Schmidt WU, Brunecker P, Xu C, Martus P, Endres M, Jungehülsing GJ, Villringer A, Fiebach JB. Prospective study on the mismatch concept in acute stroke patients within the first 24 h after symptom onset - 1000Plus study. *BMC Neurol* 2009; **9**: 60
44 **Luby M**, Warach S. Reliability of MR perfusion-weighted and diffusion-weighted imaging mismatch measurement methods. *AJNR Am J Neuroradiol* 2007; **28**: 1674-1678
45 **Touzani O**, Roussel S, MacKenzie ET. The ischaemic penumbra. *Curr Opin Neurol* 2001; **14**: 83-88
46 **Davis SM**, Donnan GA. Advances in penumbra imaging with MR. *Cerebrovasc Dis* 2004; **17** Suppl 3: 23-27
47 **Darby DG**, Barber PA, Gerraty RP, Desmond PM, Yang Q, Parsons M, Li T, Tress BM, Davis SM. Pathophysiological topography of acute ischemia by combined diffusion-weighted and perfusion MRI. *Stroke* 1999; **30**: 2043-2052
48 **Copen WA**, Rezai Gharai L, Barak ER, Schwamm LH, Wu O, Kamalian S, Gonzalez RG, Schaefer PW. Existence of the diffusion-perfusion mismatch within 24 hours after onset of acute stroke: dependence on proximal arterial occlusion. *Radiology* 2009; **250**: 878-886
49 **Baron JC**, Moseley ME. For how long is brain tissue salvageable? Imaging-based evidence. *J Stroke Cerebrovasc Dis* 2000; **9**: 15-20
50 **Perez A**, Restrepo L, Kleinman JT, Barker P, Beauchamp N, Wityk RJ. Patients with diffusion-perfusion mismatch on magnetic resonance imaging 48 hours or more after stroke symptom onset: clinical and imaging features. *J Neuroimaging* 2006; **16**: 329-333
51 **Chen F**, Liu Q, Wang H, Suzuki Y, Nagai N, Yu J, Marchal G, Ni Y. Comparing two methods for assessment of perfusion-diffusion mismatch in a rodent model of ischaemic stroke: a pilot study. *Br J Radiol* 2008; **81**: 192-198
52 **Restrepo L**, Jacobs MA, Barker PB, Beauchamp NJ, Skolasky RL, Keswani SC, Wityk RJ. Etiology of perfusion-diffusion magnetic resonance imaging mismatch patterns. *J Neuroimaging* 2005; **15**: 254-260
53 **Paciaroni M**, Medeiros E, Bogousslavsky J. Desmoteplase. *Expert Opin Biol Ther* 2009; **9**: 773-778
54 **Marks MP**, Olivot JM, Kemp S, Lansberg MG, Bammer R, Wechsler LR, Albers GW, Thijs V. Patients with acute stroke treated with intravenous tPA 3-6 hours after stroke onset: correlations between MR angiography findings and perfusion- and diffusion-weighted imaging in the DEFUSE study. *Radiology* 2008; **249**: 614-623
55 **Kakuda W**, Hamilton S, Thijs VN, Lansberg MG, Kemp S, Skalabrin E, Albers GW. Optimal outcome measures for detecting clinical benefits of early reperfusion: insights from the DEFUSE Study. *J Stroke Cerebrovasc Dis* 2008; **17**: 235-240
56 **Bang OY,** Saver JL, Buck BH, Alger JR, Starkman S, Ovbiagele B, Kim D, Jahan R, Duckwiler GR, Yoon SR, Viñuela F, Liebeskind DS. Impact of collateral flow on tissue fate in acute ischaemic stroke. *J Neurol Neurosurg Psychiatry* 2008; **79:** 625-629
57 **González RG,** Hakimelahi R, Schaefer PW, Roccatagliata L, Sorensen AG, Singhal AB. Stability of large diffusion/perfusion mismatch in anterior circulation strokes for 4 or more hours. *BMC Neurol* 2010; **10:** 13
58 **Harris AD**, Kosior RK, Chen HS, Andersen LB, Frayne R. Evolution of hyperacute stroke over 6 hours using serial MR perfusion and diffusion maps. *J Magn Reson Imaging* 2009; **29**: 1262-1270
59 **Olivot JM**, Albers GW. Using advanced MRI techniques for patient selection before acute stroke therapy. *Curr Treat Options Cardiovasc Med* 2010; **12**: 230-239
60 **Heiss WD**, Sobesky J, Hesselmann V. Identifying thresholds for penumbra and irreversible tissue damage. *Stroke* 2004; **35**: 2671-2674
61 **Carrera E,** Jones PS, Iglesias S, Guadagno JV, Warburton EA, Fryer TD, Aigbirhio FI, Baron JC. The vascular mean transit time: a surrogate for the penumbra flow threshold? *J Cereb Blood Flow Metab* 2010; **31:** 1027-1035
62 **Røhl L**, Ostergaard L, Simonsen CZ, Vestergaard-Poulsen P, Andersen G, Sakoh M, Le Bihan D, Gyldensted C. Viability thresholds of ischemic penumbra of hyperacute stroke defined by perfusion-weighted MRI and apparent diffusion coefficient. *Stroke* 2001; **32**: 1140-1146
63 **Oppenheim C**, Grandin C, Samson Y, Smith A, Duprez T, Marsault C, Cosnard G. Is there an apparent diffusion coef-

ficient threshold in predicting tissue viability in hyperacute stroke? *Stroke* 2001; **32**: 2486-2491
64 **Chen J**, Licht DJ, Smith SE, Agner SC, Mason S, Wang S, Silvestre DW, Detre JA, Zimmerman RA, Ichord RN, Wang J. Arterial spin labeling perfusion MRI in pediatric arterial ischemic stroke: initial experiences. *J Magn Reson Imaging* 2009; **29**: 282-290
65 **Tsang A**, Stobbe RW, Asdaghi N, Hussain MS, Bhagat YA, Beaulieu C, Emery D, Butcher KS. Relationship between sodium intensity and perfusion deficits in acute ischemic stroke. *J Magn Reson Imaging* 2011; **33**: 41-47
66 **Suzuki K**, Igarashi H, Watanabe M, Nakamura Y, Nakada T. Separation of perfusion signals from diffusion-weighted image series enabled by independent component analysis. *J Neuroimaging* 2011; **21:** 384-394
67 **Sun PZ**, Benner T, Copen WA, Sorensen AG. Early experience of translating pH-weighted MRI to image human subjects at 3 Tesla. *Stroke* 2010; **41**: S147-S151
68 **Sun PZ,** Zhou JY**, Sun WY, Huang J, van Zijl PCM. Detection** of the ischemic penumbra using pH-weighted MRI. *J Cereb Blood Flow Metab* 2007**; 27:** 1129-**1136**
69 **Schwab S**, Spranger M, Aschoff A, Steiner T, Hacke W. Brain temperature monitoring and modulation in patients with severe MCA infarction. *Neurology* 1997; **48**: 762-767
70 **Corbett R,** Laptook A**, Weatherall P. Noninvasive measure**ments of human brain temperature using volume-localized proton magnetic resonance spectroscopy. *J Cereb Blood Flow Metab* 1997**; 17:** 363-**369**
71 **Karaszewski B**, Wardlaw JM, Marshall I, Cvoro V, Wartolowska K, Haga K, Armitage PA, Bastin ME, Dennis MS. Measurement of brain temperature with magnetic resonance spectroscopy in acute ischemic stroke. *Ann Neurol* 2006; **60**: 438-446
72 **Heiss WD.** Ischemic penumbra: evidence from functional imaging in man. *J Cereb Blood Flow Metab* 2000**; 20:** 1276-**1293**
73 **Geisler BS**, Brandhoff F, Fiehler J, Saager C, Speck O, Röther J, Zeumer H, Kucinski T. Blood-oxygen-level-dependent MRI allows metabolic description of tissue at risk in acute stroke patients. *Stroke* 2006; **37**: 1778-1784
74 **Siemonsen S**, Fitting T, Thomalla G, Horn P, Finsterbusch J, Summers P, Saager C, Kucinski T, Fiehler J. T2′ imaging predicts infarct growth beyond the acute diffusion-weighted imaging lesion in acute stroke. *Radiology* 2008; **248**: 979-986
75 **Santosh C,** Brennan D, McCabe C, Macrae IM, Holmes WM, Graham DI, Gallagher L, Condon B, Hadley DM, Muir KW, Gsell W. Potential use of oxygen as a metabolic biosensor in combination with T2*-weighted MRI to define the ischemic penumbra. *J Cereb Blood Flow Metab* 2008; **28:** 1742-1753
76 **Heiss WD**, Sobesky J. Comparison of PET and DW/PW-MRI in acute ischemic stroke. *Keio J Med* 2008; **57**: 125-131
77 **Guadagno JV,** Warburton EA**, Aigbirhio FI, Smielewski** P, Fryer **TD, Harding S, Price CJ, GillardJH, Carpenter TA,** Baron **JC. Does the acute diffusion-weighted imaging lesion** represent penumbra as well as core? A combined quantitative PET/MRI voxel-based study. *J Cereb Blood Flow Metab* 2004; **24:** 1249-**1254**
78 **Guadagno JV**, Warburton EA, Jones PS, Fryer TD, Day DJ, Gillard JH, Carpenter TA, Aigbirhio FI, Price CJ, Baron JC. The diffusion-weighted lesion in acute stroke: heterogeneous patterns of flow/metabolism uncoupling as assessed by quantitative positron emission tomography. *Cerebrovasc Dis* 2005; **19**: 239-246
79 **Heiss WD**, Graf R, Wienhard K. Relevance of experimental ischemia in cats for stroke management: a comparative re-evaluation. *Cerebrovasc Dis* 2001; **11**: 73-81
80 **Kim SJ,** Seok JM**, Bang OY, Kim GM, Kim KH, Jeon P,** Chung **CS, Lee KJ, Alger JR, Liebeskind DS. MR mismatch** profiles in patients with intracranial atherosclerotic stroke: a comprehensive approach comparing stroke subtypes. *J Cereb Blood Flow Metab* 2009**; 29:** 1138-**1145**
81 **Ma L**, Gao PY, Lin Y, Xue J, Wang XC, Wang YJ, Wang YL, Liao XL, Liu ML, Cui SM, Yu L, Tong SJ, Huang YL, Zhou YM. Can baseline magnetic resonance angiography (MRA) status become a foremost factor in selecting optimal acute stroke patients for recombinant tissue plasminogen activator (rt-PA) thrombolysis beyond 3 hours? *Neurol Res* 2009; **31**: 355-361
82 **Wechsler LR**. Imaging evaluation of acute ischemic stroke. *Stroke* 2011; **42**: S12-S15
83 **Bai Q**, Zhao Z, Li Y, Sui H, Xie X, Gong Y, Zhao X, Wang L, Xia W, Shen J, Lu L. The application of fast multiparametric protocol MRI-based thrombolysis with rt-PA hyperacute cerebral infarction. *Neurol Res* 2008; **30**: 344-347
84 **Zhao Z**, Bai Q, Sui H, Xie X, Wen F. Fast multimode MRI based emergency assessment of hyperacute stroke thrombolysis. *Neurol Res* 2009; **31**: 346-350
85 **Harrer JU**. Clinical applicability and the perfusion-diffusion mismatch theory: not yet a perfect match. *Neurology* 2010; **75**: 1034-1035
86 **Chemmanam T**, Campbell BC, Christensen S, Nagakane Y, Desmond PM, Bladin CF, Parsons MW, Levi CR, Barber PA, Donnan GA, Davis SM. Ischemic diffusion lesion reversal is uncommon and rarely alters perfusion-diffusion mismatch. *Neurology* 2010; **75**: 1040-1047
87 **Engelter ST**, Wetzel SG, Bonati LH, Fluri F, Lyrer PA. **The** clinical significance of diffusion-weighted MR imaging in stroke and TIA patients. *Swiss Med Wkly* 2008; **138**: 729-740
88 **Montiel NH**, Rosso C, Chupin N, Deltour S, Bardinet E, Dormont D, Samson Y, Baillet S. Automatic prediction of infarct growth in acute ischemic stroke from MR apparent diffusion coefficient maps. *Acad Radiol* 2008; **15**: 77-83
89 **Rivers CS**, Wardlaw JM, Armitage PA, Bastin ME, Carpenter TK, Cvoro V, Hand PJ, Dennis MS. Do acute diffusion- and perfusion-weighted MRI lesions identify final infarct volume in ischemic stroke? *Stroke* 2006; **37**: 98-104
90 **Bates S,** Read SJ, Harrison DC, Topp S, Morrow R, Gale D, Murdock P, Barone FC, Parsons AA, Gloger IS. **Characterisation** of gene expression changes following permanent MCAO in the rat using subtractive hybridisation. *Brain Res Mol Brain Res* 2001**; 93:** 70-80
91 **Lansberg MG**, Thijs VN, Hamilton S, Schlaug G, Bammer R, Kemp S, Albers GW. Evaluation of the clinical-diffusion and perfusion-diffusion mismatch models in DEFUSE. *Stroke* 2007; **38**: 1826-1830
92 **Barber PA**, Hill MD, Eliasziw M, Demchuk AM, Pexman JH, Hudon ME, Tomanek A, Frayne R, Buchan AM. Imaging of the brain in acute ischaemic stroke: comparison of computed tomography and magnetic resonance diffusion-weighted imaging. *J Neurol Neurosurg Psychiatry* 2005; **76**: 1528-1533
93 **Tei H**, Uchiyama S, Usui T. Clinical-diffusion mismatch defined by NIHSS and ASPECTS in non-lacunar anterior circulation infarction. *J Neurol* 2007; **254**: 340-346
94 **Deguchi I**, Takeda H, Furuya D, Hattori K, Dembo T, Nagoya H, Kato Y, Fukuoka T, Maruyama H, Tanahashi N. Significance of clinical-diffusion mismatch in hyperacute cerebral infarction. *J Stroke Cerebrovasc Dis* 2010; **20**: 62-67
95 **Ebinger M**, Iwanaga T, Prosser JF, De Silva DA, Christensen S, Collins M, Parsons MW, Levi CR, Bladin CF, Barber PA, Donnan GA, Davis SM. Clinical-diffusion mismatch and benefit from thrombolysis 3 to 6 hours after acute stroke. *Stroke* 2009; **40**: 2572-2574
96 **Schaefer PW**, Barak ER, Kamalian S, Gharai LR, Schwamm L, Gonzalez RG, Lev MH. Quantitative assessment of core/penumbra mismatch in acute stroke: CT and MR perfusion imaging are strongly correlated when sufficient brain volume is imaged. *Stroke* 2008; **39**: 2986-2992
97 **Wintermark M**, Flanders AE, Velthuis B, Meuli R, van Leeuwen M, Goldsher D, Pineda C, Serena J, van der Schaaf I, Waaijer A, Anderson J, Nesbit G, Gabriely I, Medina V, Quiles A, Pohlman S, Quist M, Schnyder P, Bogousslavsky

J, Dillon WP, Pedraza S. Perfusion-CT assessment of infarct core and penumbra: receiver operating characteristic curve analysis in 130 patients suspected of acute hemispheric stroke. *Stroke* 2006; **37**: 979-985

98 **Sun Z**, Zhang X, Zhang Y, Guo H, Zhang J, Yu C. Estimation of the ischemic penumbra based on CT perfusion a pilot study. *Acad Radiol* 2010; **17**: 1535-1542

99 **Wang XC,** Gao PL, Lin Y, Xue J, Ma L, Wang CJ, Liao XL, Liu GR, Sui BB, Wang C. Diagnostic valne of CT perfusion source hnages in snperacute stroke. *Zhongguo Fangshexue Zazhi* 2009; **43:** 235-238

100 **Messé SR**, Kasner SE, Chalela JA, Cucchiara B, Demchuk AM, Hill MD, Warach S. CT-NIHSS mismatch does not correlate with MRI diffusion-perfusion mismatch. *Stroke* 2007; **38**: 2079-2084

101 **Furlan AJ**, Eyding D, Albers GW, Al-Rawi Y, Lees KR, Rowley HA, Sachara C, Soehngen M, Warach S, Hacke W. Dose Escalation of Desmoteplase for Acute Ischemic Stroke (DEDAS): evidence of safety and efficacy 3 to 9 hours after stroke onset. *Stroke* 2006; **37**: 1227-1231

102 **Chen F**, Suzuki Y, Nagai N, Sun X, Wang H, Yu J, Marchal G, Ni Y. Microplasmin and tissue plasminogen activator: comparison of therapeutic effects in rat stroke model at multiparametric MR imaging. *Radiology* 2007; **244**: 429-438

103 **Köhrmann M**, Sauer R, Huttner HB, Engelhorn T, Doerfler A, Schellinger PD. **MRI mismatch-based intravenous thrombolysis for isolated cerebellar infarction.** *Stroke* 2009; **40**: 1897-1899

104 **Hacke W,** Furlan AJ, **Al-Rawi Y, Davalos A, Fiebach JB, Gruber F, Kaste M, Lipka LJ Pedraza S, Ringleb PA, Rowley HA,** Schneider D, **Leal JS, Söhngen M, Teal PA, Wilhelm-Ogunbiyi K, Wintermark M, Warach S. Intravenous desmoteplase** in patients with acute ischaemic stroke selected by MRI perfusion-diffusion weighted imaging or perfusion CT (DIAS-2): a prospective, randomised, double-blind, placebo-controlled study. *Lancet Neurol* 2009**; 8:** 141-**150**

105 **Cho AH**, Sohn SI, Han MK, Lee DH, Kim JS, Choi CG, Sohn CH, Kwon SU, Suh DC, Kim SJ, Bae HJ, Kang DW. Safety and efficacy of MRI-based thrombolysis in unclear-onset stroke. A preliminary report. *Cerebrovasc Dis* 2008; **25**: 572-579

106 **Davis SM,** Donnan GA, **Parsons MW, Fracp CL, Butcher KS,** Peeters A**, Barber PA, Bladin C, Silva DAD, Byrnes G, Chalk** JB. **Effects of alteplase beyond 3 h after stroke in the Echo**planar Imaging Thrombolytic Evaluation Trial (EPITHET): a placebo-controlled randomised trial. *Lancet Neurol* 2008**; 7:** 299-309

107 **Hacke W**, Albers G, Al-Rawi Y, Bogousslavsky J, Davalos A, Eliasziw M, Fischer M, Furlan A, Kaste M, Lees KR, Soehngen M, Warach S. The Desmoteplase in Acute Ischemic Stroke Trial (DIAS): a phase II MRI-based 9-hour window acute stroke thrombolysis trial with intravenous desmoteplase. *Stroke* 2005; **36**: 66-73

108 **Miyamoto N**, Naito I, Takatama S, Shimizu T, Iwai T, Shimaguchi H. Urgent stenting for patients with acute stroke due to atherosclerotic occlusive lesions of the cervical internal carotid artery. *Neurol Med Chir (Tokyo)* 2008; **48**: 49-55; discussion 55-56

109 **Beck J**, Raabe A, Lanfermann H, Berkefeld J, De Rochemont Rdu M, Zanella F, Seifert V, Weidauer S. Effects of balloon angioplasty on perfusion- and diffusion-weighted magnetic resonance imaging results and outcome in patients with cerebral vasospasm. *J Neurosurg* 2006; **105**: 220-227

110 **Imai K**, Mori T, Izumoto H, Takabatake N, Kunieda T, Shimizu H, Watanabe M. Clot removal therapy by aspiration and extraction for acute embolic carotid occlusion. *AJNR Am J Neuroradiol* 2006; **27**: 1521-1527

111 **Davis SM**, Donnan GA, Butcher KS, Parsons M. Selection of thrombolytic therapy beyond 3 h using magnetic resonance imaging. *Curr Opin Neurol* 2005; **18**: 47-52

112 **Albers GW**, Thijs VN, Wechsler L, Kemp S, Schlaug G, Skalabrin E, Bammer R, Kakuda W, Lansberg MG, Shuaib A, Coplin W, Hamilton S, Moseley M, Marks MP. Magnetic resonance imaging profiles predict clinical response to early reperfusion: the diffusion and perfusion imaging evaluation for understanding stroke evolution (DEFUSE) study. *Ann Neurol* 2006; **60**: 508-517

113 **Chen F**, Suzuki Y, Nagai N, Peeters R, Marchal G, Ni Y. Dynamic susceptibility contrast-enhanced perfusion MR imaging at 1.5 T predicts final infarct size in a rat stroke model. *J Neurosci Methods* 2005; **141**: 55-60

114 **Barber PA**, Darby DG, Desmond PM, Yang Q, Gerraty RP, Jolley D, Donnan GA, Tress BM, Davis SM. Prediction of stroke outcome with echoplanar perfusion- and diffusion-weighted MRI. *Neurology* 1998; **51**: 418-426

115 **Surikova I**, Meisel S, Siebler M, Wittsack HJ, Seitz RJ. Significance of the perfusion-diffusion mismatch in chronic cerebral ischemia. *J Magn Reson Imaging* 2006; **24**: 771-778

116 **Mezzapesa DM**, Petruzzellis M, Lucivero V, Prontera M, Tinelli A, Sancilio M, Carella A, Federico F. Multimodal MR examination in acute ischemic stroke. *Neuroradiology* 2006; **48**: 238-246

117 **Kane I**, Sandercock P, Wardlaw J. Magnetic resonance perfusion diffusion mismatch and thrombolysis in acute ischaemic stroke: a systematic review of the evidence to date. *J Neurol Neurosurg Psychiatry* 2007; **78**: 485-491

118 **Hillis AE**, Wityk RJ, Barker PB, Ulatowski JA, Jacobs MA. Change in perfusion in acute nondominant hemisphere stroke may be better estimated by tests of hemispatial neglect than by the National Institutes of Health Stroke Scale. *Stroke* 2003; **34**: 2392-2396

119 **Heidenreich JO**, Hsu D, Wang G, Jesberger JA, Tarr RW, Zaidat OO, Sunshine JL. Magnetic resonance imaging results can affect therapy decisions in hyperacute stroke care. *Acta Radiol* 2008; **49**: 550-557

120 **Stoeckel MC**, Wittsack HJ, Meisel S, Seitz RJ. **Pattern of cortex and white matter involvement in severe middle cerebral artery ischemia.** *J Neuroimaging* 2007; **17**: 131-140

121 **Ogata T**, Nagakane Y, Christensen S, Ma H, Campbell BC, Churilov L, Olivot JM, Desmond PM, Albers GW, Davis SM, Donnan GA. A topographic study of the evolution of the MR DWI/PWI mismatch pattern and its clinical impact: a study by the EPITHET and DEFUSE Investigators. *Stroke* 2011; **42**: 1596-1601

122 **Ay H**, Arsava EM, Rosand J, Furie KL, Singhal AB, Schaefer PW, Wu O, Gonzalez RG, Koroshetz WJ, Sorensen AG. Severity of leukoaraiosis and susceptibility to infarct growth in acute stroke. *Stroke* 2008; **39**: 1409-1413

123 **Fiebach JB**, Hopt A, Vucic T, Brunecker P, Nolte CH, Doege C, Villringer K, Jungehulsing GJ, Kunze C, Wegener S, Villringer A. Inverse mismatch and lesion growth in small subcortical ischaemic stroke. *Eur Radiol* 2010; **20**: 2983-2989

124 **Sims JR**, Gharai LR, Schaefer PW, Vangel M, Rosenthal ES, Lev MH, Schwamm LH. **ABC/2 for rapid clinical estimate** of infarct, perfusion, and mismatch volumes. *Neurology* 2009; **72**: 2104-2110

125 **Bang OY**, Saver JL, Lee KH, Kim GM, Chung CS, Kim SJ, Ovbiagele B, Alger JR, Liebeskind DS. Characteristics of patients with target magnetic resonance mismatch profile: data from two geographically and racially distinct populations. *Cerebrovasc Dis* 2010; **29**: 87-94

126 **Kakuda W**, Lansberg MG, Thijs VN, Kemp SM, Bammer R, Wechsler LR, Moseley ME, Marks MP, Albers GW. Optimal definition for PWI/DWI mismatch in acute ischemic stroke patients. *J Cereb Blood Flow Metab* 2008; **28**: 887-891

127 **Baird AE**, Benfield A, Schlaug G, Siewert B, Lövblad KO, Edelman RR, Warach S. Enlargement of human cerebral ischemic lesion volumes measured by diffusion-weighted magnetic resonance imaging. *Ann Neurol* 1997; **41**: 581-589

128 **Restrepo L**, Jacobs MA, Barker PB, Wityk RJ. Assessment

of transient ischemic attack with diffusion- and perfusion-weighted imaging. *AJNR Am J Neuroradiol* **2004; 25**: 1645-1652
129 **Ma H**, Zavala JA, Teoh H, Churilov L, Gunawan M, Ly J, Wright P, Phan T, Arakawa S, Davis SM, Donnan GA. Fragmentation of the classical magnetic resonance mismatch "penumbral" pattern with time. *Stroke* 2009; **40**: 3752-3757
130 **Lee KY**, Latour LL, Luby M, Hsia AW, Merino JG, Warach S. Distal hyperintense vessels on FLAIR: an MRI marker for collateral circulation in acute stroke? *Neurology* 2009; **72**: 1134-1139
131 **Chen F**, Suzuki Y, Nagai N, Sun X, Coudyzer W, Yu J, Marchal G, Ni Y. Delayed perfusion phenomenon in a rat stroke model at 1.5 T MR: an imaging sign parallel to spontaneous reperfusion and ischemic penumbra? *Eur J Radiol* 2007; **61**: 70-78
132 **Ma HK**, Zavala JA, Churilov L, Ly J, Wright PM, Phan TG, Arakawa S, Davis SM, Donnan GA. The hidden mismatch: an explanation for infarct growth without perfusion-weighted imaging/diffusion-weighted imaging mismatch in patients with acute ischemic stroke. *Stroke* 2011; **42**: 662-668
133 **Cho TH**, Hermier M, Alawneh JA, Ritzenthaler T, Desestret V, Østergaard L, Derex L, Baron JC, Nighoghossian N. Total mismatch: negative diffusion-weighted imaging but extensive perfusion defect in acute stroke. *Stroke* 2009; **40**: 3400-3402
134 **Blondin D**, Seitz RJ, Rusch O, Janssen H, Andersen K, Wittsack HJ, Turowski B. Clinical impact of MRI perfusion disturbances and normal diffusion in acute stroke patients. *Eur J Radiol* 2009; **71**: 1-10
135 **Woods RP**, Iacoboni M, Mazziotta JC. **Brief report: bilateral** spreading cerebral hypoperfusion during spontaneous migraine headache. *N Engl J Med* 1994; **331**: 1689-1692
136 **Wohlgemuth WA**, Schulte-Altedorneburg G, Becker T, Zha L, Kramer D, Kirchhof K. Evaluation of a new Spin-echo diffusion-weighted sequence on a 0.35 T open magnetic resonance imaging (MRI)-system: first experiences within 3 h after acute stroke. *Neuroradiology* 2005; **47**: 532-538
137 **Olivot JM**, Mlynash M, Thijs VN, Kemp S, Lansberg MG, Wechsler L, Schlaug G, Bammer R, Marks MP, Albers GW. Relationships between infarct growth, clinical outcome, and early recanalization in diffusion and perfusion imaging for understanding stroke evolution (DEFUSE). *Stroke* 2008; **39**: 2257-2263
138 **Pedraza S**, Puig J, Blasco G, Daunis-i-Estadella J, Boada I, Bardera A, Prats A, Castellanos M, Serena J. Magnetic resonance imaging biomarkers of ischemic stroke: criteria for the validation of primary imaging biomarkers. *Drug News Perspect* 2009; **22**: 481-486

S- Editor Cheng JX **L- Editor** Webster JR **E- Editor** Xiong L

World Journal of Radiology

Online Submissions: http://www.wjgnet.com/1949-8470office
wjr@wjgnet.com
doi:10.4329/wjr.v4.i3.75

World J Radiol 2012 March 28; 4(3): 75-82
ISSN 1949-8470 (online)

REVIEW

Dural lesions mimicking meningiomas: A pictorial essay

Danai Chourmouzi, Stamatia Potsi, Anestis Moumtzouoglou, Elisavet Papadopoulou, Kostas Drevelegas, Thomas Zaraboukas, Antonios Drevelegas

Danai Chourmouzi, Stamatia Potsi, Anestis Moumtzouoglou, Elisavet Papadopoulou, Kostas Drevelegas, Department of Radiology, Interbalkan Medical Center, GR 57001 Thessaloniki, Greece
Thomas Zaraboukas, Department of Pathology, Aristotle University Medical School of Thessaloniki, GR 57001 Thessaloniki, Greece
Antonios Drevelegas, Department of Radiology, AHEPA University Hospital, Aristotle University Medical School of Thessaloniki, GR 57001 Thessaloniki, Greece
Author contributions: Chourmouzi D was the major contributor in writing the manuscript; Chourmouzi D, Potsi S, Moumtzouoglou A, Papadopoulou E and Drevelegas K analyzed and interpreted the patient data regarding the clinical and radiological findings; Zaraboukas T interpreted the patient data regarding gross specimens and histopathology; Drevelegas A was involved in patient care during hospitalization, interpreted the radiological findings and contributed in writing the manuscript; all authors read and approved the final manuscript.
Correspondence to: Dr. Stamatia Potsi, Department of Radiology, Interbalkan Medical Center, Asklipiou 10, Pilaia, GR 57001 Thessaloniki, Greece. matinapotsi@hotmail.com
Telephone: +30-231-0400000 Fax: +30-231-0471056
Received: July 8, 2011 Revised: February 28, 2012
Accepted: March 7, 2012
Published online: March 28, 2012

Abstract

The purpose of this essay was to illustrate the radiological and pathological findings in a wide spectrum of dural lesions mimicking meningiomas. Familiarity with and knowledge of these findings will narrow the differential diagnosis and provide guidance for patient management. In this pictorial review, we describe the following entities: Solitary fibrous tumors, hemangiopericytoma, gliosarcoma, leiomyosarcoma, dural metastases, Hodgkin's disease, plasmocytoma, Rosai-Dorfman disease, neurosarcoidosis, melanocytic neoplasms and plasma cell granuloma.

Key words: Differential diagnosis; Dural lesions; Imaging; Meningiomas

Peer reviewers: Tetsu Niwa, MD, PhD, Department of Radiology, Kanagawa Children's Medical Center, 2-138-4 Mutsukawa, Minamiku, Yokohama 252-8555, Japan; Farideh Nejat, MD, MPH, Department of Neurosurgery, Children's Hospital Medical Center, Tehran University of Medical Sciences, Gharib Street, Mail Box 14155-7854, Tehran, Iran; Aaron Cohen-Gadol, MD, MSc, Clinical Assistant Professor, Indiana University Department of Neurosurgery, Clarian Neuroscience Center, 1801 North Senate Blvd, Suite 610, Indianapolis, IN 46202, United States; Tayfun Hakan, MD, Neurosurgery Clinic, Haydarpasa Numune Teaching and Research Hospital, Tibbiye Caddesi, Uskudar 34668, Istanbul, Turkey

Chourmouzi D, Potsi S, Moumtzouoglou A, Papadopoulou E, Drevelegas K, Zaraboukas T, Drevelegas A. Dural lesions mimicking meningiomas: A pictorial essay. *World J Radiol* 2012; 4(3): 75-82 Available from: URL: http://www.wjgnet.com/1949-8470/full/v4/i3/75.htm DOI: http://dx.doi.org/10.4329/wjr.v4.i3.75

INTRODUCTION

There are multiple neoplastic and non-neoplastic entities that clinically and radiographically mimic meningiomas. This pictorial review considers some of the lesions that can mimic meningiomas, including solitary fibrous tumors, hemangiopericytoma, gliosarcoma, leiomyosarcoma, dural metastases, Hodgkin's disease, plasmocytoma, Rosai-Dorfman disease, neurosarcoidosis, melanocytic neoplasms and plasma cell granuloma.

SOLITARY FIBROUS TUMORS

Central nervous system (CNS) solitary fibrous tumors are rare, dural-based mesenchymal neoplasms. Although initially described as primary neoplasms of the pleura, solitary fibrous tumors have subsequently been reported in virtually every body site[1]. The typical histological features

of solitary fibrous tumors are spindle cells arranged in a patternless architecture or interlacing fascicles, prominent collagenous bands, and branching vascular channels with thin walls; these tumors exhibit diffuse CD34 reactivity[2]. The tumors present at any age and have been reported to occur in both supra and infratentorial locations.

On computed tomography (CT), the mass is most often hyperdense and contains some calcifications. The appearance on magnetic resonance imaging (MRI) is that of an extra-axial, dural-based mass predominantly isointense on T1- and T2-weighted images. Intra-lesional inhomogeneity with areas of hypointensity and hyperintensity, best described as having a patchy appearance, has been reported. In most cases, homogenous enhancement on post-contrast T1-weighted images is seen (Figure 1). Surgery is the treatment of choice. Stereotactic and external beam radiation therapy may be indicated for postsurgical tumor remnants and for unresectable recurrences[3].

HEMANGIOPERICYTOMA

Intracranial hemangiopericytomas are neoplasms of the pericytes that originate in the meninges, represent less than 1% of all CNS tumors, are aggressive and tend to occur at an earlier age than other meningeal tumors, recur with high frequency, and metastasize extra-cranially. The location of intracranial hemangiopericytomas is similar to that of meningiomas. Histologically, hemangiopericytomas are highly cellular, vascular tumors composed of angular pericytes surrounding often ill-defined capillaries in a branching pattern (staghorn vascularity).

On CT, hemangiopericytomas are heterogeneous, hyperdense, dural-based lesions that, unlike meningiomas, are not associated with calcifications or hyperostosis, and they typically show heterogeneous enhancement. Bone erosion is a feature seen in more than half of hemangiopericytoma cases[4,5]. On MRI, hemangiopericytomas are heterogeneous, predominantly isointense masses on T1- and T2-weighted images, show prominent internal vessel voids, and heterogeneously enhance on contrast-enhanced images (Figure 2). Approximately one-third of hemangiopericytomas exhibit a narrow base of dural attachment, with the remaining two-thirds showing broad-based attachment with a dural tail sign[6]. Surgical resection is the primary treatment for this tumor. Preoperative embolization can aid in reducing operative blood loss. Postoperative radiation therapy is recommended[7].

GLIOSARCOMA

Gliosarcoma is a rare cerebral tumor closely related to glioblastoma in terms of both its clinical and therapeutic characteristics. Gliosarcoma consists of gliomatous and sarcomatous elements (Figure 3A)[8].

Gliosarcoma usually occurs in middle aged adults. The ability of gliosarcoma to metastasize to other locations in the neuroaxis is well known[9].

Radiation-induced gliosarcoma may appear at the site of a treated intracranial neoplasm and should be considered in the differential diagnosis of a recurrent mass[10].

On CT, gliosarcoma tends to present as a peripherally located, sharply defined, round or lobulated, isodense or hyperdense solid mass with heterogeneous or ring enhancement due to a fibrous component. On MRI, the tumors tend to be well-defined, demonstrating either an inhomogeneous or cystic appearance with surrounding vasogenic edema. On T2-weighted images, intermediate

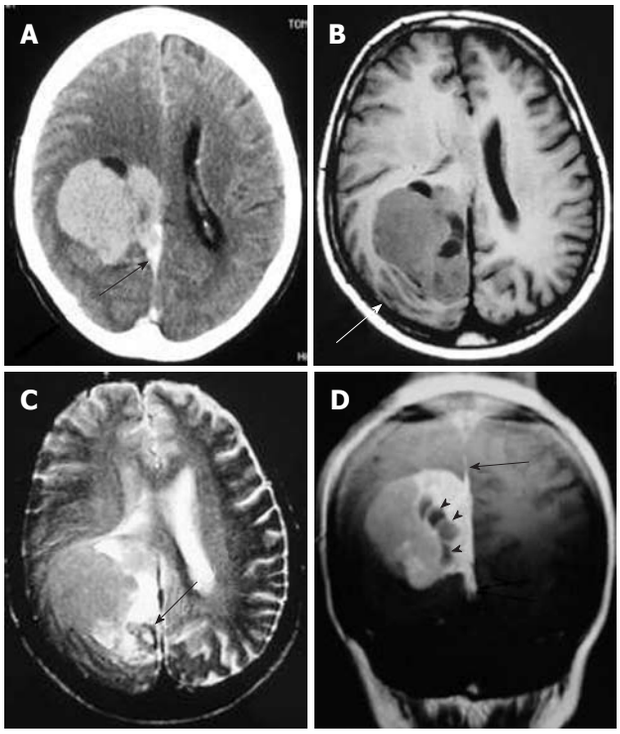

Figure 1 Solitary fibrous tumor. Post-contrast computed tomography. A: A dural-based lobulated mass with dural tail enhancement (arrow); B: Axial T1-weighted magnetic resonance (MR) image shows an extra-axial mass, isointense to the gray matter compressing the adjacent cortical convolutions (arrow); C: Axial T2-weighted MR image shows that the mass has intermediate signal intensity. Note the peritumoral cysts with high signal intensity (arrow); D: On the post-contrast, T1-weighted MR image, the mass shows intense enhancement, intra-tumoral cysts (arrowheads) and dural tail sign (arrow).

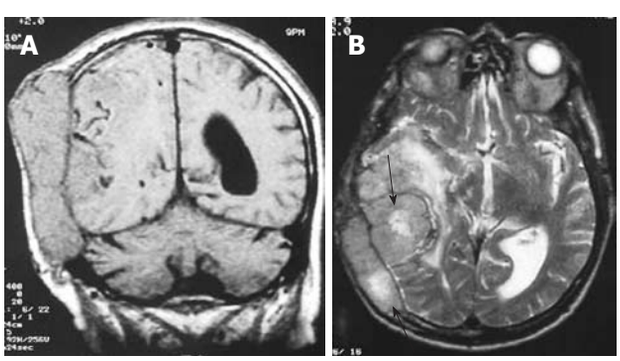

Figure 2 Hemangiopericytoma. A: The coronal T1-weighted magnetic resonance (MR) image shows an extra-axial isointense mass with internal flow voids and calvarial destruction; B: On the axial, T2-weighted MR image the mass remains isointense with internal areas of hyperintensity and moderate peritumoral edema.

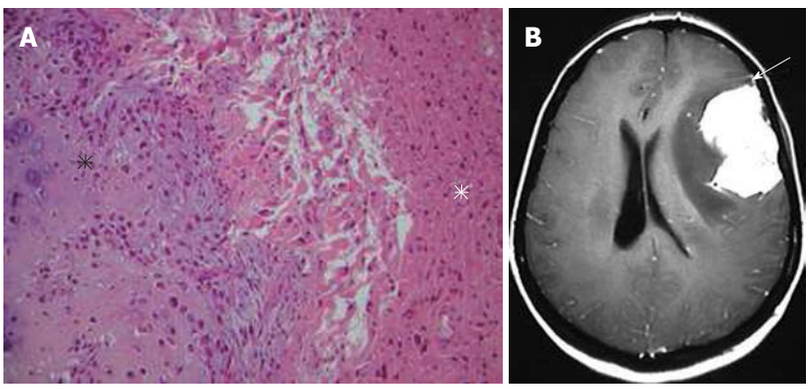

Figure 3 Gliosarcoma. A: Pathological image showing an area with features of osteogenic sarcoma (black asterisk) adjacent to the glial component of the tumor (white asterisk) (hematoxylin-eosin, original magnification × 100); B: On the axial, post-contrast T1-weighted magnetic resonance image, the tumor shows intense homogeneous enhancement. Note the close relation of the mass with the dura, which is enhanced in a way mimicking meningioma (arrow).

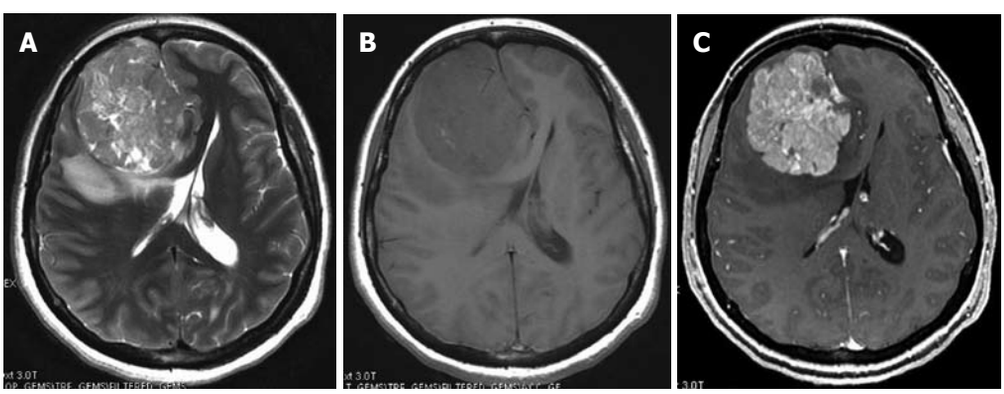

Figure 4 Dural metastasis in a 36-year-old woman with breast carcinoma. A: Axial T2-weighted image shows a large extra-axial frontal heterogeneous mass; B: On T1-weighted magnetic resonance (MR) image the mass is isointense with the gray matter; C: Axial post-contrast T1-weighted MR image shows an extra-axial strongly enhanced lesion broad based to the falx mimicking meningioma.

signal intensity with surrounding edema is visible. The signal intensity of the tumor is similar to gray matter but is hypointense relative to other glial neoplasms. Post-contrast T1-weighted images show intense tumor enhancement, often with a ring-like appearance (Figure 3B)[11]. Postsurgical treatment of gliosarcoma includes adjuvant radiotherapy with concurrent administration of temozolomide[12].

LEIOMYOSARCOMAS

Leiomyosarcomas of the CNS are extremely rare; however, they are becoming more prevalent in immunocompromised patients. Patients with acquired immunodeficiency syndrome are known to exhibit an increased incidence of smooth muscle tumors associated with Epstein virus. Intracranial leiomyosarcoma reveals dural masses or a skull-base location. Leiomyosarcoma should be included in the differential diagnosis of extra-axial CNS lesions in human immunodeficiency virus (HIV)-infected patients[13].

DURAL METASTASES

Metastases to the dura constitute one of the least frequent patterns of neoplastic spread to the craniospinal axis. The neoplasms arise either by direct extension from skull metastases or by hematogeneous spread. Breast cancer, prostate cancer, adenocarcinoma of the lung, and renal cell carcinoma are the most common. Meningeal metastasis from medulloblastoma is also a well known entity[14]. Typically, these tumors produce MR images with increased signals on T2-weighted images, often with an enhancing dural tail mimicking a meningioma (Figure 4). Patients with a single resectable symptomatic dural metastasis, controlled systemic cancer, and acceptable surgical risk should be considered for resection as first-line therapy.

HODGKIN'S DISEASE

Intracranial Hodgkin's disease occurs by direct spread from the bones of the skull or in continuity with meningeal deposits that gained access to the skull *via* the cranial nerves[15,16]. The involvement of bone in Hodgkin's lymphomas usually occurs in the late stage of the disease. Extension of the scalp mass to both the epidural space and subcutaneous soft tissue is usually seen.

Regarding the histology of Hodgkin's disease with intracranial relapse, both a nodular sclerosis and mixed cellularity variety have been described. In the majority

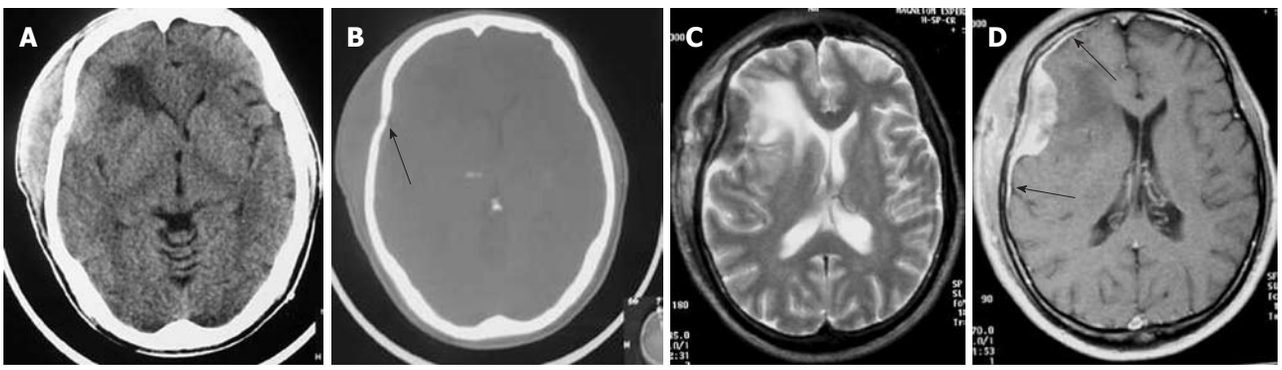

Figure 5 Non-Hodgkin Lymphoma. The axial non-contrast computed tomography. A: A hyperdense extra-axial mass extending to both sides of the frontoparietal bone; B: Bone window setting depict lytic lesion of the calvarium (arrow); C: On axial T2-weighted magnetic resonance images, the mass appears isointense with peritumoral edema; D: After the administration of contrast media, a strong homogeneous enhancement is seen with a dural tail (arrows).

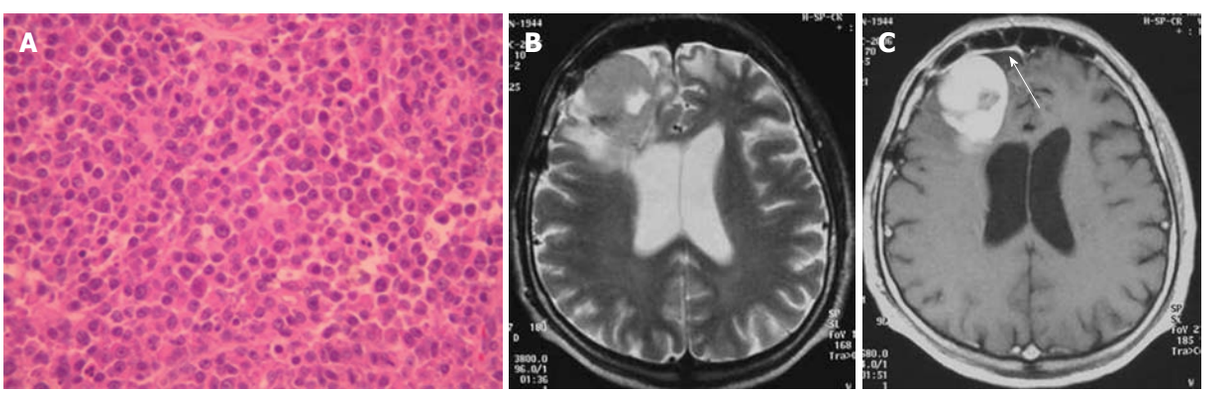

Figure 6 Plasmocytoma in a 62-year-old patient. A: Typical plasma cell morphology hematoxylin-eosin stain; B: Axial T2-weighted magnetic resonance images show an isointense frontal mass with peritumoral edema compressing the right ventricle; C: The axial post-contrast image shows intense homogeneous enhancement of the lesion with a dural tail (arrow).

of reported skull lymphomas, the mass is hyperdense on unenhanced CT and shows marked enhancement on post-contrast studies. Destruction of the bone may not be seen in some cases because the characteristic permeating growth pattern of lymphoma is a large soft tissue component and very little bone destruction. Bone window setting is useful for depicting tiny lytic lesions of the bony calvarium (Figure 5A and B).

On MRI, the densely cellular deposits of lymphoma most often do not show high signal intensity on T2-weighted images and typically remain hypo- to isointense on all pulse sequences. Post-contrast T1-weighted images show either homogeneous or inhomogeneous dense enhancement. Linear dural enhancement is usually seen on both sides of the dural mass (dural tail) and, although it is an extra-axial mass, white matter edema is usually present (Figure 5C-D)[17]. Radiotherapy and chemotherapy are the treatment of choice.

PLASMOCYTOMA

Plasmocytoma rarely involve the CNS as dural-based lesions[18]. Careful systemic evaluation should be made in such a presentation to rule out multiple myeloma which would require different management and prognosis. Some patients develop bone marrow biopsy-proven myeloma within months of the initial diagnosis of CNS plasmocytoma[19]. Histopathological examination of the mass after excision shows multiple myeloma immunopositive for IgG, kappa light chain, and CD38 (Figure 6A). On CT, plasmacytomas are extra-axial masses without calcification or bone involvement, and they are usually high-density lesions. An isointense lesion is revealed on both T1- and T2-weighted images. On post-contrast T1-weighted images, intense homogeneous contrast enhancement is demonstrated with a dural tail sign mimicking meningioma (Figure 6B and C)[20]. Systemic chemotherapy and radiotherapy are recommended after surgical excision of the mass.

ROSAI-DORFMAN DISEASE

Rosai-Dorfman disease is also known as sinus histiocytosis with massive lymphadenopathy. The disease commonly presents as massive, painless, bilateral lymph node enlargement in the neck with fever. Rarely, sites other than the lymph nodes are involved, including the CNS, eyes, upper respiratory tract, skin, and head and neck region[21]. CNS Rosai-Dorfman most commonly involves patients between 20-40 years.

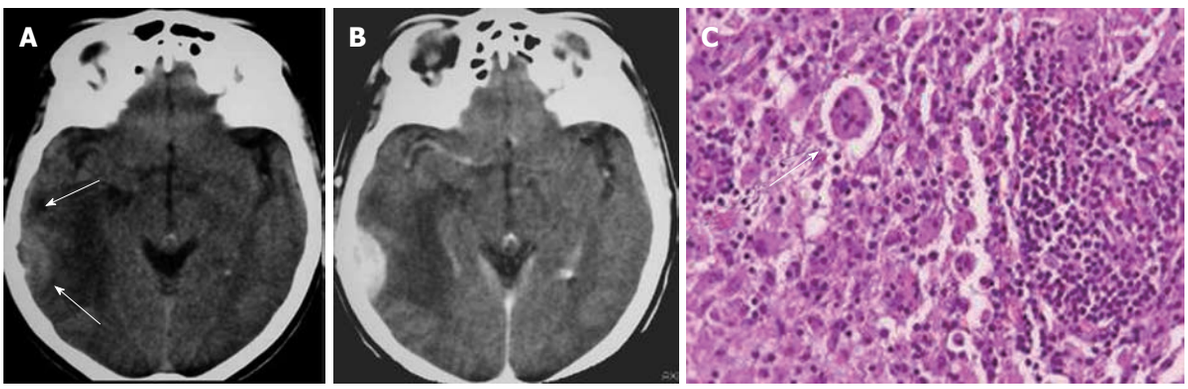

Figure 7 Rosai-Dorfman disease. A: The non-contrast computed tomography (CT) shows a peripheral, poorly marginated, hyperdense mass with peritumoral edema (arrows); B: Post-contrast CT shows a convex, homogeneously enhanced extra-axial mass; C: Pathologic image of Rosai-Dorfman disease with a characteristic finding of emperipolesis (arrow).

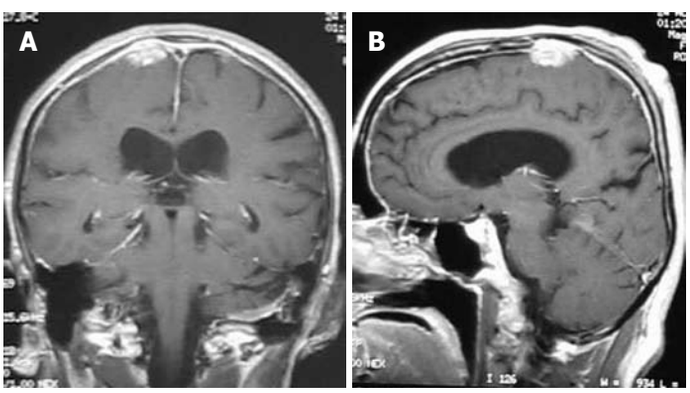

Figure 8 Neurosarcoidosis. Coronal (A) and sagittal (B) T1-weighted magnetic resonance post-contrast images show an enhancing dural-based lesion. Also, note the enhancement of the dura along the convexity.

Symptoms of intracranial disease include seizures, headache and weakness. Over 90% of CNS Rosai-Dorfman cases involve the leptomeninges. Histopathologically, the dura is thickened, fibrotic, and contains a variable density of chronic inflammatory cells, dominated by lymphocytes and plasma cells. The finding of emperipolesis is characteristic of Rosai-Dorfman disease of the leptomeninges, but in 30% of cases this feature is not identified[22].

On CT and MRI, Rosai-Dorfman disease presents as dural-based, epidural or subdural, contrast-enhancing masses that often elicit vasogenic edema in the underlying cerebral cortex and white matter (Figure 7A and B). The dural mass shows low signal intensity on T2-weighted images. Thus, clinically and radiologically, the disease is thought to represent meningioma[23]. The definitive diagnosis of Rosai-Dorfman disease involving the leptomeninges is established by biopsy (Figure 7C) and pathological examination. Treatment should be based on clinical manifestations. Many lesions are asymptomatic, heal spontaneously, and do not require treatment[24].

NEUROSARCOIDOSIS

Neurosarcoidosis occurs in approximately 5% of patients with sarcoidosis[25]. Diagnosis is based on the documentation of systemic sarcoidosis in the absence of other neurological disease. The histopathological hallmarks of neurosarcoidosis include epithelioid granulomas without caseation or staining for infectious agents. Imaging findings of neurosarcoidosis include pachymeningeal/dural masses, leptomeningeal involvement, enhancing brain parenchymal lesion, and cranial nerve involvement.

A dural-based mass is one of the least common manifestations of neurosarcoidosis.

Lesions typically homogeneously enhance on contrast-enhanced T1-weighted images (Figure 8). Variable amounts of vasogenic edema can also be seen in the white matter adjacent to the mass[26,27]. Differential considerations include lymphoma and idiopathic hypertrophic cranial pachymeningitis. Steroid therapy is usually indicated. Infliximab is a valuable pharmacological agent in the management of patients with refractory and disabling neurosarcoidosis[28].

MELANOCYTIC NEOPLASMS

Melanocytes are normally present in the intracranial leptomeninges, usually in the posterior cerebral fossa, and can give rise to benign (meningeal melanocytoma) or malignant (malignant melanoma) tumors. Most reported cases of meningeal melanocytomas are located in the posterior fossa and spinal cord, although large supraten-

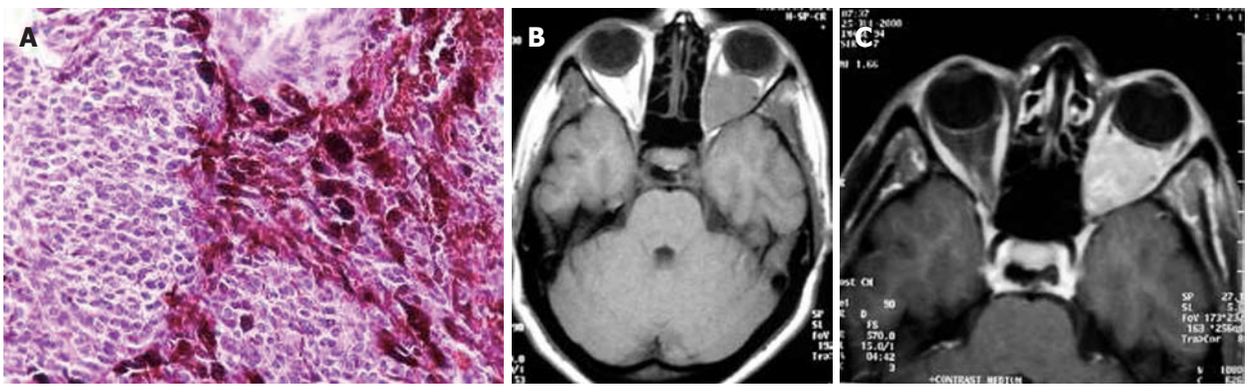

Figure 9 Melanocytic tumor. A: Photomicrograph of the mass. The neoplasm contains sheets of cells, many of which contain dark brown melanin pigment (hematoxylin-eosin, × 400); B: T1-weighted magnetic resonance and post-contrast; C: T1-weighted MR images show a left intraconal mass with intermediate signal intensity that homogeneously enhances.

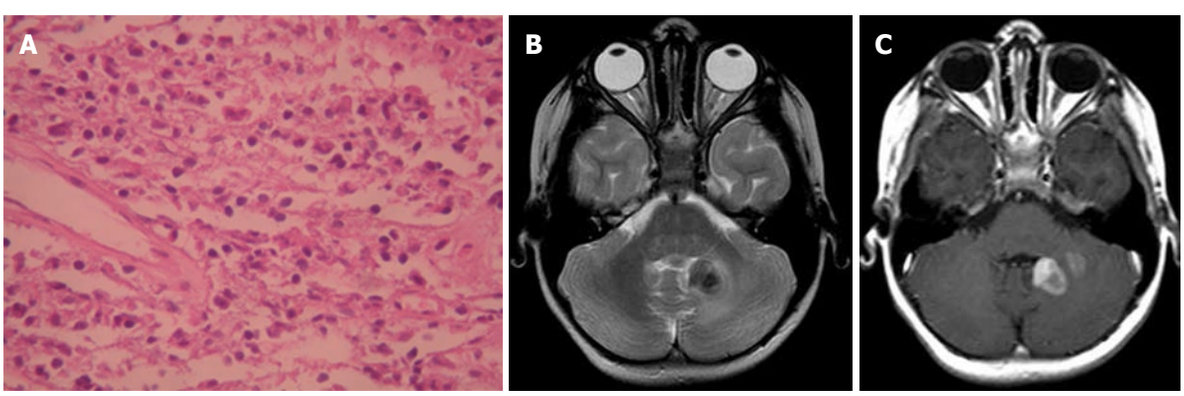

Figure 10 Plasma cell granuloma in a 4-year-old girl. A: Pathologic image. The fibrosis and infiltration is composed of lymphocytes, plasmocytes and histiocytes (hematoxylin-eosin stain); B: Axial T2-weighted magnetic resonance (MR) image shows a hypointense left cerebellar lesion adjacent to the 4th ventricle with moderate peritumoral edema; C: Post-contrast T1-weighted MR image shows heterogeneous enhancement of the lesion.

torial meningeal melanocytomas mimicking a convexity meningioma have been reported[29].

Histologically, most melanocytomas are spindle cell neoplasms, although epithelioid cytology may dominate in some cases. Tumor cells grow in sheets, nests, or fascicles (Figure 9A).

On CT, primary melanocytic lesions appear as well-circumscribed, isoattenuating to hyperattenuating, extra-axial tumors with homogeneous enhancement. Even if there is no hyperostosis, the neoplasms can mimic meningioma[30]. MRI demonstrates variable signal intensity on T1- and T2-weighted images, in proportion to the amount of melanin within the tumor. Therefore, melanocytic neoplasms are isointense or hyperintense to adjacent normal brain tissue on T1-weighted images and isointense or hypointense on T2-weighted images. The neoplasms enhance after intravenous administration of contrast material (Figure 9B and C)[31]. Complete surgical excision of the tumor is the treatment of choice. The role and efficacy of radiotherapy and chemotherapy remain controversial.

PLASMA CELL GRANULOMA

Plasma cell granuloma is a rare form of idiopathic inflammatory pseudotumor often characterized by non-neoplastic proliferation of plasma cells clinically mimicking a neoplastic process. Pseudotumors of the CNS, however, are exceptional and rare. In reported cases, these reactive lesions occurred primarily in adults, usually presenting as discrete tumors arising from the leptomeninges or dura. Histologically, the granulomas are populated by a polytypic population of mature plasma cells, plasmatoids, and small non-transformed lymphocytes in a background of variable fibrosis, fibroblasts, and entrapped leptomeningeal cells (Figure 10A)[32].

On CT, the mass is usually a well-circumscribed area of increased density markedly enhanced with the administration of contrast. On MRI, the mass has slightly high signal intensity on T1-weighted images and marked low signal intensity on T2-weighted images. The granuloma is usually heterogeneously enhanced with gadolinium-DTPA (Figure 10B and C). Parenchymal involvement has been reported[33].

CONCLUSION

The differential diagnosis of dural-based lesions in the brain varies from incidental and benign to symptomatic and malignant lesions. The above mentioned entities

involving the dura are rare and almost always diagnosed after tissue is obtained because of their clinical and radiographic similarity to meningiomas. These lesions can closely resemble meningiomas in terms of signal characteristics, enhancement pattern, and location. Imaging characteristics alone can be misleading; neuropathological support is essential for accurate diagnosis.

A thorough clinical evaluation can reveal likely diagnostic possibilities. In the presence of a heterogeneous dural-based mass with prominent internal vessels and bone erosion, the case of hemangiopericytoma should be considered. Leiomyosarcomas should be included in the differential diagnosis of dural-based lesions in HIV-infected patients.

Careful vigilance in patients with a history of cancer, presenting with new symptoms or imaging evidence of dural-based lesions, should raise the possibility of dural metastasis.

The diagnosis of lymphoma should be considered for lesions affecting the dura in high-risk immunocompromised patients. The presence of an apparent dural tail can be seen in a lymphoma. The absence of hyperostosis helps differentiate lymphoma from meningioma.

Hypercalcemia, hyperproteinemia, and serum gamma globulin peak in a patient with an extra-axial dural mass should raise the possibility of plasmocytoma. Rosai-Dorfman disease should be considered when a young adult with painless neck lymphadenopathy, fever and anemia presents with a dural mass. The already known history of systemic sarcoidosis in a patient with a dural mass and leptomeningeal enhancement is suggestive of neurosarcoidosis. Awareness that these lesions involve the dura may facilitate radiological and intra-operative recognition and, in some cases, preclude unnecessary additional surgery [34].

REFERENCES

1 **Caroli E**, Salvati M, Orlando ER, Lenzi J, Santoro A, Giangaspero F. Solitary fibrous tumors of the meninges: report of four cases and literature review. *Neurosurg Rev* 2004; **27**: 246-251

2 **Westra WH**, Gerald WL, Rosai J. Solitary fibrous tumor. Consistent CD34 immunoreactivity and occurrence in the orbit. *Am J Surg Pathol* 1994; **18**: 992-998

3 **Bisceglia M**, Galliani C, Giannatempo G, Lauriola W, Bianco M, D'angelo V, Pizzolitto S, Vita G, Pasquinelli G, Magro G, Dor DB. **Solitary fibrous tumor of the central nervous** system: a 15-year literature survey of 220 cases (August 1996-July 2011). *Adv Anat Pathol* 2011; **18**: 356-392

4 **Chiechi MV**, Smirniotopoulos JG, Mena H. Intracranial hemangiopericytomas: MR and CT features. *AJNR Am J Neuroradiol* 1996; **17**: 1365-1371

5 **Akiyama M**, Sakai H, Onoue H, Miyazaki Y, Abe T. Imaging intracranial haemangiopericytomas: study of seven cases. *Neuroradiology* 2004; **46**: 194-197

6 **Fountas KN**, Kapsalaki E, Kassam M, Feltes CH, Dimopoulos VG, Robinson JS, Smith JR. Management of intracranial meningeal hemangiopericytomas: outcome and experience. *Neurosurg Rev* 2006; **29**: 145-153

7 **Viswanathan A**, Demonte F. Tumors of the meninges. *Handb Clin Neurol* 2012; **105**: 641-656

8 **Meis JM,** Martz KL, Nelson JS. Mixed glioblastoma multiforme and sarcoma: a clinicopathologic study of 26 Radiation Therapy Oncology Group cases. *Cancer* 1991; **67:** 2342-2349

9 **Witwer BP,** Salamat MS, Resnick DK. **Gliosarcoma metastatic** to the cervical spinal cord: case report and review of the literature. *Surg Neurol* 2000; **54:** 373-378

10 **Lach M**, Wallace CJ, Krcek J, Curry B. Radiation-associated gliosarcoma. *Can Assoc Radiol J* 1996; **47**: 209-212

11 **Dwyer KW**, Naul LG, Hise JH. Gliosarcoma: MR features. *J Comput Assist Tomogr* 1996; **20**: 719-723

12 **Han SJ**, Yang I, Ahn BJ, Otero JJ, Tihan T, McDermott MW, Berger MS, Prados MD, Parsa AT. Clinical characteristics and outcomes for a modern series of primary gliosarcoma patients. *Cancer* 2010; **116**: 1358-1366

13 **Lerdlum S**, Lalitanantpong S, Numkarunarunrote N, Chaowanapanja P, Suankratay C, Shuangshoti S. MR imaging of CNS leiomyosarcoma in AIDS patients. *J Med Assoc Thai* 2004; **87** Suppl 2: S152-S160

14 **Maroldi R**, Ambrosi C, Farina D. Metastatic disease of the brain: extra-axial metastases (skull, dura, leptomeningeal) and tumour spread. *Eur Radiol* 2005; **15**: 617-626

15 **Hirmiz K,** Foyle A, Wilke D, Burrell S, Brownstone R, Ago C, Pahil R, Couban S. Intracranial presentation of systemic Hodgkin's disease. *Leuk Lymphoma* 2004; **45:** 1667-1671

16 **Guermazi A**, Brice P, de Kerviler E E, Fermé C, Hennequin C, Meignin V, Frija J. Extranodal Hodgkin disease: spectrum of disease. *Radiographics* 2001; **21**: 161-179

17 **Thurnher MM**, Rieger A, Kleibl-Popov C, Schindler E. Malignant lymphoma of the cranial vault in an HIV-positive patient: imaging findings. *Eur Radiol* 2001; **11**: 1506-1509

18 **Sahin F**, Saydam G, Ertan Y, Calli C, Dönmez A, Tombuloglu M. Dural plasmacytoma mimicking meningioma in a patient with multiple myeloma. *J Clin Neurosci* 2006; **13**: 259-261

19 **Haegelen C**, Riffaud L, Bernard M, Carsin-Nicol B, Morandi X. Dural plasmacytoma revealing multiple myeloma. Case report. *J Neurosurg* 2006; **104**: 608-610

20 **Gallina P**, Mascalchi M, Mouchaty H, Buccoliero A, Perrini P. Misleading imaging features of intracranial dural plasmacytoma: report of two cases. *Br J Neurosurg* 2004; **18**: 643-646

21 **Wu M**, Anderson AE, Kahn LB. **A report of intracranial Ro**sai-Dorfman disease with literature review. *Ann Diagn Pathol* 2001; **5**: 96-102

22 **Siadati A**, Powell SZ, Shahab I, Valadka AB, Parker JR. Pathologic quiz case: a 48 year-old woman with a dural-based intracranial tumor. *Arch Pathol Lab Med* 2001; **125**: 1115-1116

23 **Konishi E**, Ibayashi N, Yamamoto S, Scheithauer BW. Isolated intracranial Rosai-Dorfman disease (sinus histiocytosis with massive lymphadenopathy). *AJNR Am J Neuroradiol* 2003; **24**: 515-518

24 **Hadjipanayis CG**, Bejjani G, Wiley C, Hasegawa T, Maddock M, Kondziolka D. Intracranial Rosai-Dorfman disease treated with microsurgical resection and stereotactic radiosurgery. Case report. *J Neurosurg* 2003; **98**: 165-168

25 **Stern BJ**. Neurological complications of sarcoidosis. *Curr Opin Neurol* 2004; **17**: 311-316

26 **Lexa FJ**, Grossman RI. MR of sarcoidosis in the head and spine: spectrum of manifestations and radiographic response to steroid therapy. *AJNR Am J Neuroradiol* 1994; **15**: 973-982

27 **Christoforidis GA,** Spickler EM, Recio MV, Mehta BM. MR of CNS Sarcoidosis: Correlation of Imaging Features to Clinical Symptoms and Response to Treatment. *AJNR Am J Neuroradiol* 1999; **20:** 655-669

28 **Toth C**, Martin L, Morrish W, Coutts S, Parney I. Dramatic MRI improvement with refractory neurosarcoidosis treated with infliximab. *Acta Neurol Scand* 2007; **116**: 259-262

29 **Beseoglu K**, Knobbe CB, Reifenberger G, Steiger HJ, Stummer W. Supratentorial meningeal melanocytoma mimicking a convexity meningioma. *Acta Neurochir* (Wien) 2006; **148**: 485-490

30 **Chen CJ**, Hsu YI, Ho YS, Hsu YH, Wang LJ, Wong YC. Intracranial meningeal melanocytoma: CT and MRI. *Neuroradiology* 1997; **39**: 811-814
31 **Naul LG**, Hise JH, Bauserman SC, Todd FD. CT and MR of meningeal melanocytoma. *AJNR Am J Neuroradiol* 1991; **12**: 315-316
32 **Häusler M**, Schaade L, Ramaekers VT, Doenges M, Heimann G, Sellhaus B. Inflammatory pseudotumors of the central nervous system: report of 3 cases and a literature review. *Hum Pathol* 2003; **34**: 253-262
33 **Ozüm U**, Ozer H, Karadağ O, Polat N. Intracranial plasma cell-granuloma with extensive ossification. *Br J Neurosurg* 2006; **20**: 153-156
34 **Johnson MD**, Powell SZ, Boyer PJ, Weil RJ, Moots PL. Dural lesions mimicking meningiomas. *Hum Pathol* 2002; **33**: 1211-1226

S- Editor Cheng JX **L- Editor** Webster JR **E- Editor** Xiong L

World Journal of Radiology

Online Submissions: http://www.wjgnet.com/1949-8470office
wjr@wjgnet.com
doi:10.4329/wjr.v4.i3.83

World J Radiol 2012 March 28; 4(3): 83-89
ISSN 1949-8470 (online)

ORIGINAL ARTICLE

Cognitive and functional status after vein of Galen aneurysmal malformation endovascular occlusion

Jason A Ellis, Lauren Orr, Paul C McCormick Ⅱ, Richard CE Anderson, Neil A Feldstein, Philip M Meyers

Jason A Ellis, Lauren Orr, Paul C McCormick Ⅱ, Richard CE Anderson, Neil A Feldstein, Philip M Meyers, Department of Neurological Surgery, Columbia University Medical Center, NY 10032, United States
Philip M Meyers, Department of Radiology, Columbia University Medical Center, NY 10032, United States
Author contributions: Ellis JA acquired data, provided analysis and interpretation of the data, and drafted this article; Orr L acquired data and drafted this article; McCormick Ⅱ PC acquired data and drafted this article; Anderson RCE critically revised this article; Feldstein NA critically revised this article; Meyers PM critically revised this article and approved the final version for submission.
Correspondence to: Jason A Ellis, MD, Department of Neurological Surgery, Neurological Institute of New York, Columbia University Medical Center, 710 West 168th Street, NY 10032, United States. jae2109@columbia.edu
Telephone: +1-617-2567072 Fax: +1-212-305026
Received: September 5, 2011 Revised: January 2, 2012
Accepted: January 9, 2012
Published online: March 28, 2012

Abstract

AIM: To study the clinical outcomes of treating vein of Galen aneurysmal malformations (VGAM), we assessed our patient cohort using standardized cognitive and functional measures.

METHODS: A retrospective review of patients with VGAM treated by a single practitioner between 2003 and 2009 was performed for this study. In addition to routine clinical assessment, all patients were evaluated for cognitive and functional impairment using validated measures including the Neurobehavioral Rating Scale-Revised, the Bicêtre outcome score, and the Barthel index.

RESULTS: Five patients underwent combined transarterial and transvenous embolization of their VGAM during the study period. VGAMs were classified based on angioarchitecture as either choroidal (1/5) or mural (4/5) according to the classification scheme of Lasjaunias. In total, 13 embolization procedures were performed consisting of 1 to 3 treatment stages per patient. Complete or near complete occlusion was achieved in 4 patients, while subtotal occlusion was achieved in 1 patient. During follow-up (median 62.6 mo), all patients were either unchanged or cognitively and neurologically intact.

CONCLUSION: VGAM can be safely and effectively treated by staged transarterial and transvenous embolization. Using this strategy, excellent long-term cognitive and functional outcomes can be achieved.

Key words: Cognition; Embolization; Endovascular; Hemorrhage; Interventional neuroradiology; Neurological development; Outcomes; Vein of Galen aneurysmal malformation

Peer reviewer: Paul V Puthussery, MD, DMRD, MNAMS, DNB, Assistant Professor, Department of Radiodiagnosis, Government Medical College, Kochi 683571, India

Ellis JA, Orr L, McCormick Ⅱ PC, Anderson RCE, Feldstein NA, Meyers PM. Cognitive and functional status after vein of Galen aneurysmal malformation endovascular occlusion. *World J Radiol* 2012; 4(3): 83-89 Available from: URL: http://www.wjgnet.com/1949-8470/full/v4/i3/83.htm DOI: http://dx.doi.org/10.4329/wjr.v4.i3.83

INTRODUCTION

Vein of Galen aneurysmal malformations (VGAMs) are a group of congenital arteriovenous fistulas that comprise up to 37% of intracranial vascular lesions in the pediatric population[1]. Rather than a brain arteriovenous malformation of the true vein of Galen, VGAMs rep-

resent an arteriovenous fistula with drainage to a persistent embryonic vein, the median prosencephalic vein of Markowski[2]. These lesions can present with high-output congestive heart failure, seizures, failure to thrive, hydrocephalus, and brain hemorrhage. High surgical morbidity and mortality, exceeding 90% in some series, has led to the development of endovascular techniques that more safely and effectively treat these lesions[3-6]. The use of staged procedures utilizing both transarterial and transvenous catheter access routes to deliver a variety of solid and liquid embolic materials have enabled high rates of anatomic occlusion with good clinical outcomes. In large series, favorable outcomes after endovascular treatment are seen in approximately 60%-75% of patients[7-13].

Despite advancements in the endovascular treatment of VGAMs, neurological development and cognitive function may be impaired in survivors. However, only a limited number of reports address this issue directly[7,8,14]. Although transvenous techniques are potentially curative in many cases, some investigators have expressed concern that transvenous embolization is associated with worse cognitive outcomes than transarterial embolization and should be avoided. To assess this concern, we retrospectively reviewed our experience in treating VGAMs using transvenous methodology, with particular attention to clinical cognitive assessments during ongoing follow-up.

MATERIALS AND METHODS

Between 2003 and 2009, five pediatric and adult patients with symptomatic vein of Galen aneurysmal malformations underwent evaluation and transvenous endovascular treatment at our institution. A retrospective review of all patient records, including office and hospital charts as well as of available diagnostic cerebral angiograms and other imaging studies, was performed in accordance with Institutional Review Board stipulations and approval. Baseline clinical characteristics, lesion classification, endovascular surgery details, periprocedural complications, and follow-up data were collected for this review (Tables 1 and 2).

In addition to routine clinical and neurological examination, the cognitive and functional status of each patient was evaluated during the most recent post-embolization follow-up office visit. The executive/cognitive items from the Neurobehavioral Rating Scale-Revised (NRS-R)[15,16], the Bicêtre outcome score[8], and the Barthel index[17] were used in the evaluation of each patient. Factors loading under executive/cognitive in the NRS-R included patient difficulties with planning, mental flexibility, memory, disorientation, initiative or motivation, self-appraisal, conceptual disorganization, and oral comprehension[15]. As is standard for the NRS-R, each patient was graded on a four-tier scale including absent, mild, moderate, or severe difficulty for each item evaluated. The Bicêtre outcome score (BOS) is a global clinical measure for the assessment of cognitive outcome. As described by Lasjaunias *et al*[8], patients with BOS 3-5 are neurologically normal, those with BOS 2 are moderately retarded, while patients with BOS 1 are severely retarded. For small children, parents were queried regarding specific cognitive and functional impairments.

RESULTS

Five patients underwent catheter cerebral arteriography and transvenous embolization of their VGAM during the six-year study period (Table 1). The cohort underwent 13 embolization procedures including 1 to 3 treatment stages per patient. VGAMs were initially diagnosed in the neonatal period (2/5), in early childhood (2/5), and during adulthood (1/5). One patient (Patient 5) originally presented at the age of 21 mo with macrocephalus and cranial bruit, but underwent definitive endovascular embolization as an adult at the age of 32 years for complaints of progressive dementia, severe headaches and intractable seizures. The two neonates presented acutely with congestive heart failure (CHF) while the other patients presented in a delayed fashion with headache, macrocephalus, cranial bruit, prominent scalp veins, or progressive presenile dementia. A variety of preliminary diagnostic imaging modalities were employed including head ultrasound, skull radiography, head computed tomography, and brain magnetic resonance imaging (Figure 1).

Diagnostic catheter cerebral angiography was performed in all patients for treatment planning and as a guide to endovascular therapy. VGAMs were classified based on angioarchitecture as either choroidal (1/5) or mural (4/5) according to the classification scheme of Lasjaunias[8,11,18,19]. Choroidal lesions are characterized by an extensive arterial network interposed between larger arterial feeders prior to high flow drainage into the venous malformation (Figure 2A-D). Mural lesions do not have an interposed arterial network and consist of one or more direct fistulas to the median prosencephalic vein (Figure 2E and F).

All patients were placed under general anesthesia prior to endovascular treatment. Staged embolizations *via* combined transarterial and transvenous routes were then performed with systemic heparinization (Table 2). In one patient (Patient 3) who underwent a single-staged embolization, catheter access to the median prosencephalic vein was achieved by passing the microcatheter tip from the arterial side into the recipient draining vein. Thrombogenic platinum coils and a liquid embolic agent (Trufill® NBCA, Codman Cordis; Raynham, MA, United States) were primarily used to occlude the fistulas comprising the malformation.

There were a total of three periprocedural complications in two patients during the study period (Table 2). Patient 1 developed a small, subclinical left parietal infarct and subsequently a small, asymptomatic intraventricular hemorrhage (IVH) after the third stage of embolization. Patient 3 developed a small, subclinical germinal matrix hemorrhage. The left parietal infarct (Patient 1) was thought to be due to stagnation and retrograde thrombo-

Table 1 Patient characteristics

Patient	Age[1]	Gender	Presenting symptoms	Initial diagnostic imaging
1	Birth/5 d	Male	Congestive heart failure, cranial bruit	Non-contrast head computed tomography
2	5 mo/8 mo	Male	Macrocephalus, cranial bruit	Magnetic resonance imaging brain +/- contrast
3	Prenatal/5 d	Female	Congestive heart failure	Prenatal ultrasound
4	24 yr/27 yr	Male	Face pain, dementia	Magnetic resonance imaging brain +/- contrast
5	21 mo/32 yr	Female	Macrocephalus, cranial bruit	Skull X-ray

[1]At presentation/ at stage 1 embolization

Table 2 Galen aneurysmal malformations endovascular occlusion

Patient	Angio-architecture	*n*[1]	Endovascular access	Extent of occlusion	Clinical endpoint	Embolic agents	Periprocedural complications
1	Choroidal	3	Transarterial and transvenous	Complete	Normalization of cardiac function	Fibered and non-fibered platinum coils, N-butyl cyanoacrylate	Left parietal infarct post stage 2 embolization, consumptive coagulopathy and IVH post stage 3 embolization
2	Mural	3	Transarterial and transvenous	Complete	Normalization of head circumference	Fibered and non-fibered platinum coils, NBCA, Berenstein liquid coils	None
3	Mural	1	Transarterial and transvenous	Subtotal	Normalization of cardiac function	Fibered and non-fibered platinum coils	Small germinal matrix hemorrhage 21 d post embolization
4	Mural	3	Transarterial and transvenous	Complete	Resolution of vascular dementia and hemifacial pain	Fibered and non-fibered platinum coils, NBCA	None
5	Mural	3	Transarterial and transvenous	Near complete	Resolution of vascular dementia, seizures, and headaches	Fibered and non-fibered platinum coils, NBCA, hydrogel coils, polyvinyl alcohol, ethanol	None

[1]At presentation/ at stage 1 embolization. IVH: Intraventricular hemorrhage.

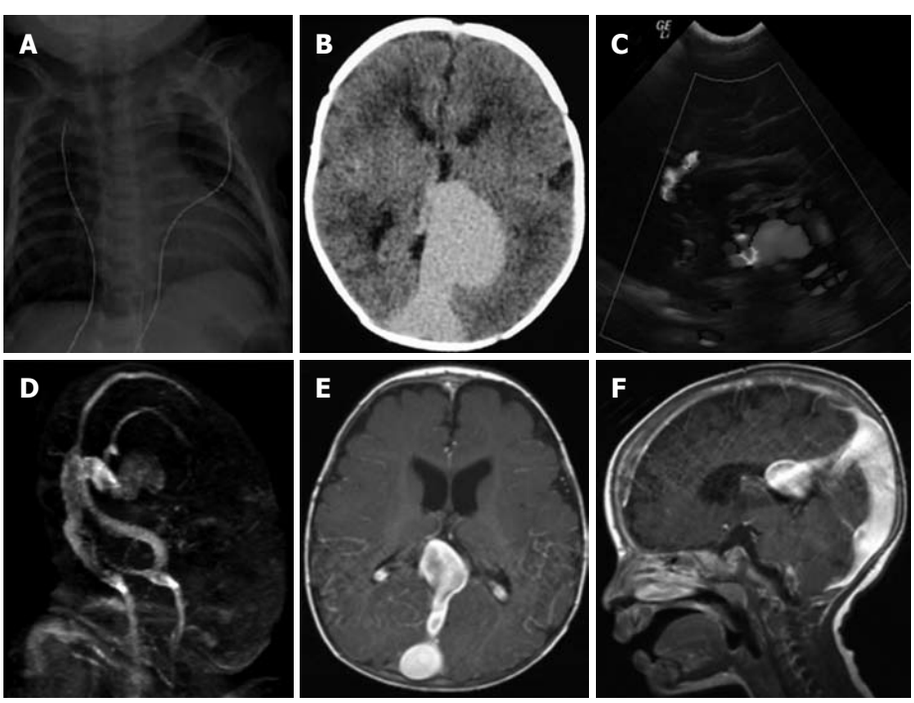

Figure 1 Preliminary diagnostic imaging in Galen aneurysmal malformations patients. A: Portable chest radiograph in a newborn (Patient 1) with clinical signs of congestive heart failure and a cranial bruit demonstrates cardiomegaly and pulmonary vascular congestion; B: A non-contrast head computed tomography shows an enlarged midline vascular structure in the posterior fossa consistent with a Galen aneurysmal malformations (VGAM); C, D: In another patient (Patient 3) who presented similarly, color Doppler ultrasound (C) indicates the presence of a posterior midline vascular pouch subsequently shown by magnetic resonance (MR) venography to be a VGAM (D); E, F: Alternatively, contrast-enhanced brain MR imaging was the initial diagnostic imaging used to diagnose a VGAM in Patient 2 who presented with macrocephalus and cranial bruit.

sis of an embolized arterial feeder. The IVH (Patient 1) occurred in the setting of a consumptive coagulopathy and was treated by aggressive resuscitation with platelets and fresh frozen plasma. The germinal matrix hemorrhage (Patient 3) was identified during a routine outpatient follow-up transfontanelle ultrasound three weeks

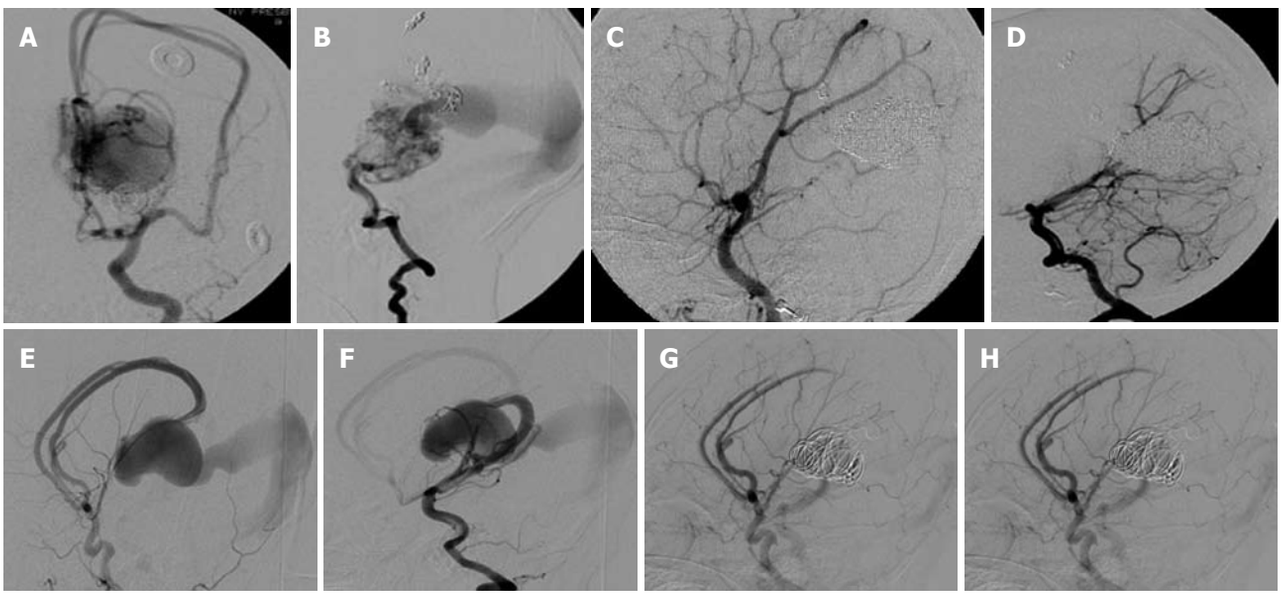

Figure 2 Catheter cerebral arteriography and embolization of Galen aneurysmal malformations. A, B: Arteriovenous shunting through a fine arterial network is seen within choroidal-type Galen aneurysmal malformations (VGAMs); C, D: Combined transarterial and transvenous embolization in this patient (Patient 1) enabled complete obliteration of the lesion; E, F: Direct fistulas to the venous pouch with feeders from the anterior (E) and posterior (F) cerebral arteries are seen in mural-type VGAMs (E and F); G, H: Palliative partial embolization in this patient (Patient 3) enabled resolution of congestive heart failure.

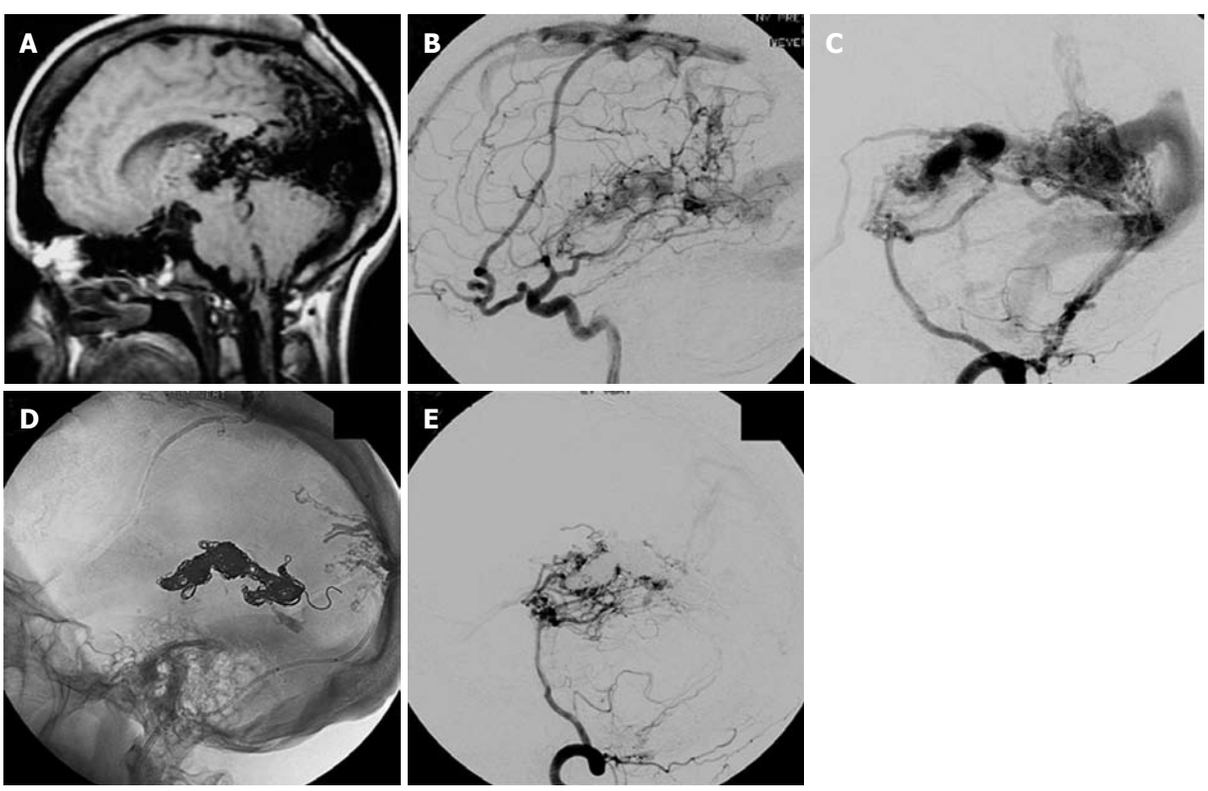

Figure 3 Galen aneurysmal malformations-associated cerebral vascular changes. A: Sagittal T1-weighted magnetic resonance imaging in this adult (Patient 5) with a VGAM shows extensive flow voids within the quadrigeminal cistern and in the medial parietal and occipital lobes; B, C: Catheter cerebral arteriography with internal carotid (B) and vertebral artery (C) injections show that multiple independent arteriovenous fistulas of the sagittal sinus, falx, and tentorium are present; D, E: Post-embolization lateral scout (D) and left vertebral artery angiogram (E) show the coil mass within the venous pouch and near complete obliteration of the lesion.

after completion of embolization. No long-term clinical sequelae were seen in either patient. Patient 5 initially presented with residual neurological deficits secondary to a remote stroke and ICH which occurred after an embolization in the 1970s using non-selective arterial injection of silastic beads (Figure 3).

Follow-up ranged from 2 to 97.2 (median 62.6) mo. At the time of last follow-up, all patients were neurologi-

Table 3 Treatment outcomes

Patient	Follow-up[1]	Clinical status	Bicêtre outcome score	Barthel index score	NRS-R executive/cognitive item difficulties
1	97.2	CHF resolved, neurologically intact	5	100	None
2	62.6	Neurologically intact	5	100	None
3	30.9	CHF resolved, neurologically intact, meeting all developmental milestones	5	NA	NA
4	2	Neurologically intact, facial pain relief	5	100	None
5	74.8	Neurological deficits including: abducens nerve palsy, left sided hemiparesis (ambulates independently with leg brace), and decreased visual acuity	2	95	Mild disorientation, memory, self-appraisal, planning, and decreased initiative/motivation

[1]Months post Galen aneurysmal malformations embolization. NRS-R: Neurobehavioral Rating Scale-Revised; CHF: Congestive heart failure; NA: Not avaliable.

cally intact with no functional or cognitive deficits or were unchanged (Table 3). Patient 5 remained stable after completion of staged embolizations but had mild persistent functional and cognitive deficits. As previously stated, the two patients with periprocedural complications had no appreciable long-term cognitive or functional impairments.

DISCUSSION

In several large series, serious long-term morbidity or death was the outcome after endovascular therapy in a significant number of VGAM patients[7-11,20-22]. The use of transvenous occlusion methodologies have been implicated in at least a subset of these poor outcomes[8,19]. However, the long-term cognitive effects of transvenous VGAM endovascular obliteration are unknown. Prior reports either do not address this issue directly or include patients who were treated a decade or more ago, and thus do not reflect outcomes seen with the use of modern equipment and techniques. Our group routinely utilizes transvenous embolization as part of a broader strategy to effect maximal VGAM occlusion. Therefore, we reviewed our contemporary experience in the endovascular treatment of VGAMs and specifically delineate the cognitive and functional outcomes observed using standardized assessment measures.

Based on results from a developmental questionnaire, Fullerton *et al*[7] specifically reported the neurodevelopmental outcomes of patients with VGAMs and found that 39% of surviving patients had significant developmental delay. Various groups have utilized other measures including Bicêtre outcome scores and found similar rates of developmental delay or retardation in the VGAM population[8,10]. While we present a smaller cohort of patients, our results indicate that very good cognitive and functional outcomes can be obtained after endovascular treatment of VGAMs with low attendant complication rates. All patients reviewed for this study had excellent clinical, cognitive, and functional outcomes during near- and long-term follow-up. Cognitive impairment secondary to therapeutic embolization was not observed. However, two minor intracranial hemorrhages and one small ischemic stroke occurred in the study group. These complications were not associated with residual cognitive or functional deficits. Prior observations that hemorrhage is not incompatible with a good outcome in VGAM patients are supported by this study[23]. Importantly, within the cohort of patients treated during this study, no deaths or serious morbidity were seen.

No strict protocols were employed in the management of the VGAM patients presented. For each patient, a multi-disciplinary approach was taken with the help of neonatologists, neurointensivists, adult and pediatric cardiologists, neurologists, pediatricians, neurointerventionalists, and neurosurgeons. Treatment decisions were based on age, presenting symptoms, and clinical status. While not ideal, embolization during the early postnatal period may be warranted to reduce arteriovenous shunting and improve cardiac status. Early intervention may also reduce the risk of brain parenchymal loss which is associated with permanent neurological deficits[24]. Conversely, it has been argued that severe CHF and low neonatal scores may warrant withholding treatment[21]. When a decision was made to proceed with treatment, the goals of therapy were individualized, tailored to the unique clinical scenario. For example, whereas in general multistage embolizations, a goal of complete or near complete VGAM occlusion is often desired, subtotal obliteration may be a sufficient temporizing measure as was the case in Patient 3.

A technical strategy employing combined transarterial and transvenous embolization routes was used for all patients in this series. This is in contrast to alternative strategies which include: (1) purely transvenous embolization; (2) maximal transarterial embolization followed by transvenous occlusion in select cases; or (3) purely transarterial embolization with strict avoidance of transvenous occlusion[8,9,11,25-27]. Reasons often cited for avoidance of transvenous embolization include venous infarction, distal migration of embolic material, and normal perfusion pressure breakthrough syndrome resulting in malignant cerebral edema or hemorrhage. In our experience, the simultaneous use of both transarterial and transvenous embolization facilitated VGAM occlusion without the introduction of technical difficulty or additional serious complications. Indeed, the use of a transvenous route is sometimes necessary as the VGAM may have arterial

feeders that are either inaccessible to microcatheterization, supply eloquent brain en route to the fistula, or are simply too numerous to embolize individually. Transvenous embolization may also be warranted if there is persistent retrograde venous drainage indicative of ongoing venous hypertension, which can be the inciting cause of hydrocephalus, macrocephaly, ischemic brain injury, and hemorrhage[8,26-28].

Treatment staging is also an important strategy to consider in the management of VGAM patients. While some practitioners try to avoid multiple embolization procedures[11], we believe that the excellent cognitive outcomes seen in our patients are, in part, the result of appropriate treatment staging. The staging of embolization allows for gradual lesion occlusion and thrombosis which promotes the development of alternative physiologic, non-fistulous drainage pathways[25]. Additionally, prolonged single-session radiation and iodinated contrast exposure are avoided by use of this strategy.

Vein of Galen aneurysmal malformations can be safely and effectively treated by current endovascular techniques with low attendant risks of morbidity or mortality. Patients treated with a strategy of staged transarterial and transvenous embolizations can have excellent long-term cognitive and functional outcomes. A multidisciplinary approach with individualized therapeutic goals, tailored to the unique clinical scenario will ensure the best possible outcome for each patient.

COMMENTS

Background

Vein of Galen aneurysmal malformations (VGAMs) are arteriovenous fistulas that drain to a persistent embryonic vein, the median prosencephalic vein of Markowski. These lesions can present with high-output congestive heart failure, seizures, failure to thrive, hydrocephalus, and brain hemorrhage. The treatment of VGAM has historically been associated with significant morbidity and mortality. While current endovascular techniques enable better outcomes to be achieved, it has been suggested that long-term cognitive deficits may be seen after therapeutic embolization.

Research frontiers

The optimal endovascular strategy for treating VGAMs is unclear. Strategies including (1) purely transvenous embolization; (2) maximal transarterial embolization followed by transvenous occlusion in select cases; (3) purely transarterial embolization with strict avoidance of transvenous occlusion; and (4) combined transarterial and transvenous embolization have been advocated by various groups.

Innovations and breakthroughs

Despite advancements in the endovascular treatment of VGAMs, neurological development and cognitive function may be impaired in survivors. In this experience the best outcomes are achieved when a multi-disciplinary approach is taken with the help of neonatologists, neurointensivists, adult and pediatric cardiologists, neurologists, pediatricians, neurointerventionalists, and neurosurgeons. In this report we show that patients treated with a strategy of staged transarterial and transvenous embolization can have excellent long-term cognitive and functional outcomes.

Applications

The findings show that VGAMs may be effectively treated using the endovascular strategy we outline. As there are currently a number of endovascular options for either palliating or curing VGAMs, this study shows that staged transarterial and transvenous embolization with a goal of complete obliteration is a viable strategy.

Peer review

It is an useful and innovative research which has been presented well.

REFERENCES

1 **Berenstein A**, Ortiz R, Niimi Y, Elijovich L, Fifi J, Madrid M, Ghatan S, Molofsky W. Endovascular management of arteriovenous malformations and other intracranial arteriovenous shunts in neonates, infants, and children. *Childs Nerv Syst* 2010; **26**: 1345-1358

2 **Raybaud CA**, Strother CM, Hald JK. Aneurysms of the vein of Galen: embryonic considerations and anatomical features relating to the pathogenesis of the malformation. *Neuroradiology* 1989; **31**: 109-128

3 **Amacher AL**, Shillito J. The syndromes and surgical treatment of aneurysms of the great vein of Galen. *J Neurosurg* 1973; **39**: 89-98

4 **Hoffman HJ**, Chuang S, Hendrick EB, Humphreys RP. Aneurysms of the vein of Galen. Experience at The Hospital for Sick Children, Toronto. *J Neurosurg* 1982; **57**: 316-322

5 **Johnston IH**, Whittle IR, Besser M, Morgan MK. Vein of Galen malformation: diagnosis and management. *Neurosurgery* 1987; **20**: 747-758

6 **Norman MG**, Becker LE. Cerebral damage in neonates resulting from arteriovenous malformation of the vein of Galen. *J Neurol Neurosurg Psychiatry* 1974; **37**: 252-258

7 **Fullerton HJ**, Aminoff AR, Ferriero DM, Gupta N, Dowd CF. Neurodevelopmental outcome after endovascular treatment of vein of Galen malformations. *Neurology* 2003; **61**: 1386-1390

8 **Lasjaunias PL**, Chng SM, Sachet M, Alvarez H, Rodesch G, Garcia-Monaco R. The management of vein of Galen aneurysmal malformations. *Neurosurgery* 2006; **59**: S184-S94; discussion S184-S94

9 **Lylyk P**, Viñuela F, Dion JE, Duckwiler G, Guglielmi G, Peacock W, Martin N. Therapeutic alternatives for vein of Galen vascular malformations. *J Neurosurg* 1993; **78**: 438-445

10 **McSweeney N**, Brew S, Bhate S, Cox T, Roebuck DJ, Ganesan V. Management and outcome of vein of Galen malformation. *Arch Dis Child* 2010; **95**: 903-909

11 **Lasjaunias P**, Garcia-Monaco R, Rodesch G, Ter Brugge K, Zerah M, Tardieu M, de Victor D. Vein of Galen malformation. Endovascular management of 43 cases. *Childs Nerv Syst* 1991; **7**: 360-367

12 **Li AH**, Armstrong D, terBrugge KG. Endovascular treatment of vein of Galen aneurysmal malformation: management strategy and 21-year experience in Toronto. *J Neurosurg Pediatr* 2011; **7**: 3-10

13 **Meila D**, Hannak R, Feldkamp A, Schlunz-Hendann M, Mangold A, Jacobs C, Papke K, Brassel F. Vein of Galen aneurysmal malformation: combined transvenous and transarterial method using a "kissing microcatheter technique". *Neuroradiology* 2012; **54**: 51-59

14 **Wong KN**, DeLuca J, Strax TE. Cognitive dysfunction following arteriovenous malformation of the vein of Galen: a case analysis. *Arch Phys Med Rehabil* 1996; **77**: 624-627

15 **McCauley SR**, Levin HS, Vanier M, Mazaux JM, Boake C, Goldfader PR, Rockers D, Butters M, Kareken DA, Lambert J, Clifton GL. The neurobehavioural rating scale-revised: sensitivity and validity in closed head injury assessment. *J Neurol Neurosurg Psychiatry* 2001; **71**: 643-651

16 **Vanier M**, Mazaux JM, Lambert J, Dassa C, Levin HS. Assessment of neuropsychologic impairments after head injury: interrater reliability and factorial and criterion validity of the Neurobehavioral Rating Scale-Revised. *Arch Phys Med Rehabil* 2000; **81**: 796-806

17 **Mahoney Fi**, Barthel Dw. Functional evaluation: the barthel index. *Md State Med J* 1965; **14**: 61-65

18 **Lasjaunias P**, Rodesch G, Terbrugge K, Pruvost P, Devictor D, Comoy J, Landrieu P. Vein of Galen aneurysmal malformations. Report of 36 cases managed between 1982 and 1988. *Acta Neurochir* (Wien) 1989; **99**: 26-37

19 **Lasjaunias PL**, Berenstein A, Brugge KGt. Surgical neuroangiography. 2nd ed. Vol 3. Berlin, New York: Springer, 2001:

105-226
20 **Heuer GG**, Gabel B, Beslow LA, Stiefel MF, Schwartz ES, Storm PB, Ichord RN, Hurst RW. **Diagnosis and treatment** of vein of Galen aneurysmal malformations. *Childs Nerv Syst* 2010; **26**: 879-887
21 **Geibprasert S**, Krings T, Armstrong D, Terbrugge KG, Raybaud CA. Predicting factors for the follow-up outcome and management decisions in vein of Galen aneurysmal malformations. *Childs Nerv Syst* 2010; **26**: 35-46
22 **Khullar D**, Andeejani AM, Bulsara KR. Evolution of treatment options for vein of Galen malformations. *J Neurosurg Pediatr* 2010; **6**: 444-451
23 **Meyers PM**, Halbach VV, Phatouros CP, Dowd CF, Malek AM, Lempert TE, Lefler JE, Higashida RT. Hemorrhagic complications in vein of Galen malformations. *Ann Neurol* 2000; **47**: 748-755
24 **Grossman RI**, Bruce DA, Zimmerman RA, Goldberg HI, Bilaniuk LT. Vascular steal associated with vein of Galen aneurysm. *Neuroradiology* 1984; **26**: 381-386
25 **Pearl M**, Gomez J, Gregg L, Gailloud P. Endovascular management of vein of Galen aneurysmal malformations. Influence of the normal venous drainage on the choice of a treatment strategy. *Childs Nerv Syst* 2010; **26**: 1367-1379
26 **Casasco A**, Lylyk P, Hodes JE, Kohan G, Aymard A, Merland JJ. Percutaneous transvenous catheterization and embolization of vein of galen aneurysms. *Neurosurgery* 1991; **28**: 260-266
27 **Dowd CF**, Halbach VV, Barnwell SL, Higashida RT, Edwards MS, Hieshima GB. Transfemoral venous embolization of vein of Galen malformations. *AJNR Am J Neuroradiol* 1990; **11**: 643-648
28 **Halbach VV**, Dowd CF, Higashida RT, Balousek PA, Ciricillo SF, Edwards MS. Endovascular treatment of mural-type vein of Galen malformations. *J Neurosurg* 1998; **89**: 74-80

S- Editor Cheng JX **L- Editor** Webster JR **E- Editor** Xiong L

World Journal of Radiology

Online Submissions: http://www.wjgnet.com/1949-8470office
wjr@wjgnet.com
doi:10.4329/wjr.v4.i3.90

World J Radiol 2012 March 28; 4(3): 90-96
ISSN 1949-8470 (online)

ORIGINAL ARTICLE

Assessment of gray matter heterotopia by magnetic resonance imaging

Ragab H Donkol, Khaled M Moghazy, Alaeddin Abolenin

Ragab H Donkol, Department of Radiology, Faculty of Medicine, Cairo University and Assir Central Hospital, Abha 61321, Saudi Arabia
Khaled M Moghazy, Departments of Radiology, Alexandria University and King Faisal University, Al Kobar 31952, Saudi Arabia
Alaeddin Abolenin, Neurology Department, King Faisal University, Al Kobar 31952, Saudi Arabia
Author contributions: Donkol RH designed the study, analyzed of data and wrote the manuscript; Moghazy K shared in manuscript writing and collection of data as well as interpreting MRI; Abolenin A contributed in selection and clinical assessment of patients as well as performing the electrophysiological analysis.
Correspondence to: Ragab H Donkol, MD, Department of Radiology, Faculty of Medicine, Cairo University and Assir Central Hospital, PO Box 34, Abha 61321,
Saudi Arabia. ragabhani@hotmail.com
Telephone:+966-7-2291169 Fax: +966-3-8552244
Received: September 25, 2011 Revised: December 23, 2011
Accepted: January 1, 2012
Published online: March 28, 2012

Abstract

AIM: To evaluate magnetic resonance imaging (MRI) features of different types of gray matter heterotopia.

METHODS: Between June 2005 and December 2009, the medical records and MRI studies of patients with gray matter heterotopia were reviewed. The MRI morphologic findings of heterotopia were recorded along with the presence and type of associated cranial malformations. Available clinical and electrophysiological data were also recorded.

RESULTS: 20 patients were included in the study. Their ages ranged from 9 mo to 39 years with a mean age of 15 years. All patients suffered from epileptic seizures. According to the location of heterotopia, patients were classified into three groups: subependymal (12), subcortical (5) and band (3) heterotopia.

CONCLUSION: MRI was useful in diagnosing and differentiating between various types of gray matter heterotopia. The severity of clinical manifestations of heterotopia was related to the location and pattern of heterotopia. Determination of heterotopia type and its extent is useful for management planning and predicting prognosis.

Key words: Epilepsy; Gray matter heterotopias; Magnetic resonance imaging; Neuroradiology; Neuroscience

Peer reviewer: Tarik F Massoud, MB, BCh, BAO, LRCPI, LRCSI, MA, MD, PhD, FRCR, Department of Radiology, University of Cambridge, Addenbrooke's Hospital, Box 219, Hills Road, Cambridge CB2 2QQ, United Kingdom

Donkol RH, Moghazy KM, Abolenin A. Assessment of gray matter heterotopia by magnetic resonance imaging. *World J Radiol* 2012; 4(3): 90-96 Available from: URL: http://www.wjgnet.com/1949-8470/full/v4/i3/90.htm DOI: http://dx.doi.org/10.4329/wjr.v4.i3.90

INTRODUCTION

Gray matter heterotopia is a relatively common form of neuronal migration disorder in which collections of cortical neurons are found in an abnormal location. It results from an in utero arrest of radial migration of neurons from the germinal matrix in the wall of the lateral ventricle to the developing cerebral cortex between 6 and 16 weeks of gestation[1,2]. It is usually discovered during the evaluation of children or young adults with epilepsy, children with neurodevelopmental abnormalities, or as an incidental finding[3-5].

The pathogenic mechanisms of gray matter heterotopia are not fully understood, but they lead to distinct clinicoradiological syndromes. Pathological classification of heterotopia includes nodular, laminar, and leptomen-

ingeal, (double cortex or band heterotopia)[1,3,6]. This classification is not particularly useful from a clinical perspective[1].

Neuroradiologists, basing their ideas on magnetic resonance imaging (MRI) appearances, have classified heterotopia into subependymal, subcortical, and band heterotopia[3,7-9]. The three forms of heterotopia were classified on the basis of the location and configuration of the ectopic gray matter tissue. Subependymal heterotopia consists of small foci of gray matter that are located in a subependymal location in close proximity to the ventricular wall. Subcortical heterotopia occurs as masses of gray matter within the deep and subcortical white matter. Band heterotopia was described as a symmetrical thick band of gray matter with smooth inner and outer margins that lies between layers of white matter[10-13]. The purpose of this study is to evaluate MRI features of different types of gray matter heterotopia.

MATERIALS AND METHODS

A consecutive series of patients with gray matter heterotopia during the period from June 2005 and December 2009 were studied. Medical records and MRI studies of all patients were reviewed. MRI morphologic findings of heterotopia were recorded along with the presence and type of associated cranial malformations. Available clinical and electrophysiological data were also recorded. All patients presented with a history of seizures, their clinical histories were reviewed with specific attention to the following; type of seizures, age at seizure onset, response to antiepileptic medications, associated cognitive or motor deficits; antenatal and perinatal history, developmental milestones, school performance and family history. Full systemic and neurologic examinations were performed during the visits to the neurology clinic. Electroencephalography (EEG) was carried out for each patient using the international 10-20 system. Head computed tomography (CT) scans were available for 12 patients. Cranial MRI studies were performed using a 1.5-T scanner (Symphony, Siemens Medical Systems, Erlangen, Germany). The following series of images were acquired: a- Sagittal, and axial T1WI: TR: 500-600 ms, TE: 14-20 ms. b- Axial and coronal T2WI: TR: 2500-4000 ms, TE: 80-120 ms. c- Axial FLAIR (Fluid-attenuated inversion recovery): TR: 7000-9000 ms, TE: 90-140 ms, TI: 2500 ms. d- Axial and coronal inversion-recovery (IR): TR/TI/TE (7000/400/70 ms). Advanced gradient echo sequence providing high contrast between white and gray matter is used as Fast Low Angle Shot and was used in 10 cases and turbo IR images were performed for 8 patients. Intravenous Gadolinium-DTPA (0.1 mmol/kg) T1WI in three planes was obtained for 9 patients as a space occupying mass was suspected on plain MRI. In all series, the thickness/gap was 5/1 mm, the matrix was 256 × 256 and the field of view was 23 cm. According to Barkovich[1], we classified heterotopia into three groups; subependymal, subcortical and band heterotopia.

RESULTS

During the study period, we included 20 patients with an MRI diagnosis of gray matter heterotopia. The mean age (± SD) of these patients was 14.6 (± 2.17) years, with a range from 9 mo to 39 years. Fourteen patients were females and 6 were males. All patients had a history of epileptic seizures. Patients were classified into three groups (Tables 1-3).

Subependymal heterotopia

This group included 12 patients (8 females and 4 males), aged 8 to 39 years with a mean age (± SD) of 17.9 (± 2.66) years. Details of the clinical, EEG and MRI findings of these patients are shown in Table 1. Subependymal heterotopia (SEH) had the MRI appearance of round to ovoid subependymal nodules, located just beneath and abutted the ependymal lining of the lateral ventricles and protruding slightly into its lumen resulting in an irregular ventricular outline. The number and size of heterotopia varied widely, from small nodules to a thick layer of coalescent nodules of gray matter lining the lateral ventricles. The nodules were isointense to the cortical gray matter on all MRI sequences (Figure 1). Contrast-enhanced T1WI studies were obtained in 4 patients, and the nodules showed no enhancement. The nodules were bilateral in 8 patients and unilateral in 4 patients. The trigone and occipital horns of lateral ventricles were the commonest location of subependymal nodules followed by the body and frontal region of the lateral ventricle. Associated brain anomalies were detected in only two patients, one had ventricular dilation and the other had Dandy Walker cyst.

Subcortical heterotopia

This group included 5 patients (3 females and 2 males), aged from 1 year to 27 years with a mean age (± SD) of 11.8 (± 4.4) years. Details of the clinical, EEG and MRI findings of these patients with subcortical heterotopia (SCH) are shown in Table 2. SCH appeared on MRI as regions of gray matter signal intensity within the cerebral hemispheric white matter. Their sizes varied from a few centimeters to large focal lesions that appeared as a mass with distortion of the adjacent ventricle but no enhancement after contrast. Three patients were diagnosed as having purely nodular SCH as there was no definite contiguity of the heterotopia with the cerebral cortex (Figure 2). The affected area of the cerebral hemisphere was reduced in size compared with the normal contralateral hemisphere. One patient had curvilinear SCH (Figure 3) as the heterotopic tissue had the appearance of enfolded cortex and showed contiguity with the cortex. One patient had mixed regions of both nodular and curvilinear SCH (Figure 4) as the gray matter nodules were seen in deep portions within the cerebral hemispheric white matter and the curvilinear portions were seen in the superficial portion and showed contiguity with the cortex. Three patients had associated brain abnormalities; two patients

Table 1 Data of 12 patients with subependymal heterotopia

Patient/sex/age (yr)	Seizure type	Developmental milestones	Neurological examination	EEG findings	MRI characteristics of heterotopia
1/F/8	Simple partial motor	Normal	Normal	Focal spikes	Unilateral nodule affecting frontal horn of right lateral ventricle
2/F/15	Complex partial	Delayed speech	Mild spasticity	Focal spikes	Bilateral nodules affecting both trigones
3/F/22	Tonic-clonic	Delayed walking	Spasticity	General spike-wave	Bilateral nodules affecting body of both lateral ventricles
4/F/14	Mixed	Learning disability	Hyperactivity, spasticity	General slow wave	Bilateral nodules affecting body of right lateral ventricle
5/M/12	Complex partial	Delayed speech	Spasticity	Focal spikes	Unilateral coalescent nodules affecting frontal horn of left lateral ventricle
6/F/10	Simple partial motor	Normal	Normal	Focal spikes	Bilateral nodules affecting trigone and occipital horns
7/M/39	Complex partial	Delayed walking	Hyperactive stretch reflexes	Focal spikes	Bilateral nodules affecting trigone and occipital horns
8/F/26	Simple partial motor	Normal	Ataxia	Focal spikes	Unilateral nodules affecting trigone of right lateral ventricle, Dandy Walker cyst
9/F/18	Simple partial motor	Normal	Spasticity	Focal spikes	Unilateral nodules affecting body of left lateral ventricle
10/M/13	Tonic-clonic	Delayed speech	Normal	General slow wave	Bilateral nodules affecting body of both lateral ventricles
11/F/28	Clonic	Learning disability	Hyperactivity	Slow wave	Bilateral nodules affecting trigone and occipital horns and ventricular dilatation
12/M/10	Tonic-clonic	Normal	Normal	General spike-wave	Bilateral nodules affecting trigone and occipital horns

M: Male; F: Female; EEG: Electroencephalography; MRI: Magnetic resonance imaging.

Table 2 Data of 5 patients with subcortical heterotopia

Patient/sex/age (yr)	Seizure type	Developmental milestones	Neurological examination	EEG findings	MRI characteristics of heterotopia
1/M/27	Complex partial	Delayed motor	Left hemiparesis	Focal spikes, slow wave	Large, nodular mass at right fronto-parietal lobes, extends across midline and ACC
2/F/15	Mixed	Delayed walking	spasticity	Focal spikes, slow waves	Small, multiple nodular, right frontal and parietal lobes
3/F/9	General tonic-clonic	Delayed speech and motor	Right hemipariesis	Spike-wave	Small, multiple, nodular, left parietal and ACC
4/F/7	General tonic-clonic	Delayed speech and motor	Attention deficit, hyperactivity, bilateral spasticity	General spike-wave	Bilateral curvilinear
5/M/1	Mixed	Delayed walking	Hyperactive reflexes	General slow wave	Mixed nodular and curvilinear and distorted ventricles

M: Male; F: Female; EEG: Electroencephalography; MRI: Magnetic resonance imaging; ACC: Anterior corpus callosum.

Table 3 Data of 3 patients with band heterotopia

Patient/ sex/age	Seizure type	Developmental milestones	Neurological examination	EEG findings	MRI characteristics of heterotopia
1/F/13 yr	Mixed	Delayed speech, motor	Nystagmus, dysartheria, spasticity	Generalized spike-wave	Bilateral diffuse thick bands at fronto-parietal lobes and pachygyria
2/F/4 yr	Tonic-clonic, myoclonic	Delayed motor	Microcephaly, bilateral spasticity	Generalized slow waves, polyphasic waves	Bilateral diffuse thick bands at both occipital lobes and pachygyria
3/F/9 mo	Infantile spasms	Delayed speech, motor	Spasticity, hyperactive reflexes	hypsarrhythmia	Bilateral diffuse thick bands at both fronto-parietal lobes and lissencephaly

M: Male; F: Female; EEG: Electroencephalography; MRI: Magnetic resonance imaging.

had agenesis of the corpus callosum and the third had ventricular distortion.

Band heterotopia

This group included 3 patients, all were females; aged

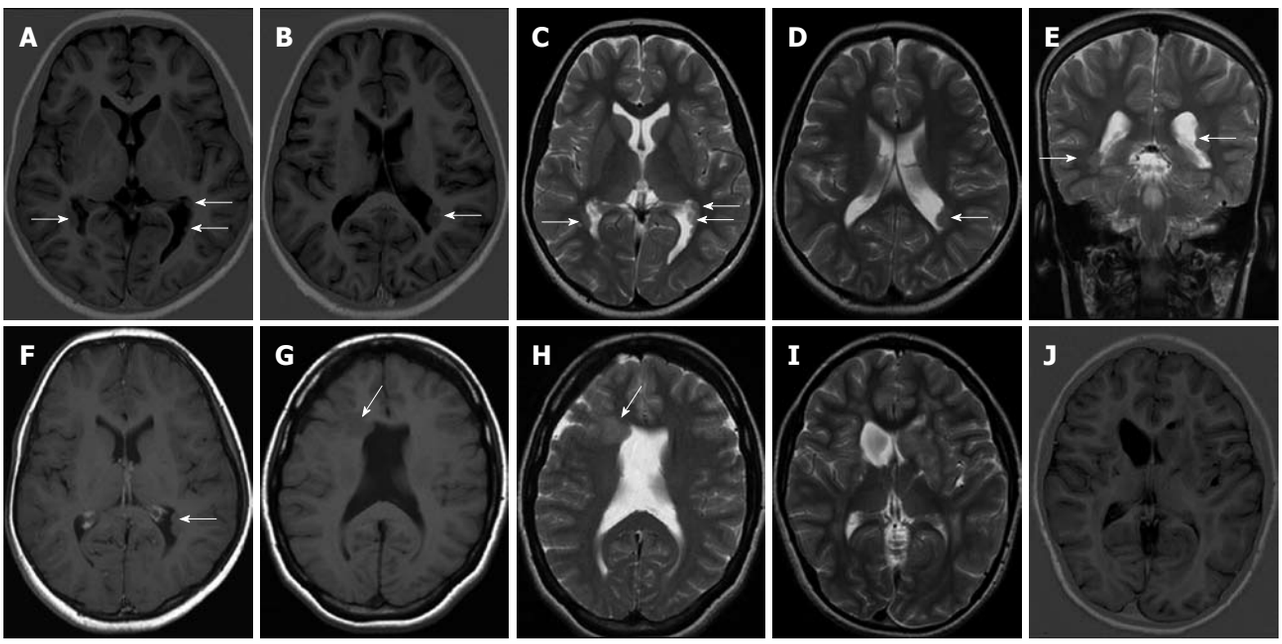

Figure 1 Subependymal heterotopia. A, B: Axial inversion-recovery magnetic resonance (MR) images; C-E: Axial (C, D) and coronal T2 W (E) images showing multiple bilateral subependymal gray matter heterotopic nodules protruding into and indenting the trigone of the lateral ventricles and the left occipital horn (arrows). The nodules are isointense to cortical gray matter; F: Axial contrast-enhanced T1WI shows no enhancement of the nodules; G, H: Axial T1W and T2W MR images revealing unilateral focal subependymal gray matter nodule (arrow) protruding into and indenting the frontal horn of the right lateral ventricle. The nodule is isointense to the cortical gray matter. Mild ventricular dilatation is noted with absent septum pelucidum; I, J: Axial T2 WI and inversion-recovery MR image showing a unilateral, large subependymal heterotopic gray matter mass projecting into the frontal horn of the left lateral ventricle. The mass is isointense to the cortical gray matter.

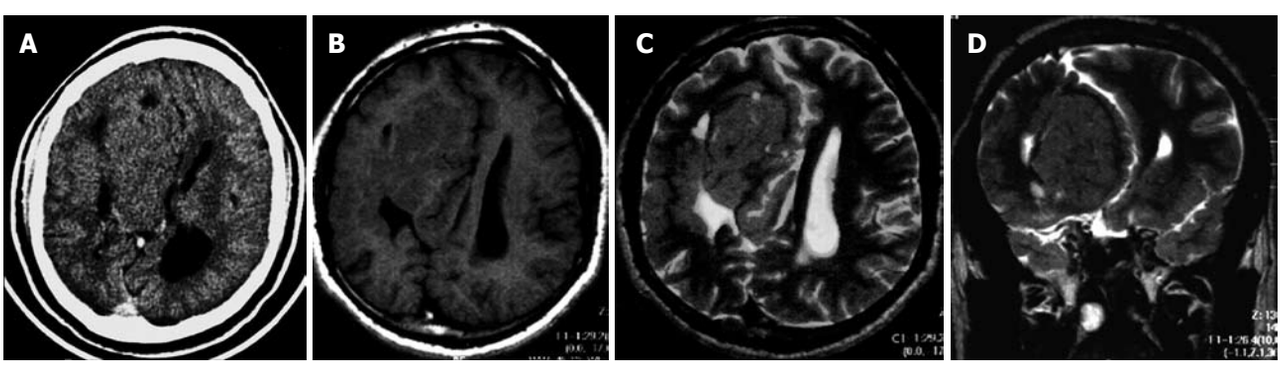

Figure 2 Subcortical nodular heterotopia. A: Contrast-enhanced axial computed tomography shows a large right fronto-parietal, non-enhancing mass exerting mass effect on the right lateral ventricle; B-D:Non-contrast enhanced magnetic resonance imaging (B), axial T1W, (C) axial T2W and (D) coronal T2W images showing a large subcortical nodular mass, isointense to the cortical gray matter. The overlying cortex is thin and the corpus callosum is agenetic.

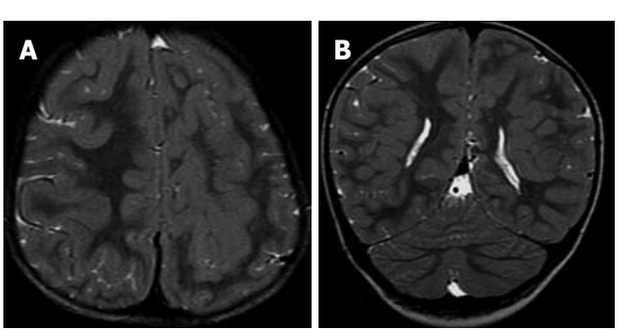

Figure 3 Subcortical curvilinear heterotopia. A, B: Axial T2W and coronal T2W images showing bilateral curvilinear heterotopia within the white matter. The heterotopic tissue is convoluted and contiguous with the overlying cortex. Linear and punctuate cerebrospinal fluid signal are seen within the heterotopic tissue. The cerebral cortex shows pachygyria.

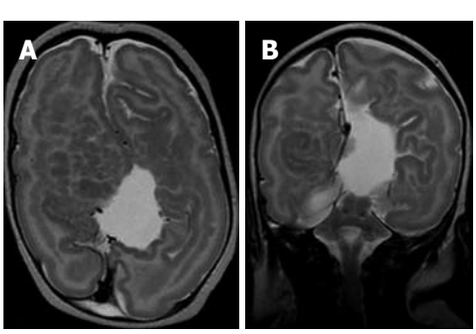

Figure 4 Mixed nodular and curvilinear subcortical heterotopia. A, B: Axial T2W and coronal T2W images showing multiple nodular and curvilinear heterotopia within the white matter bilaterally. The overlying cortex shows pachygyria. The right cerebral hemisphere is smaller compared to the left cerebral hemisphere. The corpus callosum is agenetic with distorted lateral ventricles.

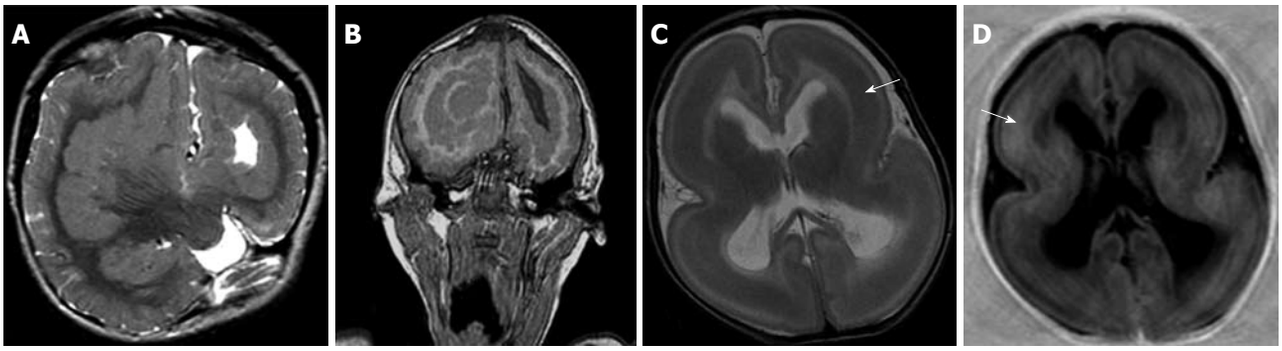

Figure 5 Band heterotopia. A, B: Axial T2W and coronal inversion-recovery images showing bilateral thick bands of heterotopia, isointense to cortical gray matter within the white matter. Note the pachygyria and small left cerebral hemisphere; C, D: Axial T2W and inversion-recovery images showing bilateral, symmetric, continuous, smooth, thick bands of gray matter (arrow) outlined by thin layers of white matter and seems like a "double cortex". Note the very thin, smooth cerebral cortex with absent cortical sulci (lissencephaly).

from 9 mo to 13 years with a mean age (± SD) of 5.9 (± 3.6) years. Details of the clinical, EEG and MRI findings of these patients with band heterotopia (BH) are shown in Table 3. Band heterotopia appeared as smooth, bilateral and symmetric ribbons of gray matter found in the central white matter between the cerebral cortex and the ventricular surface and separated from the cortex by normally myelinated white matter. BH was present in both cerebral hemispheres and had the same MRI signal intensity as the cortical gray matter on all MRI sequences (Figure 5). Two patients had associated pachygyria and one patient had lissencephaly. All patients in this group were developmentally delayed.

DISCUSSION

Malformations of cortical development are more common than was recognized in the era before MRI, as heterotopia on CT may be difficult to visualize[1,14]. Heterotopia is the most frequently occurring anomaly affecting cortical development. It is considered to be one of the most common congenital disorders in familial and early onset epilepsy[14-18]. MRI classification of gray matter heterotopia into subependymal, subcortical, and band types has been considered useful because patients in these three groups have different clinicoradiologic presentations and different underlying genetic disorders[3,5,19]. This classification of heterotopia may be useful in predicting patient outcome[2]. Several authors have reported that patients in all three heterotopia groups are very likely to develop epilepsy which is more commonly found in females than males[1,3,11,14]. In our study, all patients had a history of seizures and the female to male ratio was 14:6. In the current study, the three types of heterotopia were detected by MRI; SEH was the commonest type, followed by SCH, while BH was the least common type. On MRI; the heterotopic tissue was isointense with gray matter on all MR pulse sequences. The inversion recovery sequence was considered useful for the demonstration of heterotopic gray matter and the assessment of cortical thickness as it provides a strong contrast between gray and white matter. A similar frequency and MRI appearance has been reported in the literature[1-5].

SEH is characterized by periventricular nodules adjacent to the lateral ventricular walls just beneath and abutting the ependyma giving the nodular ventricular wall, and is not enhanced after intravenous contrast administration. This allows these nodules to be distinguished from the subependymal nodules of tuberous sclerosis that do not follow gray matter signal, and enhance after contrast administration[1,2,10-13]. SEH may be isolated or may develop in conjunction with other central nervous system malformations. It can be subdivided genetically into X-linked and non-X-linked inheritance patterns. They can be subdivided anatomically into unilateral focal, bilateral focal and bilateral diffuse groups. Some patients with SEH are neurologically and developmentally normal[1,12,20].

In this series, patients with SEH had a relatively late onset of seizures of different types. Simple partial seizure was the commonest type reported. Five patients had normal development and the remaining patients had mild developmental delay. The most common EEG abnormality was focal spikes. These findings are in agreement with other studies[1,2,8,10,11,15].

The present study, like many others, has demonstrated that MRI is excellent in the detection and characterization of SEH nodules[1,2,11,21-23]. The nodules are most likely to be bilateral and commonly at the trigone and occipital horns of lateral ventricles. It was reported that SEH caused little or no distortion of the remaining brain, whereas focal SCH caused marked distortion of the ventricles and diminished hemisphere size. In addition, surrounding white matter is normal in SEH, whereas most of the hemispheres containing SCH had qualitatively diminished white matter[1,3]. In our study, only 18% of patients with SEH had associated brain anomalies. Mithchell *et al*[12] reported that SEH was occasionally accompanied by mild ventricular dilation.

In the present study, MRI showed SCH in five patients. Three patients had purely nodular SCH, one patient had curvilinear SCH and another patient had mixed nodular and curvilinear SCH. Barckovich *et al*[3] reported that SCH usually consists of swirling, heterogeneous, nodular or curvilinear masses of gray matter containing

blood vessels and cerebrospinal fluid (CSF). It is reported that SCH extends through the white matter, from the ventricular surface to the cerebral cortex. In the current study, the affected area of the hemisphere was reduced in size compared with the normal contralateral hemisphere in three patients. Three of the five patients with SCH had associated brain abnormalities. In the present study, as in other studies, patients with SCH had a higher prevalence of developmental delay and motor dysfunction compared to the SEH group and had variable motor and intellectual disturbances, depending on the size of the lesion and the effect on the underlying cortex[3,5]. There were no differences in clinical manifestations among the different types of SCH.

Band heterotopia or double cortex syndrome usually occurs in females and very rarely in males. MRI shows the characteristic appearance of BH as a smoothly marginated layer of gray matter coursing parallel to the lateral ventricle, separated from the overlying cortex and underlying ventricle by layers of white matter. Bands are neither convoluted nor contiguous with the overlying cortex. They do not contain blood vessels or CSF. The thicker the band of heterotopic neurons; the worse the disability and increased prevalence of developmental delay[1,4,9]. In the present study, MRI showed band heterotopia in three females. Two patients had associated pachygyria and one had lissencephaly. All patients in this group had severe developmental delay.

The assessment of neuronal heterotopias and their pathophysiological significance in epilepsy are still the subject of debate. Many reports either classify all neuronal migration disorders together, or lump them with other cortical dysgeneses. Also, the mechanisms by which heterotopic gray matter results in seizures are unclear and future respective strategies will have to take into account the multiplicity of heterotopic lesions, their localization, and their effects on overlying cortical functional organization. In our study, the clinical, EEG, psychometric, and neuroimaging features of 20 patients with gray matter heterotopia are described and compared with other studies with the aim of reducing debate and emphasizing the role of conventional and advanced MRI sequences in differentiating between various types of gray matter heterotopia. The severity of the clinical manifestations of heterotopia is related to the location and pattern of heterotopia. Determination of the heterotopia type and its extent is useful for management planning and predicting prognosis.

COMMENTS

Background

Gray matter heterotopia is a relatively common form of neuronal migration disorders. The pathogenic mechanisms are not fully understood, but they lead to distinct clinicoradiological syndromes. Neuroradiologists, basing their ideas on magnetic resonance imaging (MRI) appearances, have classified heterotopia into subependymal, subcortical and band heterotopia.

Research frontiers

The assessment of neuronal heterotopias and their pathophysiological significance in epilepsy are still the subject of debate. The mechanisms by which heterotopic gray matter results in seizures are unclear. In this study, the clinical, electroencephalography, psychometric and neuroimaging features of 20 patients with gray matter heterotopia are described and compared with other studies with the aim of reducing debate and emphasizing the role of conventional and advanced MRI sequences in differentiating between various types of gray matter heterotopia.

Innovations and breakthroughs

This recent study highlighted the usefulness of MRI in differentiating between shape, location and extent of various types of gray matter heterotopia. The authors emphasized that the severity of the clinical manifestations of heterotopia is related to the location and pattern of heterotopia.

Applications

Determination of the type, extent and location of gray matter heterotopia are useful for management planning and predicting prognosis.

Terminology

Gray matter heterotopia is a neuronal migration disorder in which collections of cortical neurons are found in an abnormal location. Subependymal heterotopia consists of small foci of gray matter that are located in a subependymal location near the ventricular wall. Subcortical heterotopia occurs as masses of gray matter within the deep and subcortical white matter. Band heterotopia is a symmetrical thick band of gray matter that lies between layers of the white matter.

Peer review

This is a well-written account of MRI of brain heterotopia.

REFERENCES

1 **Barkovich AJ**, Kuzniecky RI. Gray matter heterotopia. *Neurology* 2000; **55**: 1603-1608
2 **Barkovich AJ**, Kjos BO. Gray matter heterotopias: MR characteristics and correlation with developmental and neurologic manifestations. *Radiology* 1992; **182**: 493-499
3 **Barkovich AJ**. Morphologic characteristics of subcortical heterotopia: MR imaging study. *AJNR Am J Neuroradiol* 2000; **21**: 290-295
4 **D'Agostino MD**, Bernasconi A, Das S, Bastos A, Valerio RM, Palmini A, Costa da Costa J, Scheffer IE, Berkovic S, Guerrini R, Dravet C, Ono J, Gigli G, Federico A, Booth F, Bernardi B, Volpi L, Tassinari CA, Guggenheim MA, Ledbetter DH, Gleeson JG, Lopes-Cendes I, Vossler DG, Malaspina E, Franzoni E, Sartori RJ, Mitchell MH, Mercho S, Dubeau F, Andermann F, Dobyns WB, Andermann E. Subcortical band heterotopia (SBH) in males: clinical, imaging and genetic findings in comparison with females. *Brain* 2002; **125**: 2507-2522
5 **Barkovich AJ**. Subcortical heterotopia: a distinct clinicoradiologic entity. *AJNR Am J Neuroradiol* 1996; **17**: 1315-1322
6 **Barkovich AJ**, Kuzniecky RI, Dobyns WB, Jackson GD, Becker LE, Evrard P. A classification scheme for malformations of cortical development. *Neuropediatrics* 1996; **27**: 59-63
7 **Barkovich AJ**, Kuzniecky RI, Jackson GD, Guerrini R, Dobyns WB. Classification system for malformations of cortical development: update 2001. *Neurology* 2001; **57**: 2168-2178
8 **Huttenlocher PR**, Taravath S, Mojtahedi S. Periventricular heterotopia and epilepsy. *Neurology* 1994; **44**: 51-55
9 **Ono J**, Mano T, Andermann E, Harada K, Sakurai K, Ikeda T, Yoshihara N, Shimizu K, Okada S, Andermann F. Band heterotopia or double cortex in a male: bridging structures suggest abnormality of the radial glial guide system. *Neurology* 1997; **48**: 1701-1703
10 **Dubeau F**, Tampieri D, Lee N, Andermann E, Carpenter S, Leblanc R, Olivier A, Radtke R, Villemure JG, Andermann F. Periventricular and subcortical nodular heterotopia. A study of 33 patients. *Brain* 1995; **118** (Pt 5): 1273-1287
11 **Aghakhani Y**, Kinay D, Gotman J, Soualmi L, Andermann F, Olivier A, Dubeau F. The role of periventricular nodular heterotopia in epileptogenesis. *Brain* 2005; **128**: 641-651
12 **Mitchell LA**, Simon EM, Filly RA, Barkovich AJ. Antenatal diagnosis of subependymal heterotopia. *AJNR Am J Neuroradiol* 2000; **21**: 296-300
13 **Guerrini R**, Dobyns WB. Bilateral periventricular nodular

heterotopia with mental retardation and frontonasal malformation. *Neurology* 1998; **51**: 499-503
14 **Barkovich AJ**, Kuzniecky RI, Jackson GD, Guerrini R, Dobyns WB. A developmental and genetic classification for malformations of cortical development. *Neurology* 2005; **65**: 1873-1887
15 **Lu J,** Sheen V**.** Periventricular heterotopia. *Epilepsy Behav* 2005; 7: 143-149
16 **Fauser S**, Schulze-Bonhage A, Honegger J, Carmona H, Huppertz HJ, Pantazis G, Rona S, Bast T, Strobl K, Steinhoff BJ, Korinthenberg R, Rating D, Volk B, Zentner J. Focal cortical dysplasias: surgical outcome in 67 patients in relation to histological subtypes and dual pathology. *Brain* 2004; **127**: 2406-2418
17 **Hannan AJ**, Servotte S, Katsnelson A, Sisodiya S, Blakemore C, Squier M, Molnár Z. Characterization of nodular neuronal heterotopia in children. *Brain* 1999; **122** (Pt 2): 219-238
18 **Smith AS**, Weinstein MA, Quencer RM, Muroff LR, Stonesifer KJ, Li FC, Wener L, Soloman MA, Cruse RP, Rosenberg LH. Association of heterotopic gray matter with seizures: MR imaging. Work in progress. *Radiology* 1988; **168**: 195-198
19 **Mai R**, Tassi L, Cossu M, Francione S, Lo Russo G, Garbelli R, Ferrario A, Galli C, Taroni F, Citterio A, Spreafico R. A neuropathological, stereo-EEG, and MRI study of subcortical band heterotopia. *Neurology* 2003; **60**: 1834-1838
20 **Sisodiya SM**, Free SL, Thom M, Everitt AE, Fish DR, Shorvon SD. Evidence for nodular epileptogenicity and gender differences in periventricular nodular heterotopia. *Neurology* 1999; **52**: 336-341
21 **El-Serougy LG,** Azab AH, Saad M. Gray matter heterotopia: MRI diagnostic criteria correlated with clinical assessment. *Egypt J Radiol Nuc Med* 2002; **33:** 65-77
22 **Canal N**, Frattola L, Smirne S. The metabolism of cyclic-3'-5'-adenosine monophosphate (cAMP) in diseased muscle. *J Neurol* 1975; **208**: 259-265
23 **Chang BS**, Ly J, Appignani B, Bodell A, Apse KA, Ravenscroft RS, Sheen VL, Doherty MJ, Hackney DB, O'Connor M, Galaburda AM, Walsh CA. Reading impairment in the neuronal migration disorder of periventricular nodular heterotopia. *Neurology* 2005; **64**: 799-803

S- Editor Cheng JX **L- Editor** Webster JR **E- Editor** Xiong L

World Journal of Radiology

Online Submissions: http://www.wjgnet.com/1949-8470office
wjr@wjgnet.com
doi:10.4329/wjr.v4.i3.97

World J Radiol 2012 March 28; 4(3): 97-101
ISSN 1949-8470 (online)

BRIEF ARTICLE

Prediction of transitional lumbosacral anatomy on magnetic resonance imaging of the lumbar spine

Majid Chalian, Theodoros Soldatos, John A Carrino, Alan J Belzberg, Jay Khanna, Avneesh Chhabra

Majid Chalian, Theodoros Soldatos, John A Carrino, Avneesh Chhabra, Russell H. Morgan Department of Radiology and Radiological Science, The Johns Hopkins Hospital, Baltimore, MD 21287, United States
Alan J Belzberg, Department of Neurosurgery, The Johns Hopkins Hospital, Baltimore, MD 21287, United States
Jay Khanna, Department of Orthopaedic Surgery, The Johns Hopkins Hospital, Baltimore, MD 21287, United States
Author contributions: All authors contributed equally to the design and execution of the study, analysis of the data and writing of the paper.
Correspondence to: Avneesh Chhabra, MD, Russell H. Morgan Department of Radiology and Radiological Science, The Johns Hopkins Hospital, 601 North Caroline Street, Baltimore, MD 21287, United States. achhabr6@jhmi.edu
Telephone: +1-443-2876032 Fax: +1-443-2876438
Received: August 18, 2011 Revised: February 22, 2012
Accepted: March 1, 2012
Published online: March 28, 2012

Abstract

AIM: To evaluate two simple angle measurements for predicting lumbosacral transitional vertebra (LSTV) in magnetic resonance imaging (MRI) studies of the spine.

METHODS: The lumbar spine MRI studies of 50 subjects with LSTV and 50 subjects with normal lumbosacral anatomy were retrospectively evaluated. In each study, the mid-sagittal T2-weighted image was used to measure the angle formed by a line parallel to the superior surface of the sacrum and a line perpendicular to the axis of the scan table (A-angle), as well as the angle formed by a line parallel to the superior endplate of the L3 vertebra and a line parallel to the superior surface of the sacrum (B-angle).

RESULTS: The total study population consisted of 100 subjects (46 males, 54 females, 51 ± 16 years old). There were no differences in age and sex between the two groups. Both A-angle and B-angle were significantly increased in subjects with LSTV compared to controls ($P < 0.05$). The optimal cut-off values of A-angle and B-angle for the prediction of LSTV were 39.8° (sensitivity = 80%, specificity = 80%, accuracy = 83%; 95% confidence interval = 74%-89%, $P = 0.0001$) and 35.9° (sensitivity = 80%, specificity = 54%, accuracy = 69%; 95% confidence interval = 59%-78%, $P = 0.0005$), respectively.

CONCLUSION: On sagittal MR images of the lumbar spine, an increased A-angle and/or B-angle should alert the radiologist to the presence of LSTV.

Key words: Lumbosacral transitional vertebra; Magnetic resonance imaging; Lumbar spine; Angle; Prediction

Peer reviewers: Shigeru Ehara, MD, Professor, Chair, Iwate Medical University School of Medicine, Morioka 020-8505, Japan; Tommaso Bartalena, MD, PhD, Radiology, S. Orsola University Hospital, Via Massarenti 9, 40138 Bologna, Italy

Chalian M, Soldatos T, Carrino JA, Belzberg AJ, Khanna J, Chhabra A. Prediction of transitional lumbosacral anatomy on magnetic resonance imaging of the lumbar spine. *World J Radiol* 2012; 4(3): 97-101 Available from: URL: http://www.wjgnet.com/1949-8470/full/v4/i3/97.htm DOI: http://dx.doi.org/10.4329/wjr.v4.i3.97

INTRODUCTION

Lumbosacral transitional vertebra (LSTV) is a developmental spinal anomaly, in which the lowest lumbar vertebra shows elongation of its transverse process and varying degrees of fusion/failure of segmentation from the sacrum[1]. LSTV has been reported to alter the biomechanics of the lumbar spine and contribute to low back pain[2-5]. However, controversy still exists regarding the actual clinical significance of this entity[6,7], which has an incidence of 4%-30% in the general population[8]. The

radiologic identification and reporting of LSTV may provide the clinician with a potential cause for the patient's symptoms and prevent erroneous numbering of the lumbar vertebrae, which may have serious implications in cases where spinal surgery is contemplated[7,8]. The anteroposterior radiograph of the lumbar spine remains the reference standard method to detect the above entity[9], but is not always available to the magnetic resonance imaging (MRI) reader. On MRI studies of the lumbar spine, LSTVs can be detected either on coronal images which highlight the transitional lumbosacral anatomy, or on axial images of the lumbosacral junction which depict the pseudoarthrosis or fusion of the last lumbar vertebra with the sacrum. However, coronal images are not usually acquired in MRI examinations of the lumbar spine, whereas the lumbosacral junction may be erroneously identified at the L4-L5 level in sagittal scout images of subjects with LSTV, resulting in incomplete axial coverage of the transitional level. As a result, LSTVs may be missed on MRI.

We hypothesized that transitional lumbosacral anatomy is associated with alterations of the lumbosacral curvature, the assessment of which could assist in detecting the entity on MRI. To validate this hypothesis, we applied two specific angle measurements in lumbar spine MRI studies of patients with and without LSTVs.

MATERIALS AND METHODS

Institutional review board approval was granted and informed consent was waived for this HIPAA-compliant retrospective study. The MRI database of our institution was searched for examinations of the lumbar spine performed in adults over a period of 6 mo (from January to June 2010). Two radiologists, who were blinded to the original reports of the MRI studies, consecutively evaluated examinations from newer to older on a picture archiving and communication system workstation (Ultravisual, Emageon, AL, United States), in order to enroll 50 subjects with LSTV (study group) and 50 subjects without LSTV (control group). In each examination, a vertebra was defined as LSTV when (1) on sagittal images, it was separated from the sacrum by disc material; and (2) on axial images, it exhibited uni- or bilateral pseudoarthrosis or fusion with the sacral ala[6,9-11]. Subjects with scoliosis, listhesis greater than grade 1, and/or history or MRI findings of spinal trauma, tumor, surgery or infection were excluded. After the selection of the study sample, a software-based goniometer tool was used on the mid-sagittal T2-weighted image of each MRI study in order to measure: (1) the angle formed by a line parallel to the superior surface of the sacrum and a line perpendicular to the axis of the scan table (A-angle); and (2) the angle formed by a line parallel to the superior endplate of the L3 vertebra and a line parallel to the superior surface of the sacrum (B-angle) (Figure 1).

The patient's age and sex, angle measurements of the respective MRI study and side(s) of pseudoarthrosis were registered for each case. In subjects with LSTV, the side(s) of the pseudoarthrosis/fusion was additionally recorded. Differences in age, A-angle and B-angle between the study and control groups were evaluated using Student's *t*-test for independent samples, and difference in sex using χ^2. Receiver operating characteristic (ROC) curves were computed to determine the optimal cut-off values of A-angle and B-angle for the prediction of transitional lumbosacral anatomy. A probability level of 0.05 was considered statistically significant. All data were stored on a spreadsheet (Excel 2010, Microsoft, Seattle, WA, United States), and analyses were performed using a commercially available statistical package (MedCalc 8.0, MedCalc Software, Mariakerke, Belgium).

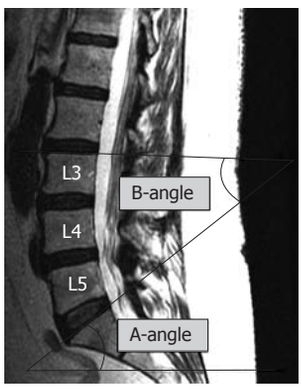

Figure 1 Mid-sagittal T2-weighted fast spin-echo image of the lumbar spine illustrates the angle measurements which were performed in the study. A-angle was defined by a line parallel to the superior surface of the sacrum and a line perpendicular to the axis of the scan table. B-angle was defined by a line parallel to the superior endplate of L3 vertebra and a line parallel to the superior surface of the sacrum.

Table 1 Demographics of the study and control groups, along with the angle measurements of the respective magnetic resonance imaging examinations

Feature	Study group	Control group	*P* value
Age (yr)	53 ± 17	48 ± 14	0.1465
Sex (males/females)	22/28	24/26	0.4205
A-angle (degrees)	46.3 ± 7.8	35.9 ± 7.7	< 0.0001
B-angle (degrees)	46.7 ± 8.4	41.6 ± 10.0	0.0035

RESULTS

The total study population consisted of 100 subjects (46 males, 54 females, 51 ± 16 years old). Table 1 summarizes the demographics of the two groups, along with the angle measurements of the respective MRI examinations. A graphic representation of the results obtained during angle measurements in subjects of the study and control groups is demonstrated in Figure 2. There were no differences in age and sex between the two groups. Both A-angle and B-angle were significantly increased in subjects with LSTV as compared to controls ($P < 0.05$, Figure 3). In the study group, the pseudoarthrosis/fusion was located on the left side in 19 (38%) cases, on the right side in 6 cases (12%) cases, and bilaterally in 25 (50%)

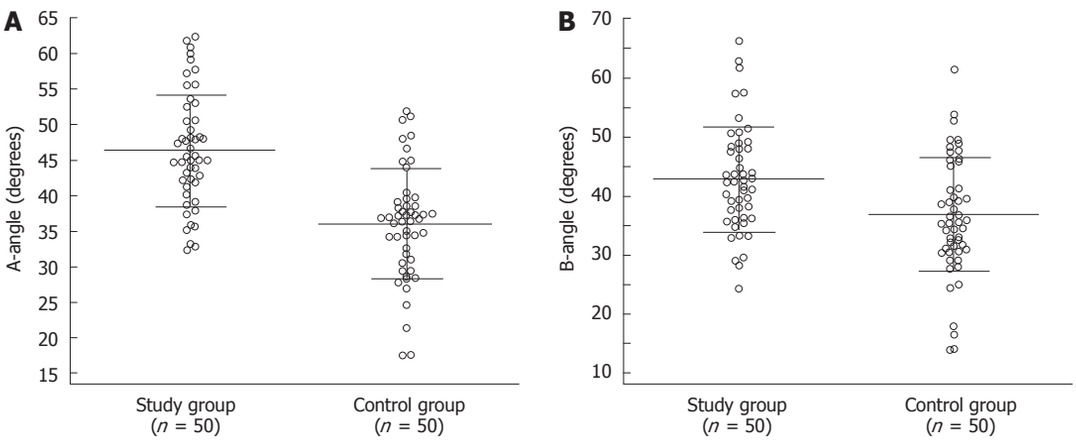

Figure 2 Graphic demonstration of the results obtained during measurements of the A-angle (A) and B-angle (B) in the two groups of the study. On each column, a set of horizontal lines represents the average value (long line) ± SD (short lines).

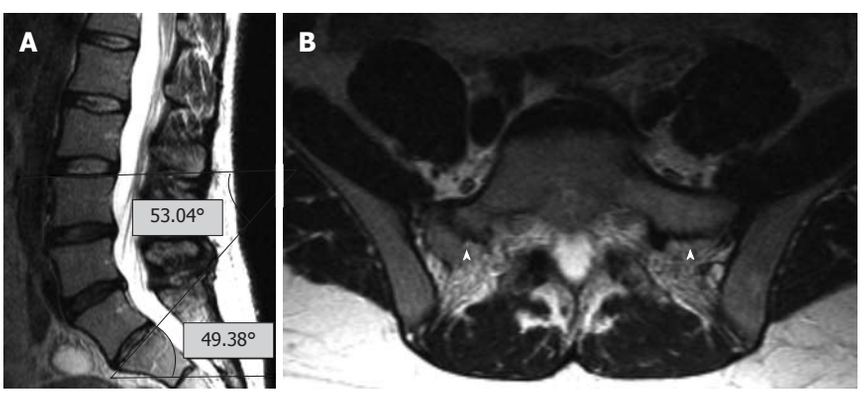

Figure 3 T2-weighted images of the lumbar spine. A: The mid-sagittal T2-weighted image of the lumbar spine exhibits increased A-angle (49.38°) and B-angle (53.04°); B: Corresponding axial fast spin-echo image in this 42-year-old female subject with transitional lumbosacral anatomy demonstrates bilateral pseudoarthrosis of the transitional vertebra with the sacral ala (arrowheads).

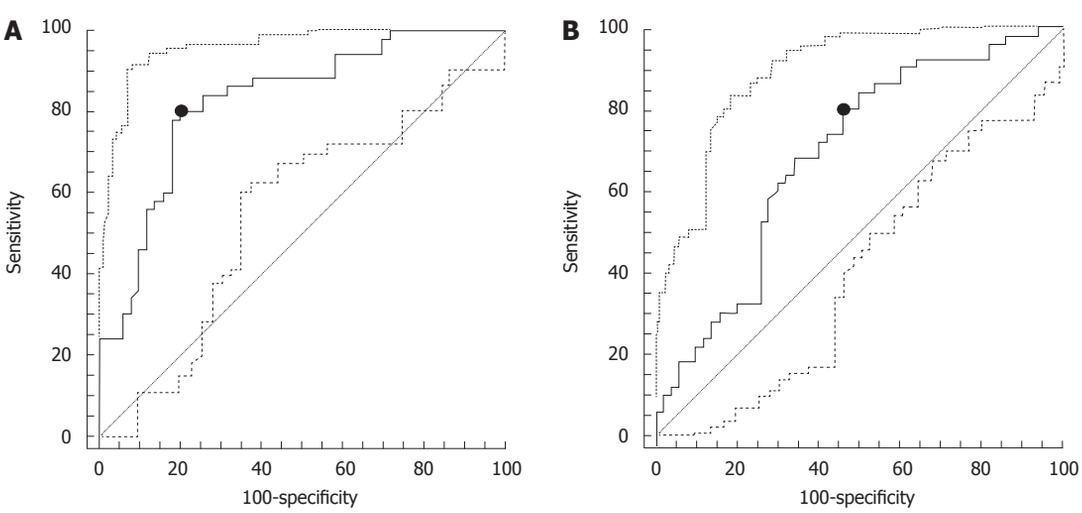

Figure 4 Receiver operating characteristic curves showing the predictive value of A-angle (A) and B-angle (B) for the presence of transitional lumbosacral vertebra.

cases. Based on the ROC curves, the optimal cut-off values of A-angle and B-angle for the prediction of LSTV were 39.8° (sensitivity = 80%, specificity = 80%, area under the ROC curve = 0.825; 95% confidence interval = 0.737-0.894, $P = 0.0001$), and 35.9° degrees (sensitivity = 80%, specificity = 54%, area under the ROC curve = 0.687; 95% confidence interval = 0.586-0.776, $P = 0.0005$), respectively (Figure 4).

DISCUSSION

Since the first reported association between LSTVs and low back pain by Bertolotti *et al*[12] in 1917, there has been considerable debate and controversy among authors regarding the clinical relevance of the above entity. It has been suggested that articulation between a LSTV and the sacrum protects the intervening intervertebral disc by limiting motion across the pseudoarthrosis and transmitting stress to superior lumbar segments, thereby resulting in its early degeneration. In subjects with LSTV, low back pain can originate from the pseudoarthrosis, resultant instability and degeneration of the level cephalad to the LSTV, compression of the nerve root from hypertrophied transverse process, and the contralateral facet joint, when the articulation is unilateral[8]. Clinicians who consider LSTV as a cause of low back pain and physicians who are involved with interventional procedures on the lumbar spine would benefit from MRI reports which describe the presence of this anatomical variation and provide accurate numbering of the lumbar vertebrae. MRI of the lumbar spine lacks the panoramic perspective of radiography and the spatial resolution of computed tomography, and unless the radiologist actively interrogates for this entity, the detection of LSTV may be missed.

In our experience, subjects with LSTV frequently demonstrate exaggerated lumbar lordotic curvature and lack of sharp angulations at the lumbosacral junction on the mid-sagittal MR image. Hence, we employed two simple angle measurements, the A-angle and the B-angle, which quantify the lumbosacral angulation and sacral inclination on sagittal MRI images, respectively. The A-angle is identical in measurement to the lumbosacral angle measured on lateral radiographs of the spine, increased values of which have been previously reported to be associated with low back pain[13]. The B-angle was defined by the superior sacral surface and the superior endplate of L3 vertebra, as we have observed that, in most cases, the main curvature of the lumbar spine extends along the above levels.

In agreement with our observations, both angles were significantly increased in subjects with LSTV as compared to controls (Figure 2). The two angles exhibited similar levels of sensitivity; however, the A-angle demonstrated higher specificity. Since most radiologists start the evaluation of lumbar spine MRIs from the sagittal images, it is suggested that a measurement of the A-angle or B-angle or at least a gross assessment of the sacral inclination and lumbar lordosis should be performed before proceeding to the detailed study assessment. An A-angle of greater than 40°, a B-angle of greater than 36°, a large inclination of the sacrum grossly with respect to axis of the scan table, or an exaggerated lumbar lordosis should alert the radiologist for the possible presence of an LSTV. Compared to the A-angle, the B-angle may be more difficult to measure (e.g., the forming lines may intersect out of the image) and is also harder to assess grossly by visual inspection. Of course, exaggerated lumbar lordosis may also result from significant degenerative disc disease, age or larger degrees of listhesis. The results of this study suggest that this finding should be carefully scrutinized in young subjects to avoid missing an LSTV.

Previous studies have reported several predictive similar signs which can suggest the presence of LSTV in lumbar spine MRIs. O'Driscoll *et al*[11] described two types of intervertebral discs, which present at the lumbosacral junction in subjects with LSTV. The "type I" disc is smaller than the superior one, maintains its high T2 signal intensity, has no intranuclear cleft, and extends along the entire anteroposterior space without any fusion between the adjacent endplates, and has been considered indicative of an LSTV. However, the specificity of the above findings is questionable, as in cases of pseudoarthrosis the transitional disc may appear normal. A "type Ⅱ" disc is a rudimentary disc which is smaller than the transitional one, maintains its signal intensity, has no intranuclear cleft, and is associated with fusion of the anterior endplates, both of which appear concave[11]. Again, these signs are non-specific since a residual disc may exist at the S1-S2 level in up to 58% of cases, leading to overdiagnosis of LSTV[1]. On axial images, the identification of the iliolumbar ligaments, arising from the L5 vertebra, enables precise detection of LSTV and accurate numbering of the lumbar vertebrae[9]; however, in cases with segmentation anomalies of the thoracolumbar spine, the recognition of L5 vertebra may be incorrect[8]. Another study demonstrated that LSTVs commonly assume a "squared" appearance in lateral radiographs, with the ratio of the anteroposterior diameter of the superior endplate to the inferior endplate being less than 1.37[14].

By design, retrospective case-control studies are susceptible to selection bias; therefore a limitation of our study is that the studied material is not representative of the general population. Another limitation is the absence of correlation with radiographic findings, and the identification of the transitional anatomy being exclusively based on MRI. As a result, from the four classical types of LSTVs described by Castelvi *et al*[6], we were able to identify the LSTVs which exhibited pseudoarthrosis or fusion with the sacrum (types Ⅱ, Ⅲ and Ⅳ), but not those with dysplastic transverse processes, measuring at 19 mm in craniocaudal dimension (type Ⅰ). Therefore, we cannot exclude the possibility that one or more cases were erroneously included in the study or the control group. However, the intent of the study was to predict LSTV on MR imaging alone, as these simple measurements may help MRI readers in their routine practice when radiographs have not been performed, or are not available at the time of read out. Future prospective studies in larger populations may re-evaluate the predictive values of the angles we present in this paper.

COMMENTS

Background

Lumbosacral transitional vertebra (LSTV) has been reported to alter the biomechanics of the lumbar spine and has been postulated to be an important contributor to low back pain. On magnetic resonance imaging (MRI), the detection of LSTVs is not always straightforward, and an unknown number of cases are

missed. Sagittal MRI images constitute the initial search front for the readers to detect abnormalities of curvature and vertebral numbering. If the LSTV is not suspected on the sagittal image, it is easy to overlook the transitional vertebra on the axial image and lose the normal count. A simple means to detect LSTV on sagittal MRI studies of the lumbar spine may assist radiologists in providing more accurate reports.

Research frontiers

This paper describes two simple angle measurements used on sagittal MRI images of the lumbar spine to predict LSTV.

Innovations and breakthroughs

Previous authors have described angle measurements which can be used to predict LSTV on radiographs, but there have been no respective reports on MRI. This is a novel and important paper, which describes easy and accurate means of predicting LSTV on MRI studies of the lumbar spine.

Applications

The angle measurements described are helpful for detecting LSTV, particularly in cases where radiographs have not been performed, or are not available at the time of read out.

Terminology

LSTV is a developmental spinal anomaly, in which the lowest lumbar vertebra shows elongation of its transverse process and varying degrees of fusion/failure of segmentation from the sacrum.

Peer review

The authors present simple but useful research describing an easy and intuitive sign that may give a hint to the radiologist regarding the presence of a transitional lumbosacral vertebral body. The A-angle is quite easy to assess at gross visual inspection and may alert radiologists looking for other morphologic signs which should be regarded as the only real definite evidence of transitional vertebral anatomy.

REFERENCES

1 **Hughes RJ**, Saifuddin A. Imaging of lumbosacral transitional vertebrae. *Clin Radiol* 2004; **59**: 984-991

2 **Avimadje M**, Goupille P, Jeannou J, Gouthière C, Valat JP. Can an anomalous lumbo-sacral or lumbo-iliac articulation cause low back pain? A retrospective study of 12 cases. *Rev Rhum Engl Ed* 1999; **66**: 35-39

3 **Brault JS**, Smith J, Currier BL. Partial lumbosacral transitional vertebra resection for contralateral facetogenic pain. *Spine (Phila Pa 1976)* 2001; **26**: 226-229

4 **Jonsson B,** Stromqvist B, Egund N. Anomalous lumbosacral articulations and low-back pain. Evaluation and treatment. *Spine* 1989; **14:** 831-834

5 **Santavirta S**, Tallroth K, Ylinen P, Suoranta H. Surgical treatment of Bertolotti's syndrome. Follow-up of 16 patients. *Arch Orthop Trauma Surg* 1993; **112**: 82-87

6 **Castellvi AE**, Goldstein LA, Chan DP. Lumbosacral transitional vertebrae and their relationship with lumbar extradural defects. *Spine* (Phila Pa 1976) **1984; 9**: 493-495

7 **Bron JL**, van Royen BJ, Wuisman PI. **The clinical significance** of lumbosacral transitional anomalies. *Acta Orthop Belg* 2007; **73**: 687-695

8 **Konin GP**, Walz DM. Lumbosacral transitional vertebrae: classification, imaging findings, and clinical relevance. *AJNR Am J Neuroradiol* 2010; **31**: 1778-1786

9 **Hughes RJ**, Saifuddin A. Numbering of lumbosacral transitional vertebrae on MRI: role of the iliolumbar ligaments. *AJR Am J Roentgenol* 2006; **187**: W59-W65

10 **Luoma K**, Vehmas T, Raininko R, Luukkonen R, Riihimäki H. Lumbosacral transitional vertebra: relation to disc degeneration and low back pain. *Spine* (Phila Pa 1976) 2004; **29**: 200-205

11 **O'Driscoll CM**, Irwin A, Saifuddin A. Variations in morphology of the lumbosacral junction on sagittal MRI: correlation with plain radiography. *Skeletal Radiol* 1996; **25**: 225-230

12 **Bertolloti M.** Contribute alla conoscenza dei vizi di differenzazione del rachide con speciale reguardo all assimilazione sacrale della v lombare. *La Radiologia Medica* 1917; **4:** 113-144

13 **Hellems HK**, Keats TE. Measurement of the normal lumbosacral angle. *Am J Roentgenol Radium Ther Nucl Med* 1971; **113**: 642-645

14 **Wigh RE**. The thoracolumbar and lumbosacral transitional junctions. *Spine* (Phila Pa 1976) **1980; 5**: 215-222

S- Editor Cheng JX **L- Editor** Logan S **E- Editor** Xiong L

World Journal of Radiology

Online Submissions: http://www.wjgnet.com/1949-8470office
wjr@wjgnet.com
doi:10.4329/wjr.v4.i3.102

World J Radiol 2012 March 28; 4(3): 102-108
ISSN 1949-8470 (online)

BRIEF ARTICLE

Relationship between patient centering, mean computed tomography numbers and noise in abdominal computed tomography: Influence of anthropomorphic parameters

Mi Sung Kim, Sarabjeet Singh, Elkan Halpern, Sanjay Saini, Mannudeep K Kalra

Mi Sung Kim, Myongji Hospital, Kwandong University, 522 Naegok-dong, Gangneung-si, Gangwon-do 220-801, South Korea
Sarabjeet Singh, Elkan Halpern, Sanjay Saini, Mannudeep K Kalra, Department of Radiology, Massachusetts General Hospital, Harvard Medical School, Boston, MA 02114, United States
Author contributions: Kim MS helped in manuscript writing and editing, literature search; Singh S helped in organizing the study, literature search, manuscript writing; Kalra MK helped in overall study design and manuscript writing.
Supported by Research funding from GE Healthcare (Waukesha, Wis) (to Kalra MK)
Correspondence to: Dr. Sarabjeet Singh, Department of Radiology, Massachusetts General Hospital, Harvard Medical School, 55 Fruit St, Boston, MA 02114,
United States. ssingh6@partners.org
Telephone: +617-643-4583 Fax: +617-643-0111
Received: January 18, 2011 Revised: February 28, 2012
Accepted: March 7, 2012
Published online: March 28, 2012

Abstract

AIM: To determine the influence of anthropomorphic parameters on the relationship between patient centering, mean computed tomography (CT) numbers and quantitative image noise in abdominal CT.

METHODS: Our Institutional Review Board approved study included 395 patients (age range 21-108, years; male:female = 195:200) who underwent contrast-enhanced abdominal CT on a 16-section multi-detector row scanner (GE LightSpeed 16). Patient centering in the gantry isocenter was measured from the lateral localizer radiograph (off center S = patient off centered superior to isocenter; off center I = patient off centered inferior to isocenter). Mean CT numbers (Hounsfield Units: HU) and noise (standard deviation of CT numbers: SD) were measured in the anterior (aHU, aSD) and posterior (pHU, pSD) abdominal wall subcutaneous fat and liver parenchyma (LivHU, LivSD) at the level of the porta hepatis. Patients' age, gender, weight, body mass index and maximal anteroposterior diameter were recorded. The data were analyzed using linear regression analysis.

RESULTS: Most patients (81%; 320/395) were not correctly centered in the gantry isocenter for abdominal CT scanning. Mean CT numbers in the abdominal wall increased significantly with an increase in the off-centering distance, regardless of the direction of the off-center ($P < 0.05$). There was a substantial increase in pSD ($P = 0.01$) and LivSD ($P = 0.017$) with off-centering. Change in mean CT numbers and image noise along the off-center distance was influenced by the patient size ($P < 0.01$).

CONCLUSION: Inappropriate patient centering for CT scanning adversely affects the reliability of mean CT numbers and image noise.

Key words: Automatic exposure control; Computed tomography radiation dose reduction; Patient offcentering; Tube current modulation

Peer reviewers: Tilo Niemann, MD, Department of Radiology, University Hospital Basel, Petersgraben 4, CH-4031 Basel, Switzerland; Hadi Rokni Yazdi, MD, Associate Professor, Department of Radiology, Central Radiology, Imam Khomeini Hospital, Tehran University of Medical Sciences, Keshavarz Blvd, Tehran 1419733141, Iran; Zhonghua Sun, PhD, Discipline of Medical Imaging, Department of Imaging and Applied Physics, Curtin University of Technology, GPO Box U 1987, Perth, Western Australia 6845, Australia

Kim MS, Singh S, Halpern E, Saini S, Kalra MK. Relationship between patient centering, mean computed tomography numbers and noise in abdominal computed tomography: Influence of an-

thropomorphic parameters. *World J Radiol* 2012; 4(3): 102-108 Available from: URL: http://www.wjgnet.com/1949-8470/full/v4/i3/102.htm DOI: http://dx.doi.org/10.4329/wjr.v4.i3.102

INTRODUCTION

Increasing use of computed tomography (CT) has raised concerns about potential risk of radiation-induced carcinogenesis. Clinical and technical strategies have been suggested to reduce radiation dose without compromising diagnostic information[1-6]. For radiation dose reduction, current multi-detector row computed tomography (MDCT) scanners are armed with several technologies such as X-ray intensity shaping bow-tie filters and automatic exposure control (AEC) techniques.

Bow-tie or beam shaping filters configure the X-ray beam to the cross-sectional geometry of the body region being scanned, so that the thinner peripheral portion of the body receives a lower radiation dose compared to the thicker central portion of the cross section[7]. These filters affect the incident X-ray beam characteristics which in turn affect their attenuation from the patient. Errors in centering of patients in the CT gantry isocenter can result in overestimation or underestimation of regional X-ray attenuation, which in turn can lead to erroneous estimation of tube current with the AEC techniques[3]. Thus, both bow-tie filters and AEC techniques require optimum patient centering within the gantry isocenter to reduce radiation dose while maintaining diagnostic image quality[8].

Previous studies have shown that inappropriate patient centering on the gantry affects image quality and radiation dose obtained with AEC techniques[9,10]. However, the effect of patient off-centering on mean CT numbers and image noise has not been assessed with respect to patient size. Therefore, the purpose of our study is to determine the influence of anthropomorphic parameters on the relationship between patient centering, mean CT numbers and quantitative image noise in abdominal CT.

MATERIALS AND METHODS

Patient population

This retrospective study was approved by the Human Research Committee of the Institutional Review Board of Massachusetts General Hospital.

The requirement for informed consent was waived. The study protocol was in compliance with the Health Insurance Portability and Accountability Act.

The study comprised 395 consecutive patients who underwent routine abdominal CT (mean age, 57 years; age range, 21-108 years) at a single tertiary health care hospital in October 2009. There were 195 male patients (49%, 195/395 patients; mean age, 57 years; age range, 21-108 years) and 200 female patients (51%, 200/395 patients; mean age, 57 years; age range, 20-94 years).

Patient body weight and body mass index [(BMI = weight in kg/(height in meters)^2] were recorded. Maximal anteroposterior (AP) diameter of the abdomen was measured from the lateral localizer radiograph. Lateral localizer radiographs were preferred over transverse CT images, as often in large patients transverse CT images do not have skin to skin field of view, whereas lateral radiographs have skin to skin coverage in all patients from use of a large field of view of 50 cm.

The outcome variables of our study included CT numbers [Hounsfield units (HU)], and quantitative image noise [standard deviation of the CT numbers (SD)] measured in the subcutaneous fat of the anterior and posterior abdominal wall as well as in liver parenchyma.

Scanning protocol

Routine contrast-enhanced abdominal CT was performed on a 16-section multi-detector row scanner (GE LightSpeed 16; GE Healthcare, Waukesha, WI, United States) in all patients included in our study. In our institution, we acquired two localizer radiographs for each patient in lateral and AP projections at 80 kVp and 20 mA.

Transverse CT images were acquired from the top of the diaphragm to the pubic symphysis in all patients in single helical acquisition following administration of non-ionic contrast medium (Iopamidol 370 mg%, Bracco Diagnostics, Princeton, NJ, United States) injected at the rate of 2.5-3 cc per second. The scanning parameters comprised of 120 kVp, 0.5 s gantry rotation time, 1.375:1 beam pitch, 27.5 mm table speed per gantry rotation, and 16 × 1.25 mm detector collimation. Images were reconstructed with 5 mm section thickness at 5 mm intervals using a standard soft tissue reconstruction kernel.

A combined automatic exposure control technique (Auto mA 3D, GE Healthcare) was used to scan all patients. This technique uses the noise index as a surrogate for image quality, or more precisely, the average noise in the entire image. The Auto mA 3D technique performs tube current modulation at different projections (angular modulation or x-y modulation) with in individual section positions as well as at different section positions along the patient's long axis or scanning direction (z-modulation). In addition to the noise index, the technique requires users to specify a range of tube current between which such tube current modulation should occur. The latter allows the user to control the extent of tube current modulation. As per our standard department protocols, the noise index is adjusted according to body weight: < 60 kg, 10 noise index; 61-90 kg, 12.5 noise index; > 91 kg, 15 noise index. The minimum and maximum tube current limits were set at 120 and 440 mA.

Assessment of patient centering

CT images were reviewed on a clinical web-based PACS within the firewalls of our hospital (Radamicas, Merge Healthcare, Hartland, WI, United States). Patient off-center distance from the gantry isocenter was measured from lateral localizer radiographs (Figure 1) by one of the authors (Kim MS with 10 years of experience). Off-

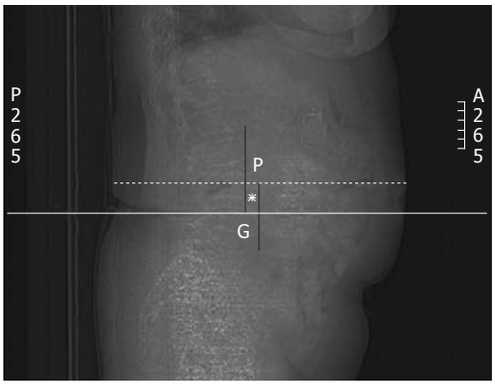

Figure 1 Calculation of off-centering distance. First, the gantry isocenter (G) was determined as the midpoint of the entire image (thick line). Next, maximal anterior-posterior diameter of the patient (broken line) was measured. Lastly, distance (asterix) between the midpoints of maximal patient diameter (P) and gantry isocenter (G) was measured to obtain the off-centering distance.

centering of patients was estimated from the images by first determining the gantry isocenter as the midpoint of the entire image or the scan field of view. Next, the maximal anterior-posterior diameter of the patient was measured. Lastly, distance between the midpoints of maximal patient diameter and the gantry isocenter was measured to obtain the off-centering distance.

Once the lateral projection localizer radiograph is acquired, technologists plan the acquisition of transverse images. For reconstruction of transverse images, the planning field of view (FOV) defaults to the center of the localizer radiograph. In the case of appropriate patient centering, technologists only have to adjust the size of display FOV. However, with patient off-centering, in our experience the technologists change the position of display FOV without actually re-centering the patient in the gantry isocenter. This re-centering of display FOV rather than re-centering of the patient, leads to patient off-centering. Therefore, for the purpose of our study, we used localizer radiographs instead of transverse CT images to estimate patient off-centering. In addition, previously described automatic centering techniques have also used lateral localizer radiographs to estimate the extent of patient off-centering[7].

The off-center distance was arbitrarily divided into 5 groups based on the distance between the patient AP center on the lateral projection radiograph and the gantry isocenter; 0-5 mm (considered ideal centering), 6-10 mm, 11-20 mm, 21-30 mm and greater than 30 mm from the gantry isocenter. The direction of off-centering (superior and inferior) compared to gantry isocenter was also evaluated.

Regions of interest and radiation dose

After measuring the distance and direction of off-centering, the mean CT numbers and their image noise (standard deviation of HU) were measured from the 5 mm contrast-enhanced transverse abdominal CT image in liver parenchyma at the level of the porta hepatis using a circular 30-50 mm^2 region of interest (ROI). Mean CT numbers and image noise were measured in the anterior and posterior abdominal wall subcutaneous fat using circular 10-30 mm^2 regions of interest.

CT dose index volume ($CTDI_{vol}$ in mGy) from the dose information page of each CT examination included in our study was recorded.

Statistical analysis

Data were tabulated in a spreadsheet program (Microsoft Excel; Microsoft, Inc., Princeton, NJ, United States). Statistical analysis was performed using a statistical analysis package (SAS/STAT 9.2; SAS Institute, Cary, NC, United States). Linear regression analysis was performed to evaluate the relationship between off-centering, mean CT numbers and image noise. In addition, the same analysis was used to evaluate the influence of patient age, gender, body weight, BMI and maximal AP diameter of abdomen on the variability of mean CT numbers, SD and $CTDI_{vol}$ with off-centering. A *P* value less than 0.05 was considered to indicate a statistically significant difference.

RESULTS

Centering and off-centering: distribution and magnitude

Only 19% of patients (75/395 patients; male:female, 41:34) were centered correctly in the gantry isocenter. Most patients (81%, 320/395 patients; male:female, 154:166; mean age, 57 years) were off-centered with respect to the gantry isocenter. In terms of magnitude of off-centering, most patients were off-centered by 11-20 mm (39%, 125/320 patients) followed by 21-30 mm off-centering (26%, 85/320 patients) and greater than 31 mm off-centering (17%, 63/320 patients) (Table 1).

Amongst the off-centered patients, 99 patients were centered superior to the gantry isocenter (off-center S, 31%, 99/320 patients; male:female, 53:46; mean age, 58 years) and 221 patients were centered inferior to the gantry isocenter (off-center I , 69%, 221/320 patients; male:female, 101:120; mean age, 57 years). Interestingly, most patients with greater than 31 mm off-centering were positioned inferior to the gantry isocenter (84%, 53/63 patients; male: female, 21: 32) (Table 1).

Off-centering, patient demographics and size

There was no significant difference between patient age in the centered and off-centered groups or in the different off-centering groups (P = 0.15). Although we had almost equitable distribution of male and female patients in our study, more men (n = 40/75 patients, 54%) were centered adequately in the gantry isocenter than women (n = 35/75 patients, 46%).

There was no significant difference between patient weight, AP diameter and BMI of centered (weight = 78.6 ± 27.6 kg, AP diameter, 28.2 ± 5.5 cm, BMI 26.7 ± 6.3 kg/m^2) and off-centered (weight = 78.0 ± 19.0 kg, AP diameter, 28.6 ± 5.5 cm, BMI 27.6 ± 6.0 kg/m^2) patients (P = 0.41, 0.29 and 0.16, respectively). However, patients off-centered above the gantry isocenter (weight = 89.4 ± 21.3 kg, AP diameter, 32.1 ± 5.8 cm, BMI 30.7 ± 7.1 kg/m^2)

Table 1 Patient size, computed tomography numbers and quantitative image noise at different magnitude and direction of off-centering (mean ± SD)

Distance (#patients)	Direction (#patients)	BMI (kg)	Weight (mGy)	AP diameter (cm)	$CTDI_{vol}$	aHU	pHU	LivHU	aSD	pSD	LivSD
0-5 mm	Ideal	27	77	28	13.4	-97.5 ± 27.2	-92.8 ± 14.9	117.0 ± 43.4	9.9 ± 4.9	11.8 ± 4.3	17.0 ± 3.7
(*n* = 75)	centering	(18-59)	(31-181)	(17-52)	(5.2-48.3)	(-117~-45)	(-121~-34)	(63~153)	(5~45)	(4~33)	(9~15)
6-10 mm	A	28	76	27	14.1	-98.2 ± 9.3	-90.9 ± 9.5	114.0 ± 20.0	11.0 ± 2.6	12.3 ± 3.0	17.8 ± 3.4
(*n* = 47)	(*n* = 20)	(20-38)	(54-107)	(17-33)	(9.0-33.0)	(-115~-78)	(-106~ -71)	(55~153)	(6~18)	(7~16)	(10~30)
	B	28	79	29	13	-95.1 ± 13.1	-88.7 ± 19.3	117.6 ± 26.9	9.7 ± 2.3	13.4 ± 4.01	17.4 ± 5.2
	(*n* = 27)	(21-40)	(54-127)	(20-53)	(7.2-23.4)	(-115~-60)	(-109~-59)	(80~167)	(6~15)	(8~23)	(13~23)
11-20 mm	A	30	88	31	15.4	-96.9 ± 13.4	-93.3 ± 14.0	109.9 ± 22.5	11.0 ± 3.6	12.6 ± 3.7	18.1 ± 4.9
(*n* = 125)	(*n* = 47)	(19-51)	(54-130)	(23-40)	(9.2-42.2)	(-116~-45)	(-114~-44)	(63~158)	(5~22)	(7~23)	(11~31)
	B	27	74	28	13.2	-97.1 ± 13.1	-92.9 ± 11.8	119.3 ± 25.2	9.5 ± 2.4	11.9 ± 3.2	17.9 ± 4.3
	(*n* = 78)	(17-49)	(35-136)	(15-44)	(5.8-34.5)	(-115~-53)	(-124~63)	(31~175)	(6~18)	(8~21)	(11~29)
21-30 mm	A	29	89	32	13.9	-96.5 ± 10.9	-89.0 ± 12.8	107.4 ± 26.31	12.4 ± 3.31	13.6 ± 3.91	18.7 ± 3.81
(*n* = 85)	(*n* = 22)	(20-37)	(46-129)	(19-53)	(6.2-26.7)	(-112~-74)	(-118~-56)	(40~142)	(7~20)	(9~24)	(6~20)
	B	26	73	27	12.7	-94.6 ± 13.7	-85.3 ± 13.01	122.3 ± 25.1	10.4 ± 2.8	13.3 ± 3.71	17.9 ± 4.9
	(*n* = 63)	(15-35)	(40-109)	(17-38)	(5.9-23.5)	(-113~-44)	(-110~-43)	(55~177)	(6~23)	(6~22)	(11~34)
[3]31 mm (*n*	A	36	96	34	14.2	-94.3 ± 7.4	-89.1 ± 16.6	116.6 ± 24.8	16.4 ± 7.01	14.0 ± 5.0	26.7 ± 4.01
= 63)	(*n* = 10)	(22-52)	(65-141)	(28-46)	(10.1-21.1)	(-103~-80)	(-100~-77)	(81~153)	(9~29)	(8~24)	(21~38)
	B	26	74	27	14.1	-94.1 ± 13.7	-87.1 ± 13.5[a]	125.0 ± 24.8[a]	9.4 ± 2.5	13.5 ± 4.7[a]	17.2 ± 4.0
	(*n* = 53)	(19-38)	(49-118)	(19-36)	(6.1-42.6)	(-129~-68)	(-113~-61)	(63~167)	(6~18)	(8~30)	(11~30)

[a]Implies significant statistical difference ($P < 0.05$). Off-centering distance and direction had a greater effect on image noise as compared to the mean computed tomography (CT) numbers. Numbers in parentheses are ranges. A: Superior off-centering; B: Inferior off-centering; aHU: Mean CT numbers in the anterior abdominal wall; pHU: Mean CT numbers in the posterior abdominal wall; LivHU: Mean CT numbers in liver, aSD: Quantitative noise in the anterior abdominal wall; pSD: Quantitative noise in the posterior abdominal wall; LivSD: Quantitative noise in the liver.

Table 2 Computed tomography numbers and quantitative image noise for ideally centered and off-centered patients (mean ± SD)

Direction	aHU	pHU	LivHU	aSD	pSD	LivSD
Ideal centering	-97.5 ± 15.9	-92.8 ± 15.1	117.0 ± 21.5	9.9 ± 4.9	11.8 ± 4.3	17.0 ± 3.7
A	-96.9 ± 11.5 (0.4)	-91.4 ± 12.5 (0.25)	111.1 ± 24.3 (0.05)	11.8 ± 4.1 (0.004)[a]	12.8 ± 3.8 (0.045)[a]	18.8 ± 5.3 (0.003)[a]
B	-95.5 ± 14.4 (0.16)	-89.1 ± 14.5 (0.03)[a]	121.0 ± 24.5 (0.1)	9.8 ± 2.6 (0.33)	12.8 ± 3.9 (0.03)[a]	17.6 ± 4.3 (0.09)

[a]Implies significant statistical difference ($P < 0.05$). Numbers in parentheses are *P* values. A: Superior off-centering; B: Inferior off-centering; aHU: Mean computed tomography (CT) numbers in the anterior abdominal wall; pHU: Mean CT numbers in the posterior abdominal wall; LivHU: Mean CT numbers in the liver; aSD: Quantitative noise in the anterior abdominal wall: pSD: Quantitative noise in the posterior abdominal wall; LivSD: Quantitative noise in the liver.

were significantly larger than patients centered below the gantry isocenter (weight = 73.1 ± 15.8 kg, AP diameter, 27.0 ± 4.5 cm, BMI 26.0 ± 4.9 kg/m^2) when the off-centering distance exceeded 10 mm ($P < 0.0001$). The largest differences in BMI, abdominal AP diameter and weight between off-centering superior and inferior were seen with greater than 30 mm off-centering ($P < 0.0001$) (Table 1). For subjects with less than 10 mm off-centering, there was no difference between body weight, BMI or AP diameter in the superior (weight = 79.3 ± 15.4 kg, AP diameter, 28.4 ± 4.3 cm, BMI 28.9 ± 6.0 kg/m^2) and inferior off-centering directions (weight = 81.1 ± 22.6 kg, AP diameter, 29.8 ± 7.2 cm, BMI 28.8 ± 6.8 kg/m^2) (P = 0.36, 0.19 and 0.48, respectively).

The effect of off-centering on $CTDI_{vol}$ is illustrated in Table 1. There was no significant difference between $CTDI_{vol}$ in patients with and without appropriate centering ($P = 0.8$).

Off-centering and image quality

The relationship between distance along the direction of off-center, mean CT numbers and objective image noise is summarized in Table 2. Regardless of the direction of off-centering, the mean CT numbers measured in the abdominal wall were significantly higher in off-centered patients compared to those centered correctly in the gantry isocenter (P = 0.034-0.0009). When the direction of off-centering was taken into account, only the mean CT numbers in the posterior abdominal wall increased significantly for patients centered below the gantry isocenter (P = 0.03). This change in mean CT numbers was less than 10% in absolute numbers (Table 2). When the magnitude of off-centering was taken into account, there was no significant change in mean CT numbers with up to 20 mm off-centering from the gantry isocenter (P = 0.1-0.47).

When data were normalized for patients' age, gender, weight, BMI and AP diameters, mean CT numbers in all three regions between superior and inferior off-centering varied significantly for patients with different body weights ($P < 0.001$).

Image noise increased significantly in the posterior abdominal wall and liver parenchyma with an increase in

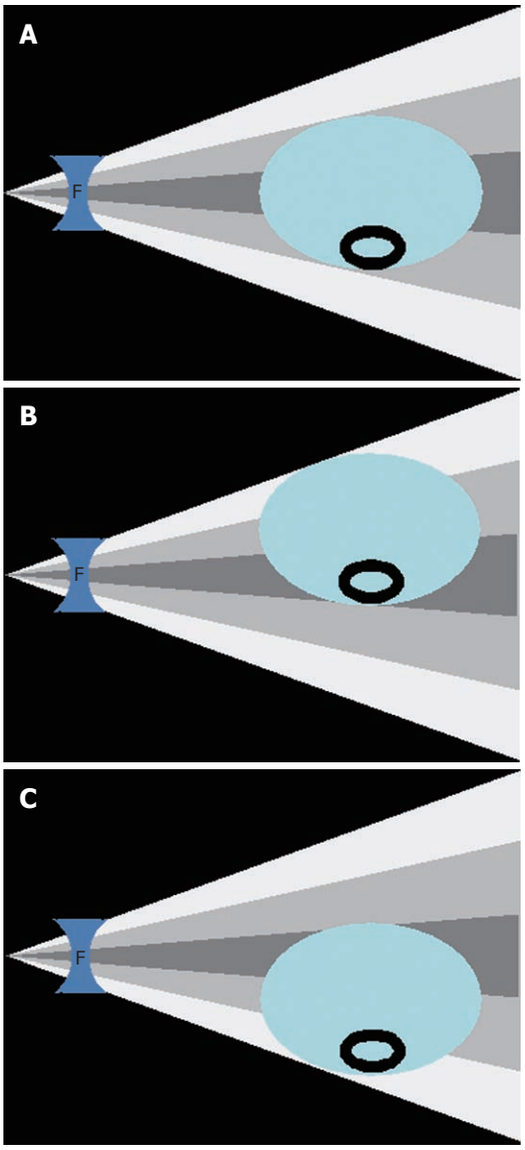

Figure 2 More attenu¬ated X-ray beam is received in the center of bow-tie filter corresponds to the posterior abdominal wall and the anterior abdominal wall when patients are centered the gantry isocenter. A: When the patient is centered in the gantry isocenter, bow-fie filter (F) allows most X-rays (darker gray) to traverse thicker, central parts of the patient and fewer X-rays (white) in the peripheral portion to pass through thinner, peripheral parts of the patient; B: When the patient is positioned above the gantry isocenter, the anterior portion of the patient's abdominal wall which is further from the gantry isocenter receives fewer X-rays (white) with a consequent increase in noise, whereas the posterior abdominal wall receives the central more intense X-ray beam (darker gray), and therefore has less noise; C: When the patient is positioned below the gantry isocenter, the anterior portion of the patient's abdominal wall coincides with the gantry isocenter to receive more X-rays, resulting in no significant change in its noise, whereas the posterior abdominal wall moves away from the gantry isocenter and receives fewer X-rays which leads to higher noise.

off-centering distance. When the direction of off-centering was taken into account, noise in the anterior abdominal wall ($P = 0.004$) and liver ($P = 0.003$) increased significantly only with superior off-centering, whereas noise in the posterior abdominal wall increased significantly with both directions of off-centering ($P = 0.03$-0.045). There was a significant difference in image noise in the abdominal wall and liver between superior and inferior off-centering after normalizing BMI, body weight and maximal AP diameter of abdomen ($P < 0.0001$). Although there was a difference in objective image noise between superior and inferior off-centering, subjective image quality was not compromised for all 397 abdominal CT examinations, as reviewed from the radiology reports.

DISCUSSION

The role of appropriate patient centering has been emphasized for CT scanning, in particular when using AEC techniques and bow-tie filters to reduce radiation dose[8,9]. Optimal patient centering implies matching the patient's mean center of mass with the center of the bow-tie filter which coincides with the center of the gantry in the CT scanner for optimal use of bow-tie filters. When a patient is not centered optimally, inappropriate compensation of the X-ray beam by bow-tie filters allows more X-ray to the surface of the thinner peripheral portion of the body while the X-ray beam incident upon the thicker central portion is reduced.

Li *et al*[7] reported that the peripheral and surface radiation dose increases by 12% and 18%, respectively, in images of an elliptical water phantom centered 30 mm below the isocenter, and by 41% and 49% in the same phantom centered 60 mm below the isocenter. These authors reported an overall increase of 6% and 22% in overall image noise at 3 and 6 cm phantom off-centering from the gantry isocenter. Conversely, Matsubara *et al*[10] reported a much smaller increase in overall image noise (15%) with 5 cm off-centering of a circular water phantom.

Our study highlights the variation in image noise for different anatomic locations in the abdomen. We noted a maximal increase in image noise of 16.5% in the posterior abdominal wall and 10% in the liver with patient off-centering of greater than 3 cm. In contrast, the increase in image noise with the same magnitude of off-centering was only 4% in the anterior abdominal wall. These discrepancies in change of image noise may be explained on the basis of differences in the regional X-ray beam attenuation in anterior and posterior abdominal wall and liver. Compared to the low attenuation from soft tissue of the anterior abdominal wall, the posterior abdominal wall has higher attenuation due to the vertebral column and therefore also has a greater increase in image noise with off-centering compared to the anterior abdominal wall. Since liver has higher attenuation than the anterior abdominal wall but lower than that of the posterior abdominal wall, with off-centering there is an intermediate change in image noise in the liver.

Our study also highlights the influence of directionality of vertical off-centering on image noise. When patients are centered above the gantry isocenter, the center of bow-tie filter corresponds to the posterior abdominal wall and the anterior abdominal wall receives more attenuated X-ray beam (Figure 2). This is likely the reason for a greater increase in image noise in the anterior abdominal wall than in the posterior abdominal wall with superior

off-centering. Conversely, when patients are off-centered below the gantry isocenter, there is a greater increase in the posterior abdominal wall noise as it lies in the path of the more attenuated X-ray beam traversing through the peripheral thicker portion of the bow-tie filter.

This selective change in image noise with directionality of off-centering can also be explained on the basis of differences in $CTDI_{vol}$ with off-centering of patients. We noted a slightly higher $CTDI_{vol}$ with off-centering in the superior direction than in the inferior direction, and that may be due to the fact that patients centered above the gantry isocenter were substantially larger than patients centered below the gantry isocenter. It must be emphasized that with use of automatic exposure control, the CTDI vol changes with the size of the patient.

We also found that with off-centering there is some change in the CT numbers in different geometric locations of the images although this change is much less compared to the change in image noise (1%-5% relative to ideal patient centering). This modest change in CT numbers with off-centering may also be a result of differential beam attenuation by bow-tie filters in off-centered patients as relevant to the image noise.

Interestingly, we also noted a substantial influence of patient size on magnitude and direction of off-centering. Patients centered above the isocenter tended to be substantially larger than those centered below the isocenter. This may be explained on the basis of incorrect or underestimation of centering of patients with large body habitus. Unfortunately, we found that despite rising awareness about the risks associated with CT scanning and recent publications emphasizing an increase in radiation dose with patient off-centering, there was a very modest difference between the proportion of off-centered patients in our study (81%) compared to that reported in two prior studies (95%-95.5%) conducted at different institutions[7,11]. In our institution, technologists are reminded about the importance of patient centering from time to time, although there is no fixed routine or interval for completing such notification. The fact that off-centering continues to occur in the vast majority of our patients perhaps suggests that manual off-centering by the CT technologists is either not properly performed or cannot be performed with a great deal of accuracy. Regardless of the reasons for off-centering, there is an urgent need for an automatic assisted patient centering technique on CT equipments which are otherwise being armed with sophisticated dose reduction techniques such as automatic exposure control and bow-tie filters. In this direction, it is important to note that some vendors have introduced a feature to allow CT users to change table position for better patient centering directly from the CT scanner (Siemens Definition Flash, Siemens Medical Solutions, Forchheim, Germany) user interface after checking the localizer radiograph. This ability helps technologists to "fine tune" or "correct" patient centering without the need to go into the CT gantry suite.

There are clinical implications resulting from our study. There needs to be greater education and training of the CT technologists for patient centering. The method of centering patients with large body habitus needs specific attention. Differential distribution of image noise is influenced by both magnitude and direction of off-centering and hence off-centering should be avoided in order to maintain a uniform image quality. Radiologists should bear in mind that there is a slight but statistically insignificant change in mean CT numbers in the liver with off-centering.

There are limitations in our study. Although we included a large number of patients in our study, we did not perform a power analysis to determine the actual sample size required to test our hypothesis. In particular, there were fewer patients in the off-centering groups with more than 30 mm off-centering distance from the gantry isocenter. Another limitation was that the size and location of the ROIs being measured were not homogeneous for each patient. The size of ROIs in abdominal subcutaneous fat ranged from 10 to 30 mm^2 according to the amount of subcutaneous fat. Likewise, the liver ROIs ranged from 30 to 50 mm^2 to include just the liver parenchyma and avoid inclusion of large blood vessels within the ROI. Although we did not perform a formal detailed subjective image quality assessment, we carried out a retrospective analysis of the radiology reports to check image quality of these CT examinations. Study reports are stored in the hospital database along with the images and comments on suboptimal image quality affecting diagnostic confidence. We found that none of the examinations showed suboptimal image quality. Another limitation of our study is that we did not compare the effect of different off-centering distances and directions in the same patient as it was not feasible and practical to scan patients several times with different off-centering. It is possible, although unproven from our study, that greater changes in CT numbers and image noise may have come to light on an individual patient basis. We also did not assess the effect of horizontal off-centering of the patients on image noise and mean CT numbers.

In conclusion, inappropriate patient centering in the gantry isocenter adversely affects the mean CT numbers and image noise along the distance of off-center. Therefore, attention to appropriate patient centering is important for maintaining image quality and optimizing radiation dose during MDCT examination, particularly in large patients.

COMMENTS

Background

Computed tomography (CT) radiation dose related risks are one of the major concerns amongst the medical community, media and general public. There are several attempts in the past to optimize radiation dose associated with CT by following the principle of "as low as reasonably achievable". X-ray beam shaping filters are designed to expose the peripheral thinner portions of the body with lower radiation dose as compared to thicker central portion. This assumption only works when the authors have the patient perfectly centered in the X-ray beam. Any offcentering of patient affects the selected tube current and finally radiation dose associated with CT.

Research frontiers

Prior studies have shown that patient offcentering from the CT scanner iso-

center does affect the associated radiation dose with tube current modulation techniques. However, the relationship between mean CT numbers or the Hounsfield values and the image noise has not been assessed with respect to patient size.

Innovations and breakthroughs

The study highlights the influence of directionality of vertical off-centering on image noise. When patients are centered above the gantry isocenter, the center of bow-tie filter corresponds to the posterior abdominal wall and the anterior abdominal wall receives more attenuated X-ray beam. The authors also found that with off-centering there is some change in the CT numbers in different geometric locations of the images although this change is much less compared to the change in image noise (1%-5% relative to ideal patient centering). This modest change in CT numbers with off-centering may also be a result of differential beam attenuation by bow-tie filters in off-centered patients as relevant to the image noise.

Applications

Clinical implications of this study are the need for greater education and training of the CT technologists for patient centering. The method of centering patients with large body habitus needs specific attention. Differential distribution of image noise is influenced by both magnitude and direction of off-centering and hence off-centering should be avoided in order to maintain a uniform image quality. Radiologists should bear in mind that there is a slight but statistically insignificant change in mean CT numbers in the liver with off-centering.

Terminology

Bow-tie or beam shaping filters: These filters configure the X-ray beam to the cross-sectional geometry of the body region being scanned, so that the thinner peripheral portion of the body receives a lower radiation dose compared to the thicker central portion of the cross section. Patient Off-centering: Any deviation of patients center from the CT scanner gantry iso-center, which can be either vertically or horizontally.

Peer review

This is a good descriptive study in which authors analyze the affect of patient offcentering on CT image noise and Hounsfield Units numbers. The results are interesting and show an increase in 16% image noise in posterior abdominal wall and suggest a need for education and training of CT technologist in more accurate patient centering.

REFERENCES

1 **Donnelly LF**, Emery KH, Brody AS, Laor T, Gylys-Morin VM, Anton CG, Thomas SR, Frush DP. Minimizing radiation dose for pediatric body applications of single-detector helical CT: strategies at a large Children's Hospital. *AJR Am J Roentgenol* 2001; **176**: 303-306

2 **Maher MM**, Kalra MK, Toth TL, Wittram C, Saini S, Shepard J. Application of rational practice and technical advances for optimizing radiation dose for chest CT. *J Thorac Imaging* 2004; **19**: 16-23

3 **Kalra MK**, Maher MM, Toth TL, Hamberg LM, Blake MA, Shepard JA, Saini S. Strategies for CT radiation dose optimization. *Radiology* 2004; **230**: 619-628

4 **Sodickson A**, Baeyens PF, Andriole KP, Prevedello LM, Nawfel RD, Hanson R, Khorasani R. Recurrent CT, cumulative radiation exposure, and associated radiation-induced cancer risks from CT of adults. *Radiology* 2009; **251**: 175-184

5 **Griffey RT**, Sodickson A. Cumulative radiation exposure and cancer risk estimates in emergency department patients undergoing repeat or multiple CT. *AJR Am J Roentgenol* 2009; **192**: 887-892

6 **Feng ST**, Law MW, Huang B, Ng S, Li ZP, Meng QF, Khong PL. Radiation dose and cancer risk from pediatric CT examinations on 64-slice CT: a phantom study. *Eur J Radiol* 2010; **76**: e19-e23

7 **Li J**, Udayasankar UK, Toth TL, Seamans J, Small WC, Kalra MK. Automatic patient centering for MDCT: effect on radiation dose. *AJR Am J Roentgenol* 2007; **188**: 547-552

8 **Avilés Lucas P**, Castellano IA, Dance DR, Vañó Carruana E. Analysis of surface dose variation in CT procedures. *Br J Radiol* 2001; **74**: 1128-1136

9 **Kalra MK**, Maher MM, Kamath RS, Horiuchi T, Toth TL, Halpern EF, Saini S. Sixteen-detector row CT of abdomen and pelvis: study for optimization of Z-axis modulation technique performed in 153 patients. *Radiology* 2004; **233**: 241-249

10 **Matsubara K**, Koshida K, Ichikawa K, Suzuki M, Takata T, Yamamoto T, Matsui O. Misoperation of CT automatic tube current modulation systems with inappropriate patient centering: phantom studies. *AJR Am J Roentgenol* 2009; **192**: 862-865

11 **Li J**, Udayasankar UK, Toth TL, Small WC, Kalra MK. Application of automatic vertical positioning software to reduce radiation exposure in multidetector row computed tomography of the chest. *Invest Radiol* 2008; **43**: 447-452

S- Editor Cheng JX **L- Editor** Webster JR **E- Editor** Xiong L

World Journal of Radiology

Online Submissions: http://www.wjgnet.com/1949-8470office
wjr@wjgnet.com
doi:10.4329/wjr.v4.i3.109

World J Radiol 2012 March 28; 4(3): 109-114
ISSN 1949-8470 (online)

BRIEF ARTICLE

Ablation margin assessment of liver tumors with intravenous contrast-enhanced C-arm computed tomography

Jin Iwazawa, Shoichi Ohue, Naoko Hashimoto, Takashi Mitani

Jin Iwazawa, Naoko Hashimoto, Takashi Mitani, Department of Radiology, Nissay Hospital, 6-3-8 Itachibori, Nishiku, Osaka 550-0012, Japan
Shoichi Ohue, Department of Radiology, Komatsu Hospital, 11-6 Kawakatsucho, Neyagawa 572-8567, Japan
Author contributions: Iwazawa J and Ohue S performed the radiofrequency ablations; Hashimoto N, Iwazawa J and Ohue S collected and analyzed the data; Mitani T participated in the design and coordination of the study.
Correspondence to: Jin Iwazawa, MD, Department of Radiology, Nissay Hospital, 6-3-8 Itachibori, Nishiku, Osaka 550-0012, Japan. iwazawa.jin@nissay-hp.or.jp
Telephone: +81-6-65433581 Fax: +81-6-65326482
Received: August 27, 2011 Revised: December 8, 2011
Accepted: December 15, 2011
Published online: March 28, 2012

Abstract

AIM: To evaluate the feasibility of intravenous contrast-enhanced C-arm computed tomography (CT) for assessing ablative areas and margins of liver tumors.

METHODS: Twelve patients (5 men, 7 women; mean age, 69.5 years) who had liver tumors (8 hepatocellular carcinomas, 4 metastatic liver tumors; mean size, 16.3 mm; size range, 8-20 mm) and who underwent percutaneous radiofrequency ablations (RFAs) with a flat-detector C-arm system were retrospectively reviewed. Intravenously enhanced C-arm CT and multidetector computed tomography (MDCT) images were obtained at the end of the RFA sessions and 3-7 d after RFA to evaluate the ablative areas and margins. The ablated areas and margins were measured using axial plane images acquired by both imaging techniques, with prior contrast-enhanced MDCT images as the reference. The sensitivity, specificity, and positive and negative predictive values of C-arm CT for detecting insufficient ablative margins (< 5 mm) were calculated. Statistical differences in the ablative areas and margins evaluated with both imaging techniques were compared using a paired *t*-test.

RESULTS: All RFA procedures were technically successful. Of 48 total ablative margins, 19 (39.6%) and 20 (41.6%) margins were found to be insufficient with C-arm CT and MDCT, respectively. Moreover, there were no significant differences between these 2 imaging techniques in the detection of these insufficient ablative margins. The sensitivity, specificity, and positive and negative predictive values for detecting insufficient margins by C-arm CT were 90.0%, 96.4%, 94.7% and 93.1%, respectively. The mean estimated ablative areas calculated from C-arm CT (462.5 ± 202.1 mm^2) and from MDCT (441.2 ± 212.5 mm^2) were not significantly different. The mean ablative margins evaluated by C-arm CT (6.4 ± 2.2 mm) and by MDCT (6.0 ± 2.4 mm) were also not significantly different.

CONCLUSION: The efficacy of intravenous contrast-enhanced C-arm CT in assessing the ablative areas and margins after RFA of liver tumors is nearly equivalent to that of MDCT.

Key words: Radiofrequency ablation; Cone-beam computed tomography; Safety margin; Liver; Neoplasms

Peer reviewers: Sergio Casciaro, PhD, Institute of Clinical Physiology, National Research Council, Campus Universitario Ecotekne, Via Monteroni, 73100 Lecce, Italy; Kazushi Numata, MD, PhD, Associate Professor, Gastroenterological Center, Yokohama City University Medical Center, 4-57 Urafune-cho, Minami-ku, Yokohama, Kanagawa 232-0024, Japan

Iwazawa J, Ohue S, Hashimoto N, Mitani T. Ablation margin assessment of liver tumors with intravenous contrast-enhanced C-arm computed tomography. *World J Radiol* 2012; 4(3): 109-114 Available from: URL: http://www.wjgnet.com/1949-8470/full/v4/i3/109.htm DOI: http://dx.doi.org/10.4329/wjr.v4.i3.109

INTRODUCTION

Radiofrequency ablation (RFA) is an established local therapy for managing malignant liver tumors because of its applicability to minimally invasive treatment. A recent randomized controlled trial demonstrated that RFA for small hepatocellular carcinoma confers a survival benefit comparable to that of surgical resection[1]. In addition, RFA offers patients the potential benefits of safety, reasonable cost, and reduced hospitalization, while resulting in postoperative outcomes comparable to those of surgery[2]. To achieve curative ablation, complete ablation of the tumor with ablative margins of at least 5 mm is required[3]. Failure to obtain these sufficient safety margins is one of the significant prognostic factors affecting local tumor progression[4]. The ablative areas and margins are usually evaluated after RFA therapy with postprocedural contrast-enhanced multidetector computed tomography (MDCT) or magnetic resonance (MR) imaging[3,5]. However, an immediate assessment of therapeutic efficacy using CT or MR imaging can be difficult to accomplish unless the procedure can be performed on the available CT or MR imaging equipment. Otherwise, the patient must be transferred to the nearest imaging scanner, which requires significant preparation time and carries an increased risk of contamination of both the patient and the RFA equipment.

The flat-detector C-arm angiographic system is a relatively new imaging system that generates both conventional angiographic images and multisectional soft tissue images similar to those of CT[6,7]. Moreover, recent developments in C-arm cone-beam CT technology have enabled the prompt acquisition of CT-like images without the need for patient transfer and with a CT dose index lower than that of conventional CT[8,9]. Furthermore, a wider free space than that for a conventional CT scanner is available in the C-arm equipment, and thus, easier and safer RFA procedures would be expected. C-arm CT images are acquired by rotating a flat detector around the patient, and these images provide useful information about tumor location and configuration[10]. The images can also be used to determine the best navigation route for the needle[11] to perform RFA of liver tumors. Due to the low-contrast nature of C-arm CT[12], assessment of the therapeutic efficacy of RFA requires contrast-enhanced C-arm CT images that are commonly acquired by injecting contrast material through a catheter previously placed in the hepatic artery[11]. The intravenous administration of contrast material is a convenient and timesaving technique that is less invasive for the patients. However, the application of intravenously enhanced C-arm CT for assessing the therapeutic efficacy of RFA has not yet been documented.

In this preliminary study, we evaluated the feasibility of intravenously enhanced C-arm CT for the immediate assessment of ablative areas and margins after RFA of malignant liver tumors.

MATERIALS AND METHODS

Study design

We retrospectively reviewed 12 patients (5 men, 7 women; mean age, 69.5 years) who had solitary liver tumors (8 hepatocellular carcinomas and 4 metastatic tumors; size range, 8-20 mm; mean size, 16.3 mm) and who underwent intravenous contrast-enhanced C-arm CT and MDCT after RFA between December 2009 and April 2011. All patients underwent contrast-enhanced MDCT within 56 d (mean, 35.6 d) prior to the RFA session. The diagnosis of the tumor was confirmed from previous imaging findings as well as from elevated levels of serum tumor markers. For evaluating ablative areas and margins, intravenously enhanced C-arm CT and MDCT images were obtained at the end of the RFA sessions and 3-7 d after the sessions. Ablative areas and margins measured with both imaging techniques were compared, with preprocedural MDCT images as the reference.

This study proceeded in accordance with the guidelines of our institutional review board, and written informed consent was obtained from the patients.

Radiofrequency ablation

All RFA procedures were performed with a flat-detector C-arm angiographic system (Innova 3100; GE Healthcare, Waukesha, WI, United States). A 17-gauge radiofrequency electrode (Cool-tip radiofrequency electrode; Radionics, Burlington, MA, United States) with an exposed needle tip of 2 or 3 cm was used depending on the size of the tumor. The needle was inserted using ultrasound (US) guidance in all cases. When the target tumor was poorly defined by the US, C-arm CT was used to assist the needle placement. The ablation was terminated when tissue resistance reached the maximum value or when the ablative duration exceeded 6 min. After the ablation was completed, the temperature of the ablated tissue was measured. When the tissue temperature had not exceeded 60 ℃, additional ablation was performed after needle replacement until the tissue temperature exceeded 60 ℃[13].

C-arm computed tomography

Intravenous contrast-enhanced C-arm CT images were obtained 2 min after injecting a 90-mL bolus of iopamidol (300 mgI/mL; flow rate, 1 mL/s) through the antecubital vein by using a power injector. The image acquisition parameters were as follows: total scanning angle, 200°; acquisition time, 10 s; matrix size, 1500 × 1500; isotropic voxel size, 0.2 mm; and effective field of view (FOV), 18 cm^2. Raw data sets were transferred to an external workstation (Advantage Workstation 4.2; GE Healthcare), where the images were reconstructed with a slice thickness of 3-5 mm on multiple planes. Images were reconstructed within approximately 2.25 min of the end of each scan.

Multidetector computed tomography

Triphasic contrast-enhanced MDCT images were ob-

tained using a 16-MDCT scanner (Somatom Sensation, Siemens Medical Solutions, Forchheim, Germany) with the following scanning parameters: 120 kV; 182 mA; beam collimation, 0.75 mm; helical pitch, 1.15 mm; and rotation table speed, 0.5 s. Helical acquisition for arterial, portal, and venous phase imaging was initiated at 20, 60 and 160 s, respectively, after a threshold level of 100 Hounsfield units (HU) was reached in the abdominal aorta. Images were reconstructed in 5-mm thick transverse sections.

Image analysis

Both contrast-enhanced C-arm CT images and portal-phase MDCT images were viewed on a commercial workstation (eFilm Workstation; Infocom, Tokyo, Japan) by a single observer who had more than 10 years of experience in hepatic vascular intervention and liver imaging. Firstly, the diameters of the ablated regions were measured in 2 orthogonal long and short axes by using axial plane images of each imaging modality. By using an eclipse model, the estimated ablated area was calculated as πab, where a and b are one-half of the long and short axes, respectively. Secondly, the ablative margins of each region were measured in 4 orthogonal directions on the axial plane image by measuring the distance from the nearest hepatic or portal vein, with preprocedural MDCT images as the reference (Figures 1 and 2). The distance measurements were performed manually on the workstation.

Differences in the detection of insufficient ablative margins (< 5 mm), mean estimated ablative areas, and mean ablative margins in C-arm CT and MDCT images were statistically compared using the paired *t*-test. The sensitivity, specificity, positive predictive values (PPVs), and negative predictive values (NPVs) for detecting insufficient ablation margins by C-arm CT were calculated, using MDCT images as the reference.

RESULTS

All RFA procedures were technically successful without major complications in all 12 patients. Two of the twelve patients received C-arm CT assistance during the RF needle placement because the target lesion was located outside the US scan range. Of the 12 patients, 6 received a single ablation, whereas the remaining 6 underwent an additional ablation after adjusting the needle position based on US images. The mean ablation time for single lesions was 8.9 min (range, 6-12 min). The mean therapeutic time from needle insertion to completion of the final image acquisition of C-arm CT was approximately 40 min. For all 12 patients, intravenous contrast-enhanced C-arm CT images were successfully obtained after the procedure. There were no significant differences in detection for the long and short axes of the ablated tissues, mean estimated ablative area, mean ablative margin, and an insufficient safety margin with C-arm CT and with MDCT (Table 1). The sensitivity, specificity, PPV, and NPV for detecting insufficient safety margins with the C-arm CT were 90.0%, 96.4%, 94.7% and 93.1%, respectively. One false positive and 2 false negative findings were recorded on C-arm CT images. The false positive result was attributed to the oblique acquisition of the C-arm CT images, and the 2 false negatives were caused by size reduction of the ablated tissues. Local tumor recurrence was observed in 2 of the 12 study lesions during the follow-up observation periods (mean, 10.1 mo; range 5-18 mo). These 2 recurrent lesions arose from the locations that were equally judged as insufficient ablative margins using both C-arm CT and MDCT.

DISCUSSION

In this study, we found that C-arm CT is nearly equivalent to MDCT in terms of detecting ablative areas and insufficient safety margins directly after RFA procedures. This result could be applied to determine the therapeutic endpoint of RFA and map further treatment strategies. When C-arm CT detects an insufficient ablation margin or a residual lesion, targeted additional ablation would then be promptly applied under C-arm CT assistance. Conversely, when sufficient ablative margins are confirmed on C-arm CT images, additional therapeutic assessments with other imaging modalities may not be required. Another advantage of C-arm CT is its multiplicity in usage. As C-arm CT has comparable ability to MDCT for the detection of hypervascular liver tumors[10,14], operators can obtain pretreatment information for treatment planning, including skin entry point, needle path, and target lesion location, size, and configuration from C-arm CT images immediately prior to the therapy. C-arm CT is also useful during therapy for enabling 3D fluoroscopic guidance for insertion of the radiofrequency electrode to the target tumor, which provides operators with a safer and easier approach to the target[11]. Furthermore, as suggested by our results, the treatment efficacy of RFA can be evaluated with C-arm CT acquired immediately after the therapy. Thus, C-arm CT has various potential applications throughout the RFA procedures.

Although there were no significant differences in detection for the long and short axes of the ablated tissues, the mean estimated ablative area, and mean ablative margin with C-arm CT and with MDCT, all of the parameters were slightly overestimated by C-arm CT relative to MDCT. This result might be attributable to differences in the time points at which the image acquisitions occurred. During the ablation process, the tissue is destroyed by coagulative necrosis. The resultant ablated region then gradually decreases in size through tissue shrinkage[15]. Therefore, a more accurate comparison would have been expected if C-arm CT and MDCT images were obtained on the same day.

Kim *et al*[16] reported that a 5-mm safety margin was achieved in only 2.7% of patients, and vessel-induced indentation of the ablation zone contributed to the thinnest ablative margins observed in 47.3% in RFA of

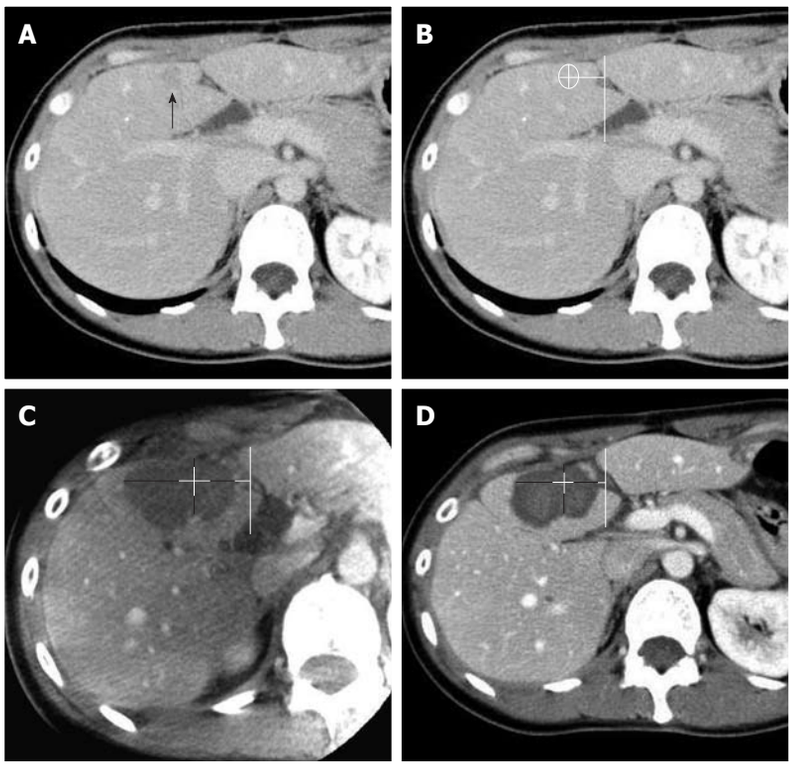

Figure 1 A 43-year-old woman with a 13-mm hepatocellular carcinoma in hepatic segment Ⅳ. A: A venous-phase image from contrast-enhanced multidetector computed tomography (MDCT) prior to treatment shows a hypoattenuated tumor in hepatic segment Ⅳ (arrow); B: A venous-phase MDCT image in which the tumor size has been measured in vertical and horizontal directions and the tumor location has been determined by the distance from the left portal vein; C: An intravenous contrast-enhanced C-arm computed tomography image obtained just after radiofrequency ablation (RFA) shows sufficient ablative margins in all 4 directions (ventral margin, 1.8 mm; dorsal margin, 8.8 mm; right lateral margin, 20.5 mm, left lateral margin, 10.3 mm) even though the ventral ablative margin is less than 5 mm due to the adjacent liver border; D: A portal-phase image from contrast-enhanced MDCT obtained 7 d after the RFA procedure shows an almost identical configuration with ablative margins (ventral margin, 2.0 mm; dorsal margin, 8.0 mm; right lateral margin, 17.0 mm; left lateral margin, 10.0 mm) comparable to those depicted in the C-arm CT image.

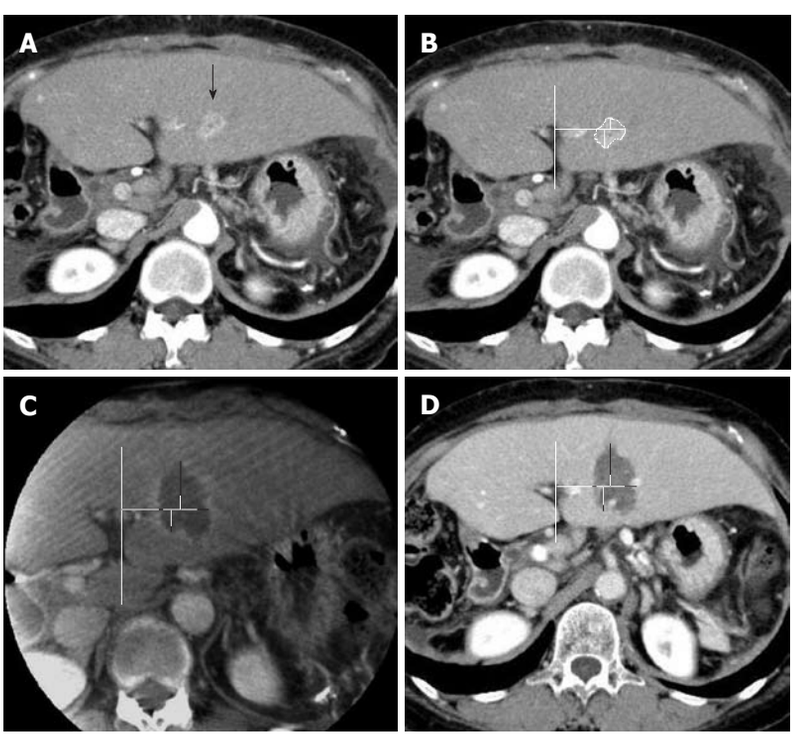

Figure 2 A 59-year-old woman with a 15-mm hepatocellular carcinoma in hepatic segment Ⅲ. A: An arterial-phase image from contrast-enhanced multidetector computed tomography (MDCT) prior to treatment shows a well-enhanced tumor in hepatic segment Ⅲ (arrow); B: An arterial-phase MDCT image in which the tumor size has been measured in the vertical and horizontal directions and the tumor location has been determined by the distance from the left portal vein; C: An intravenous contrast-enhanced C-arm computed tomography (CT) image obtained just after radiofrequency ablation (RFA) reveals insufficient ablative margins in the right lateral (1.1 mm) and dorsal (1.9 mm) directions. Indentations caused by the left hepatic vein and the portal vein adjacent to the tumor might disrupt sufficient ablation. The ventral (11.3 mm) and left lateral (5.4 mm) ablative margins appear sufficient; D: A portal-phase image from contrast-enhanced MDCT obtained 7 d after RFA shows an almost identical configuration with comparable ablative margins (ventral margin, 11.0 mm; dorsal margin, 3.0 mm; right lateral margin, 2.0 mm; left lateral margin, 6.0 mm) to those evaluated on C-arm CT image.

Table 1 Comparison of intravenous contrast-enhanced C-arm computed tomography and multidetector computed tomography for the assessment of ablative areas and margins in radiofrequency ablation of liver tumors (mean ± SD)

	C-arm computed tomography	Multidetector computed tomography	*P* value
Mean long axis (mm)	28.1 ± 8.1	27.3 ± 8.1	0.134
Mean short axis (mm)	19.9 ± 4.8	19.3 ± 5.1	0.161
Mean estimated ablative area (mm^2)	462.5 ± 202.1	441.2 ± 212.5	0.206
Mean ablative margin (mm)	6.4 ± 2.2	6.0 ± 2.4	0.159
Insufficient safety margin detection (%)	39.6 (19/48)	41.6 (20/48)	0.569

patients with hepatocellular carcinoma whose tumor diameters were 2-5 cm. In this study, a 5-mm safety margin was achieved in 60.4% (29/48) of patients with C-arm CT and 58.3% (28/48) of patients with MDCT. Tumor size in this study (mean, 1.6 cm; range 0.8-2.0 cm) was relatively small, which might have affected this higher rate of achieving sufficient ablative margins in our study. Vessel-related indentation for insufficient ablative margin was observed in 37.5% (18/48) of subjects for both C-arm CT and MDCT in this study, as shown in Figure 2.

C-arm CT intrinsically has potential disadvantages in the assessment of ablative areas and the safety margins in terms of contrast resolution, image quality, and FOV. Although C-arm CT has a comparable spatial resolution to MDCT[17], its contrast resolutions are expected to be only 50 HU for abdominal application[6]. The usage of contrast material for C-arm CT acquisition may overcome this limitation; however, imaging information for liver tumors using intravenously enhanced C-arm CT has not yet been quantified. C-arm CT has modality-specific artifacts that occasionally can negatively affect the image quality. For example, transient movement during image acquisition spoils the entire image quality in C-arm CT, whereas only the affected slice image is spoiled in MDCT. Recently, respiratory motion artifacts in C-arm CT have been successfully corrected in a phantom model[18]. Thus, patients who have difficulty holding their breath or have tumors in the left hepatic lobe susceptible to the heartbeat could be accurately examined by C-arm CT in the near future. In the current study, although some movement artifacts affected image quality, the detection of ablative areas and margins remained acceptable. The effective FOV available with the flat-detector C-arm system used in this study was only 18 mm^2. This might be acceptable for planning and assessing the RFA for a single lesion; however, it becomes problematic when visualization of 2 or more hepatic lesions located throughout the entire liver is required. However, these shortcomings can be overcome using a wider detector with an increased scanning range.

This study has several limitations. Firstly, we compared single-phase contrast-enhanced C-arm CT with triple-phase contrast-enhanced MDCT. Due to the relatively long reconstruction time for the current version of C-arm CT, acquiring triphasic contrast-enhanced C-arm CT images was unachievable. We therefore compared contrast-enhanced C-arm CT images with the portal-phase images of MDCT. Secondly, the ablated area and margins were measured manually on the workstation by a single observer. The measurements may have contained certain errors. Thirdly, the amount of iopamidol administered for a single acquisition of C-arm CT was 90 mL in this study. Repeated acquisition of contrast-enhanced C-arm CT is limited due to increased risk of renal disturbance. Fourthly, we evaluated ablative areas and margins only on an axial plane image. In clinical settings, 3-dimensional images are required for assessing the safety margins in every direction.

In this preliminary study, the efficacy of intravenous contrast-enhanced C-arm CT for assessing ablative areas and safety margins immediately after the RFA of liver tumors is nearly equivalent to that of MDCT performed 3-7 d after RFA.

COMMENTS

Background

Radiofrequency ablation is an established local therapy for managing malignant liver tumors. Immediate assessment of ablative margins is necessary for prompt decisions regarding further treatment. The ablative margins are usually evaluated using postprocedural contrast-enhanced computed tomography (CT). However, immediate assessment of ablative margins can often be difficult, unless the procedure can be performed using the available CT imaging equipment.

Research frontiers

Recent developments in C-arm cone-beam CT technology have enabled the prompt acquisition of soft-tissue images without the need for patient transfer, and the CT dose index for C-arm CT is expected to be lower than that for conventional CT. C-arm equipment also includes a wider working space than that available in conventional CT scanners. However, the adequacy of the quality of images obtained using C-arm CT during liver tumor imaging is still controversial because of the low contrast obtained in C-arm CT.

Innovations and breakthroughs

The paper found that intravenous contrast-enhanced C-arm CT is nearly equivalent to multidetector CT in terms of detecting ablative areas and insufficient safety margins directly after radiofrequency ablation of liver tumors.

Applications

Prompt and sufficient image acquisition during C-arm CT performed for assessing the therapeutic efficacy of liver tumor ablation during the procedure provides useful information regarding further treatment strategies. When an insufficient ablative margin is detected in C-arm CT, targeted additional ablation would then be promptly performed. Conversely, when sufficient ablative margins are confirmed, no additional therapeutic assessments with other imaging modalities may be required. These advantages of C-arm CT may improve the overall therapeutic efficacy of liver tumor ablation.

Terminology

The term "C-arm CT" refers to the images provided by the C-arm flat-panel cone-beam system. The digital flat-panel detector rotates around the patient to generate volumetric images similar to those obtained with conventional CT. The C-arm system also provides projection radiography, fluoroscopy, and digital subtraction angiography in a single-patient setup in the interventional suite. Such facilities allow the operators to perform intraprocedural imaging without the need for patient transfer.

Peer review

The paper addresses an important issue related to safety margin evaluation in liver radiofrequency ablation and compares C-arm CT and multidetector CT imaging in this regard. The paper is well written and well presented and correctly reports study limitations and future perspectives.

REFERENCES

1 **Chen MS**, Li JQ, Zheng Y, Guo RP, Liang HH, Zhang YQ, Lin XJ, Lau WY. A prospective randomized trial comparing percutaneous local ablative therapy and partial hepatectomy for small hepatocellular carcinoma. *Ann Surg* 2006; **243**: 321-328

2 **Minami Y**, Kudo M. Radiofrequency ablation of hepatocellular carcinoma: Current status. *World J Radiol* 2010; **2**: 417-424

3 **Mori K**, Fukuda K, Asaoka H, Ueda T, Kunimatsu A, Okamoto Y, Nasu K, Fukunaga K, Morishita Y, Minami M. Radiofrequency ablation of the liver: determination of ablative margin at MR imaging with impaired clearance of ferucarbotran--feasibility study. *Radiology* 2009; **251**: 557-565

4 **Kim YS**, Rhim H, Cho OK, Koh BH, Kim Y. Intrahepatic recurrence after percutaneous radiofrequency ablation of hepatocellular

carcinoma: analysis of the pattern and risk factors. *Eur J Radiol* 2006; **59**: 432-441

5 **Kim KW**, Lee JM, Klotz E, Kim SJ, Kim SH, Kim JY, Han JK, Choi BI. Safety margin assessment after radiofrequency ablation of the liver using registration of preprocedure and postprocedure CT images. *AJR Am J Roentgenol* 2011; **196**: W565-W572

6 **Wallace MJ**, Kuo MD, Glaiberman C, Binkert CA, Orth RC, Soulez G. Three-dimensional C-arm cone-beam CT: applications in the interventional suite. *J Vasc Interv Radiol* 2008; **19**: 799-813

7 **Orth RC**, Wallace MJ, Kuo MD. C-arm cone-beam CT: general principles and technical considerations for use in interventional radiology. *J Vasc Interv Radiol* 2008; **19**: 814-820

8 **Kim S**, Yoshizumi TT, Toncheva G, Yoo S, Yin FF. Comparison of radiation doses between cone beam CT and multi detector CT: TLD measurements. *Radiat Prot Dosimetry* 2008; **132**: 339-345

9 **Hirota S**, Nakao N, Yamamoto S, Kobayashi K, Maeda H, Ishikura R, Miura K, Sakamoto K, Ueda K, Baba R. Cone-beam CT with flat-panel-detector digital angiography system: early experience in abdominal interventional procedures. *Cardiovasc Intervent Radiol* 2006; **29**: 1034-1038

10 **Iwazawa J**, Ohue S, Hashimoto N, Abe H, Hamuro M, Mitani T. Detection of hepatocellular carcinoma: comparison of angiographic C-arm CT and MDCT. *AJR Am J Roentgenol* 2010; **195**: 882-887

11 **Morimoto M**, Numata K, Kondo M, Nozaki A, Hamaguchi S, Takebayashi S, Tanaka K. C-arm cone beam CT for hepatic tumor ablation under real-time 3D imaging. *AJR Am J Roentgenol* 2010; **194**: W452-W454

12 **Linsenmaier U**, Rock C, Euler E, Wirth S, Brandl R, Kotsianos D, Mutschler W, Pfeifer KJ. Three-dimensional CT with a modified C-arm image intensifier: feasibility. *Radiology* 2002; **224**: 286-292

13 **McGahan JP**, Brock JM, Tesluk H, Gu WZ, Schneider P, Browning PD. Hepatic ablation with use of radio-frequency electrocautery in the animal model. *J Vasc Interv Radiol* 1992; **3**: 291-297

14 **Meyer BC**, Frericks BB, Voges M, Borchert M, Martus P, Justiz J, Wolf KJ, Wacker FK. Visualization of hypervascular liver lesions During TACE: comparison of angiographic C-arm CT and MDCT. *AJR Am J Roentgenol* 2008; **190**: W263-W269

15 **Goldberg SN**, Gazelle GS, Halpern EF, Rittman WJ, Mueller PR, Rosenthal DI. Radiofrequency tissue ablation: importance of local temperature along the electrode tip exposure in determining lesion shape and size. *Acad Radiol* 1996; **3**: 212-218

16 **Kim YS**, Lee WJ, Rhim H, Lim HK, Choi D, Lee JY. The minimal ablative margin of radiofrequency ablation of hepatocellular carcinoma (& gt; 2 and & lt; 5 cm) needed to prevent local tumor progression: 3D quantitative assessment using CT image fusion. *AJR Am J Roentgenol* 2010; **195**: 758-765

17 **Watanabe H**, Honda E, Tetsumura A, Kurabayashi T. A comparative study for spatial resolution and subjective image characteristics of a multi-slice CT and a cone-beam CT for dental use. *Eur J Radiol* 2011; **77**: 397-402

18 **Zhang Q**, Hu YC, Liu F, Goodman K, Rosenzweig KE, Mageras GS. Correction of motion artifacts in cone-beam CT using a patient-specific respiratory motion model. *Med Phys* 2010; **37**: 2901-2909

S- Editor Cheng JX **L- Editor** Logan S **E- Editor** Xiong L

World Journal of Radiology

Online Submissions: http://www.wjgnet.com/1949-8470office
wjr@wjgnet.com
doi:10.4329/wjr.v4.i3.115

World J Radiol 2012 March 28; 4(3): 115-120
ISSN 1949-8470 (online)

CASE REPORT

Hepatic artery pseudoaneurysm after endoscopic biliary stenting for bile duct cancer

Manabu Watanabe, Kazue Shiozawa, Takahiko Mimura, Ken Ito, Itaru Kamata, Yui Kishimoto, Koichi Momiyama, Yoshinori Igarashi, Yasukiyo Sumino

Manabu Watanabe, Kazue Shiozawa, Takahiko Mimura, Ken Ito, Itaru Kamata, Yui Kishimoto, Koichi Momiyama, Yoshinori Igarashi, Yasukiyo Sumino, Division of Gastroenterology and Hepatology, Department of Internal Medicine, Toho University Medical Center, Omori Hospital, 6-11-1, Omorinishi, Ota-ku, Tokyo 143-8541, Japan

Author contributions: Mimura T, Ito K, Kamata I, Kishimot Y, Momiyama K were responsible for patient care; Watanabe M, Igarashi Y, Sumino Y designed the research; Shiozawa K assisted with review of the literature; Watanabe M wrote the paper.

Correspondence to: **Manabu Watanabe, MD, PhD,** Division of Gastroenterology and Hepatology, Department of Internal Medicine, Toho University Medical Center, Omori Hospital 6-11-1, Omorinishi, Ota-ku, Tokyo 143-8541, Japan. manabu62@med.toho-u.ac.jp

Telephone: +81-3-37624151 Fax: +81-3-37638542

Received: August 28, 2011 Revised: November 14, 2011
Accepted: November 21, 2011
Published online: March 28, 2012

Abstract

We report a case of a pseudoaneurysm of the right hepatic artery observed 9 mo after the endoscopic placement of a Wallstent, for bile duct stenosis, which was treated with transcatheter arterial embolization. The patient presented with obstructive jaundice and was diagnosed with inoperable common bile duct cancer. A plastic stent was inserted endoscopically to drain the bile, and chemotherapy was initiated. Abdominal pain and jaundice appeared approximately 6 mo after the beginning of chemotherapy. A diagnosis of stent occlusion and cholangitis was made, and the plastic stent was removed and substituted with a self-expandable metallic stent (SEMS) endoscopically. Nine months after SEMS insertion, contrast-enhanced computed tomography showed a pseudoaneurysm of the right hepatic artery protruding into the common bile duct lumen and in contact with the SEMS. The shape and size of the pseudoaneurysm and diameter of its neck was determined by contrast-enhanced ultrasonography using Sonazoid. A micro-catheter was led into the pseudoaneurysm in the right hepatic artery, GDC™ Detachable Coils were placed, and IDC™ Detachable Coils were then placed in the right hepatic artery on the distal and proximal sides of the pseudoaneurysm using the isolation method. There have been a few reports on pseudoaneurysm associated with stent placement in the biliary tract employing percutaneous transhepatic procedures, however, reports of pseudoaneurysms associated with endoscopic SEMS placement are very rare.

Key words: Pseudoaneurysm; Self-expandable metallic stents; Sonazoid; Transcatheter arterial embolization; Wallstent

Peer reviewers: Takao Hiraki, MD, Assistant Professor, Department of Radiology, Okayama University Medical School, 3-5-1 Shikatacho, Okayama 700-0861, Japan; Hadi Rokni Yazdi, MD, Associate Professor, Department of radiology, Central Radiology, Imam Khomeini Hospital, Tehran University of Medical Sciences, Keshavarz Blvd, Tehran, 1419733141, Iran

Watanabe M, Shiozawa K, Mimura T, Ito K, Kamata I, Kishimoto Y, Momiyama K, Igarashi Y, Sumino Y. Hepatic artery pseudoaneurysm after endoscopic biliary stenting for bile duct cancer. *World J Radiol* 2012; 4(3): 115-120 Available from: URL: http://www.wjgnet.com/1949-8470/full/v4/i3/115.htm DOI: http://dx.doi.org/10.4329/wjr.v4.i3.115

INTRODUCTION

Recently, self-expandable metallic stents (SEMS) have begun to be used widely for internal drainage of malignant biliary tract stenosis, and are contributing to improvements in patients' quality of life (QOL) as they are expected to prolong the period of patency depending on

the stent diameter. SEMS placement is considered safe due to the development and improvement of various devices, however, serious complications such as hemorrhage as well as re-occlusion and inflammation are occasionally observed and pose difficulties in management. In this study, we placed an SEMS endoscopically in a patient with obstructive jaundice due to inoperable middle common bile duct cancer. A pseudoaneurysm was confirmed in the right hepatic artery approximately 9 mo later, and was treated with transcatheter arterial embolization (TAE) prophylactically. There have been a few reports of pseudoaneurysm associated with stent placement in the biliary tract employing percutaneous transhepatic procedures, however, reports of pseudoaneurysms associated with endoscopic SEMS placement are very rare. Such a case is reported here, with a review of the literature.

CASE REPORT

A 70-year-old man, who had been generally healthy, noted malaise, yellowing of the bulbar conjunctiva, and brown urine, and consulted a local clinic. He was diagnosed with obstructive jaundice and was admitted to our hospital. Blood chemistry tests showed that ALT was 202 IU/L (normal < 31 IU/L), ALP was 3023 IU/L (normal < 314 IU/L), T-bilirubin was 16.1 mg/dL (normal <1.0 mg/dL), D-bilirubin was 10.9 g/dL (normal < 0.3 mg/dL), C reactive protein (CRP) was 5.9 mg/dL (normal < 0.2 mg/dL), and WBC was 16300/μL (normal < 9000 μL), indicating jaundice, increases in hepatic and biliary tract enzymes and inflammatory reactions. Abdominal ultrasonography (US) showed a hypoechoic solid mass in the middle of the common bile duct with dilation of the intrahepatic duct and enlargement of the gallbladder. Abdominal CT confirmed findings similar to those on US and showed swelling of lymph nodes around the mass and in the abdominal cavity. Narrowing over about 20 mm of the common bile duct was noted on endoscopic retrograde cholangiopancreatography (ERCP), and a diagnosis of adenocarcinoma was made following biopsy. On the basis of these findings, a diagnosis of inoperable common bile duct cancer was made, and a plastic stent (10Fr× 40 mm, Zimmon Biliary Stent, Wilson-Cook Medical) was inserted endoscopically to drain the bile, and chemotherapy (TS-1: oral 5-fluorouracil derivative) was initiated. Abdominal pain and jaundice appeared approximately 6 mo after the beginning of chemotherapy. A diagnosis of stent occlusion and cholangitis was made, and the plastic stent was removed and substituted for an SEMS (80 × 10 mm, WallFlex® Biliary RX uncovered Stent, Boston Scientific) endoscopically. CT images obtained 5 mo later showed no abnormal findings in the right hepatic artery (Figure 1). After 9 mo, abdominal pain and jaundice recurred, and the patient was hospitalized again. T-bilirubin was 3.7 mg/dL, CRP was increased at 9.4 mg/dL, and CT and ERCP showed dilation of the intrahepatic bile duct, indicating cholangitis, but, at this point, a small pseudoaneurysm of the right hepatic artery,

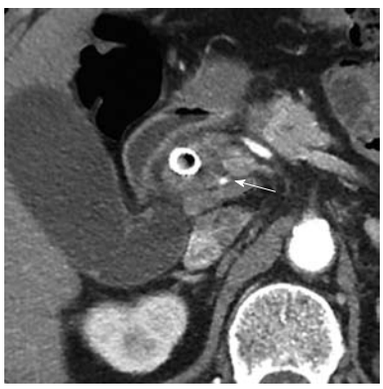

Figure 1 Computed tomography image obtained 5 mo after self-expandable metallic stent insertion showed no abnormal findings of the right hepatic artery (arrow).

Figure 2 Computed tomography showed a small pseudoaneurysm of the right hepatic artery, measuring 9 × 6 mm, protruding into the common bile duct lumen (arrow) 9 mo after self-expandable metallic stent insertion.

measuring 9 × 6 mm, protruding into the common bile duct lumen and in contact with the SEMS was overlooked (Figure 2). On the 2nd hospital day, an endoscopic nasobiliary drainage (ENBD) (7.2Fr. pigtail, Hanako Medical Co., Tokyo) and a plastic stent (7Fr × 100 mm, Zimmon Biliary Stent, Wilson-Cook Medical) were placed into the SEMS (stent-in-stent placement). On CT performed on the 6th hospital day, the pseudoaneurysm had enlarged to 21 × 11 mm (Figure 3). US performed on the same day showed marked dilation of the common bile duct to a diameter of 24 mm and consequent extrinsic compression of the portal vein. The SEMS was displaced toward the liver, and hypoechoic solid components filling the space between the SEMS and bile duct and a pseudoaneurysm showing cystic growth in the lumen of the bile duct were observed. Only the apex of the pseudoaneurysm was in contact with the SEMS (Figure 4). The pseudoaneurysm and hypoechoic solid components filling the dilated bile duct were examined on contrast-enhanced ultrasonography (CEUS) using Sonazoid, and the maximum diameter and neck diameter of the pseudoaneurysm were found to be 23 mm and about 14 mm, respectively. However, there were no Sonazoid bubbles detected in the bile duct other than the pseudoaneurysm, and the hypoechoic solid

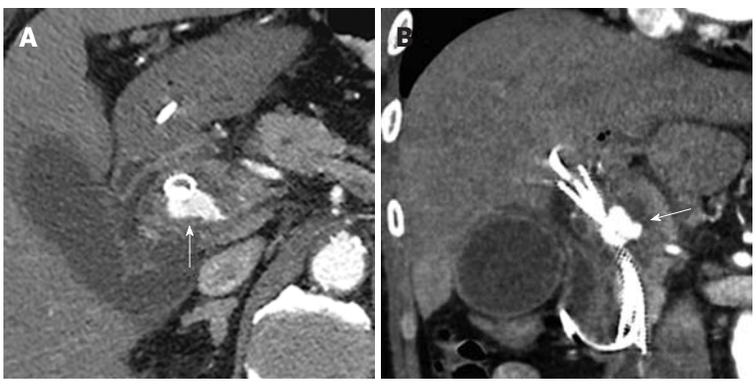

Figure 3 On the 2nd hospital day, an endoscopic nasobiliary drainage and a plastic stent were placed into the self-expandable metallic stent. On the 6th hospital day, axial (A) and coronal (B) plane arterial phase computed tomography showed enlargement of the pseudoaneurysm (arrow).

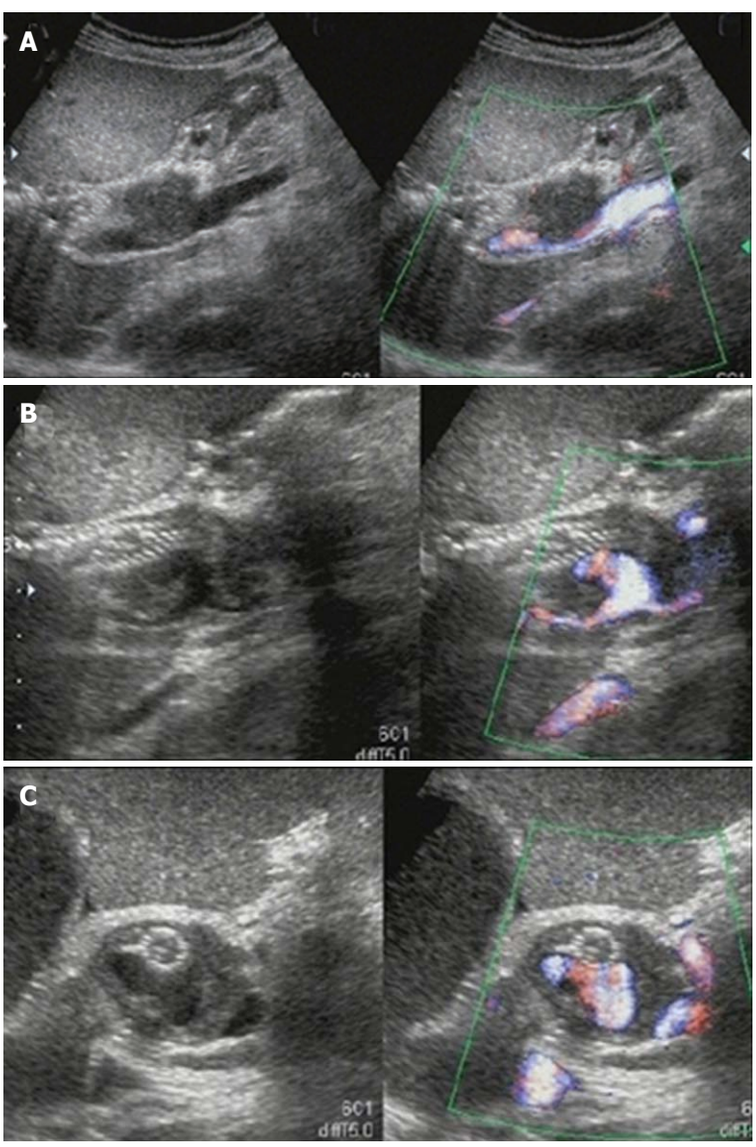

Figure 4 Color Doppler ultrasonography on the 6th hospital day. A: Ultrasonography showed marked dilation of the common bile duct to a diameter of 24 mm and consequent extrinsic compression of the portal vein; B:The self-expandable metallic stent (SEMS) was displaced toward the liver, and hypoechoic solid components filling the space between the SEMS and bile duct and a pseudoaneurysm showing cystic growth in the lumen of the bile duct was observed; C: Only the apex of the pseudoaneurysm was in contact with the SEMS.

components filling the bile duct were judged to be debris (Figure 5). While no hemorrhage from the bile duct was noted during the disease course, the pseudoaneurysm tended to enlarge, and TAE was performed on the 12th hospital day. On angiography, the left and right hepatic arteries were found to arise from the superior mesenteric artery, and the pseudoaneurysm was confirmed to be located in the right hepatic artery, as suggested by computed tomography (CT). The aneurysm was located upstream of the common bile duct cancer at the upper third of the SEMS and was separated from the ends of the stent. A micro-catheter was led into the pseudoaneurysm in the right hepatic artery, two 3D shape coils, two 2D shape (GDC™ Detachable Coils, Boston Scientific) were placed, and seven coils (IDC™Detachable Coils, Boston Scientific) were then placed in the right hepatic artery

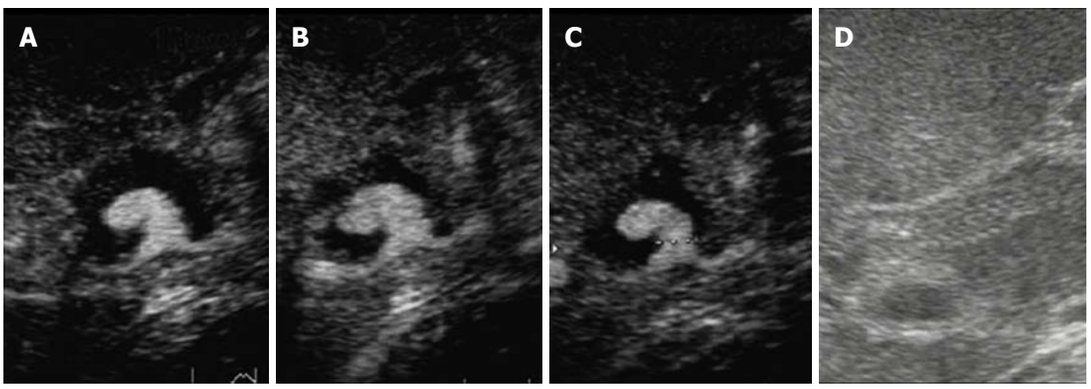

Figure 5 The pseudoaneurysm and hypoechoic solid components filling the dilated bile duct were examined on contrast-enhanced ultrasonography. A-C: Images obtained at 15 s (A), 55 s (B) and 127 s (C) after injection of Sonazoid (0.5 mL) *via* a left cubital venous line showed no Sonazoid bubbles in the common bile duct other than in the pseudoaneurysm; D: Monitor B-mode ultrasonography image.

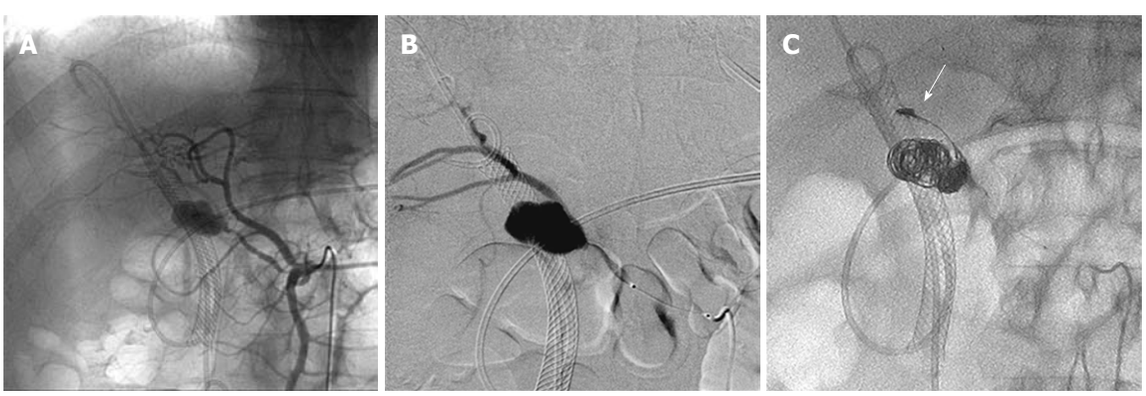

Figure 6 Transcatheter arterial embolization performed on the 12th hospital day. A, B: On angiography, the left and right hepatic arteries were found to arise from the superior mesenteric artery, and the pseudoaneurysm was confirmed to be located in the right hepatic artery; C: One IDC coil was placed in the right hepatic artery on the distal side of the pseudoaneurysm (arrow) after the pseudoaneurysm was framed using several types of coils. Seven coils were placed in the right hepatic artery on the distal and proximal sides of the pseudoaneurysm using the isolation method.

on the distal and proximal sides of the pseudoaneurysm using the isolation method, and the absence of contrast medium influx into the pseudoaneurysm was confirmed (Figure 6). There was no sign of partial hepatic infarction after the procedure on lab data and images. Since no blood flow signal of the pseudoaneurysm was noted on subsequent Doppler US, the ENBD was removed, and the patient was discharged on the 20th hospital day. Chemotherapy has continued to the present.

DISCUSSION

The incidence of serious complications associated with SEMS placement in the bile duct has been reported to be 7%-24%[1,2], and cholangitis, pancreatitis, acute cholecystitis, liver abscess, common bile duct perforation, duodenal perforation, and hemobilia are frequent complications. These complications occur relatively early after the placement of an SEMS, are caused by the procedure of stent placement and re-occlusion due to sludge, and are often resolved by conservative treatment. However, hemobilia occasionally leads to a serious outcome. Generally, hemobilia associated with SEMS placement is considered to be caused by damage to the artery or liver parenchyma due to percutaneous transhepatic puncture prior to SEMS placement or vascularization due to infection. Green *et al*[3] reported in a review of 222 recent cases of hemobilia, that the hemorrhage was caused by medical procedures involving the hepatobiliary system such as percutaneous transhepatic biliary drainage in 147. Moreover, pseudoaneurysms were reported to have been noted in 1.7%-16.9% of cases with hemobilia associated with surgical procedures of the hepatobiliary system[4,5].

To date, there have been a few reports of pseudoaneurysm caused by stents including plastic stents rather than by complications of endoscopic or percutaneous transhepatic procedures, however, those caused by SEMS are very rare[6,7]. Monroe *et al*[6] noted a pseudoaneurysm of the pancreaticoduodenal artery 3 wk after the endoscopic placement of an SEMS, and reported that it was caused by necrosis of the arterial wall due to compression by the SEMS. Rai *et al*[7] reported a case that developed obstructive jaundice 6 mo after percutaneous transhepatic placement of an SEMS, and underwent endoscopic placement of a plastic stent in the SEMS for bile drainage. The stent re-occluded after several months, and,

when the plastic stent alone was removed, a pseudoaneurysm of the right hepatic artery ruptured. They concluded that inflammation around the bile duct and adhesion between the SEMS and hepatic artery contributed to the formation of the right hepatic artery pseudoaneurysm.

In our patient, a plastic stent was placed for obstructive jaundice due to inoperable middle common bile duct cancer, and was replaced with an SEMS endoscopically due to the recurrence of jaundice after 6 mo. CT performed the next day showed no abnormal findings in the right hepatic artery, but CT performed 9 mo after stent re-occlusion first disclosed a pseudoaneurysm in the right hepatic artery. On US and CT, the pseudoaneurysm was about 20 mm in diameter, protruded into the markedly dilated lumen of the common bile duct, and was displaced with only its apex being in contact with the external wall of the SEMS. In addition, US suggested the presence of hypoechoic solid components in the space between the external wall of the SEMS and common bile duct, apparently filling the pseudoaneurysm. However, on CEUS, no Sonazoid bubbles were noted in the hypoechoic area around the pseudoaneurysm, thus, the solid components were judged to be sludge or debris rather than tumor invasion. Moreover, the pseudoaneurysm was located near the center of the SEMS and was distant from its ends, suggesting that the possibility of its formation due to trauma or compression of the arterial wall by the metal at the tip of the SEMS was low. From a review of the disease course, the pseudoaneurysm in the right hepatic artery in our patient was unlikely to have been caused by placement of the plastic stent or SEMS or invasion of the primary cancer to the hepatic artery. Also, no pancreatitis associated with the endoscopic procedure or stent placement was noted, excluding pancreatitis as a cause of pseudoaneurysm formation. Therefore, in our patient, the pseudoaneurysm was considered to have developed due to the promotion of erosion of the hepatic artery wall in contact with the common bile duct by the concurrence of factors including marked dilation of the common bile duct due to the accumulation of sludge and debris and the spread of inflammation to surrounding tissues from recurring cholangitis associated with obstructive jaundice. This etiology of pseudoaneurysms resembles that reported by Monroe *et al*[6], however, there has been no report of a hepatic artery pseudoaneurysm in a patient undergoing endoscopic placement of an SEMS.

More than 60% of unruptured pseudoaneurysms of the hepatic artery are either asymptomatic and detected incidentally or are symptomatic but present nonspecific findings[8,9]. Of ruptured pseudoaneurysms, 10% are asymptomatic and symptoms such as hemobilia, hematemesis, hematochezia, and abdominal pain are noted in 64%, 30%, 14% and 20%, respectively[10]. The possibility of hepatic artery pseudoaneurysm rupture is 21%-80%[11-14], and the mortality rate due to their rupture is high at 21-43%[13,15], thus, appropriate imaging diagnosis and treatment before rupture are desired.

Due to the recent development of imaging modalities, high-performance ultrasound devices, multi-detector row CT (MDCT), and magnetic resonance angiography have become available for the diagnosis of pseudoaneurysms[15-17]. Kim *et al*[16] compared the usefulness of MDCT and Doppler US for the early detection of hepatic artery pseudoaneurysms, which is a complication of liver transplantation from a living donor, and reported MDCT as more effective, probably because US is affected by gas in the digestive tract and the examiner's skill. CEUS, on the other hand, is advantageous in that it is free of radiation exposure or iodine allergy and can also be used in patients with renal dysfunction. The use of CEUS in patients with hepatic artery pseudoaneurysm has not been reported. However, with the use of contrast media such as Sonazoid, its diagnostic utility for hepatic artery pseudoaneurysms may not only be improved, but may also contribute to treatment planning by allowing delineation of the morphology of the lesion, measurement of its neck, determination of the presence or absence of mural thrombi, and detailed and real-time evaluation of the environment around the lesion. According to the report by Green *et al*[3] concerning treatments for hemobilia including that due to pseudoaneurysms, 43% were treated conservatively, 36% by TAE, and 20% surgically, and the rate of surgical treatment appears to be decreasing due to the development of interventional radiology. We also treated our patient with TAE. Embolization can be performed either by covered-stent insertion[18,19] or by simultaneous embolization of both the proximal and distal sides of the pseudoaneurysm[20]. In our patient, because of the width of the neck with a diameter of 14 mm and the mural structure of the pseudoaneurysm, consisting only of a delicate fibrous capsule[18], the internal wall of the aneurysm was framed first using a 3D shape coil, and then a 2D shape coil, a conventional platinum coil, was placed so that it would entwine with the 3D coil to prevent escape of the 2D coil out of the pseudoaneurysm. Thereafter, seven IDC coils were placed in the right hepatic artery on the distal and proximal sides of the pseudoaneurysm, and the procedure was completed by confirming the absence of blood flow in the pseudoaneurysm. It was very important for the safe execution of the procedure that the responsible artery could be identified as a branch of the hepatic artery that arose from the SMA by CT, and that the shape and size of the pseudoaneurysm and diameter of its neck could be determined by CEUS before TAE. The success rate of TAE in controlling hemobilia has been reported to be 80%-100%[3], and the mortality rate due to TAE for pseudoaneurysm of the hepatic artery has been reported to be 25% lower than that due to surgery[10]. Therefore, surgery should be selected for large pseudoaneurysms and patients in whom TAE has been unsuccessful or is contraindicated.

In conclusion, in our patient, prophylactic TAE was performed for a hepatic artery pseudoaneurysm without hemobilia. In addition, CEUS was very useful for delineation of the pseudoaneurysm on examination before

TAE. A lethal pseudoaneurysm or hemobilia may occur during long-term placement of an SEMS in the bile duct. While an SEMS reduces the incidence of jaundice and cholangitis, it may cause specific refractory complications that have not been evaluated sufficiently. Also, if a stent is placed over a long period, many problems including biocompatibility of the stent material and structure remain to be evaluated. The accumulation of cases based on long-term follow-up is necessary.

REFERENCES

1 **Rossi P**, Bezzi M, Salvatori FM, Maccioni F, Porcaro ML. Recurrent benign biliary strictures: management with self-expanding metallic stents. *Radiology* 1990; **175**: 661-665
2 **Tesdal IK,** Jaschke W, Duber C, Werhand J, Klose KJ. Biliary stenting: self-expandable and balloon-expandable stent. Early and late results. In: Liermann DD, editor. Stents-State of the art and future developments. Canada: Polyscience Publications Inc., 1995: 190-195
3 **Green MH**, Duell RM, Johnson CD, Jamieson NV. Haemobilia. *Br J Surg* 2001; **88**: 773-786
4 **Sarr MG**, Kaufman SL, Zuidema GD, Cameron JL. Management of hemobilia associated with transhepatic internal biliary drainage catheters. *Surgery* 1984; **95**: 603-607
5 **Hoevels J**, Nilsson U. Intrahepatic vascular lesions following nonsurgical percutaneous transhepatic bile duct intubation. *Gastrointest Radiol* 1980; **5**: 127-135
6 **Monroe PS,** Deeter WT, Rizk P. Delayed hemobilia secondary to expandable metal stent. *Gastrointest Endosc* 1993; **39:** 190-191
7 **Rai R**, Rose J, Manas D. Potentially fatal haemobilia due to inappropriate use of an expanding biliary stent. *World J Gastroenterol* 2003; **9**: 2377-2378
8 **Finley DS**, Hinojosa MW, Paya M, Imagawa DK. Hepatic artery pseudoaneurysm: a report of seven cases and a review of the literature. *Surg Today* 2005; **35**: 543-547
9 **Akatsu T**, Hayashi S, Egawa T, Doi M, Nagashima A, Kitano M, Yamane T, Yoshii H, Kitajima M. Hepatic artery pseudoaneurysm associated with cholecystitis that ruptured into the gallbladder. *J Gastroenterol* 2004; **39**: 900-903
10 **Tessier DJ**, Fowl RJ, Stone WM, McKusick MA, Abbas MA, Sarr MG, Nagorney DM, Cherry KJ, Gloviczki P. Iatrogenic hepatic artery pseudoaneurysms: an uncommon complication after hepatic, biliary, and pancreatic procedures. *Ann Vasc Surg* 2003; **17**: 663-669
11 **Reber PU,** Baer HU, Patel AG, Wildi S, Triller J, Büchler MW. **Superselective microcoil embolization: treatment of** choice in high-risk patients with extrahepatic pseudoaneurysms of the hepatic arteries. *J Am Coll Surg* 1998; **186:** 325-330
12 **Genyk YS**, Keller FS, Halpern NB. **Hepatic artery pseudoa**neurysm and hemobilia following laser laparoscopic cholecystectomy. A case report. *Surg Endosc* 1994; **8**: 201-204
13 **Messina LM,** Shanley CJ. Visceral artery aneurysms. *Surg Clin North Am* 1997; **77:** 425-442
14 **Abbas MA,** Fowl RJ, Stone WM, Panneton JM, Oldenburg WA, Bower TC, Cherry KJ, Gloviczki P. Hepatic artery aneurysm: factors that predict complications. *J Vasc Surg* 2003; **38:** 41-45
15 **Chandramohan AN**, Fitzgerald S, Sherlock D, Tam E. Sonographic diagnosis and follow-up of idiopathic hepatic artery aneurysm, an unusual cause of obstructive jaundice. *J Clin Ultrasound* 2001; **29**: 466-471
16 **Kim HJ**, Kim KW, Kim AY, Kim TK, Byun JH, Won HJ, Shin YM, Kim PN, Ha HK, Lee SG, Lee MG. Hepatic artery pseudoaneurysms in adult living-donor liver transplantation: efficacy of CT and Doppler sonography. *AJR Am J Roentgenol* 2005; **184**: 1549-1555
17 **Lin YH,** Lee RC, Hsia CY, Chen HC, Chiang JH, Tseng HS, Chang CY. Right hepatic artery pseudoaneurysm ruptured into the gallbladder demonstrated by magnetic resonance angiography. *J Chin Med Assoc* 2010; **73:** 331-333
18 **Loffroy R**, Rao P, Ota S, De Lin M, Kwak BK, Krause D, Geschwind JF. Packing technique for endovascular coil embolisation of peripheral arterial pseudo-aneurysms with preservation of the parent artery: safety, efficacy and outcomes. *Eur J Vasc Endovasc Surg* 2010; **40**: 209-215
19 **Paci E**, Antico E, Candelari R, Alborino S, Marmorale C, Landi E. Pseudoaneurysm of the common hepatic artery: treatment with a stent-graft. *Cardiovasc Intervent Radiol* ; **23**: 472-474
20 **Ikeda O**, Nakasone Y, Tamura Y, Yamashita Y. Endovascular management of visceral artery pseudoaneurysms: transcatheter coil embolization using the isolation technique. *Cardiovasc Intervent Radiol* 2010; **33**: 1128-1134

S- Editor Cheng JX **L- Editor** Webster JR **E- Editor** Xiong L

World Journal of Radiology

Online Submissions: http://www.wjgnet.com/1949-8470office
wjr@wjgnet.com
doi:10.4329/wjr.v4.i3.121

World J Radiol 2012 March 28; 4(3): 121-125
ISSN 1949-8470 (online)

CASE REPORT

Balloon-occluded retrograde transvenous obliteration for gastric varices *via* the intercostal vein

Hiroki Minamiguchi, Nobuyuki Kawai, Morio Sato, Akira Ikoma, Munehisa Sawa, Tetsuo Sonomura, Shinya Sahara, Kouhei Nakata, Isao Takasaka, Motoki Nakai

Hiroki Minamiguchi, Nobuyuki Kawai, Morio Sato, Akira Ikoma, Munehisa Sawa, Tetsuo Sonomura, Shinya Sahara, Kouhei Nakata, Isao Takasaka, Motoki Nakai, Department of Radiology, Wakayama Medical University 811-1 Kimiidera, Wakayama Shi, Wakayama 641-8510, Japan

Author contributions: Minamiguchi H, Kawai N and Sawa M performed the case; Ikoma A, Sonomura T, Sahara S, Nakata K, Takasaka I and Nakai M revised the manuscript; Minamiguchi H and Sato M wrote the manuscript.

Correspondence to: Hiroki Minamiguchi, Assistant Professor, Department of Radiology, Wakayama Medical University 811-1 Kimiidera, Wakayama Shi, Wakayama 641-8510, Japan. hiromina3@hotmail.com

Telephone: +81-73-4410604 Fax: +81-73-4443110

Received: July 17, 2011 Revised: February 20, 2012
Accepted: February 27, 2012
Published online: March 28, 2012

Abstract

Gastric varices are usually associated with a gastro-renal (G-R) shunt. However, the gastric varices described in this case report were not associated with a G-R shunt. The inflow vessel was the posterior gastric vein and the outflow vessels were the narrow inferior phrenic vein and the dilated cardio-phrenic vein. First, percutaneous transhepatic obliteration of the posterior gastric vein was performed, but the gastric varices remained patent. Then, micro-balloon catheterization of the subphrenic vein was carried out *via* the jugular vein, pericardial vein and cardio-phrenic vein, however, micro-balloon-occluded inferior phrenic venography followed by micro-coil embolization of the cardio-phrenic vein revealed no delineation of gastric varices resulting in no further treatment. Thereafter, as a gastro-subphrenic-intercostal vein shunt developed, a micro-balloon catheter was advanced to the gastric varices *via* the intercostal vein and balloon-occluded retrograde transvenous obliteration (BRTO) was performed resulting in the eradication of gastric varices. BRTO for gastric varices *via* the intercostal vein has not previously been documented.

Key words: Balloon-occluded retrograde transvenous obliteration; Gastric varices; Gastro-subphrenic-intercostal vein shunt; Hepatocellular carcinoma; Intercostal vein

Peer reviewer: Hadi Rokni Yazdi, MD, Associate Professor, Department of Radiology, Central Radiology, Imam Khomeini Hospital, Tehran University of Medical Sciences, Keshavarz Blvd, Tehran 1419733141, Iran

Minamiguchi H, Kawai N, Sato M, Ikoma A, Sawa M, Sonomura T, Sahara S, Nakata K, Takasaka I, Nakai M. Balloon-occluded retrograde transvenous obliteration for gastric varices *via* the intercostal vein. *World J Radiol* 2012; 4(3): 121-125 Available from: URL: http://www.wjgnet.com/1949-8470/full/v4/i3/121.htm DOI: http://dx.doi.org/10.4329/wjr.v4.i3.121

INTRODUCTION

Once gastric varices rupture, bleeding is extremely dangerous and sometimes fatal because the volume of hemorrhage is often large. Treatment procedures for gastric varices such as surgical portosystemic shunt, percutaneous transhepatic obliteration (PTO) and transjugular intrahepatic portosystemic shunt may be effective[1]. However, balloon-occluded retrograde transvenous obliteration (BRTO), which was first reported by Kanagawa *et al*[2], is becoming a well-established treatment for gastric varices, whether hemorrhagic or prophylactic, as BRTO is less invasive than the other procedures and offers good control even if hepatic function is poor. During BRTO, the sclerosant is infused into the gastric varices under occlusion of the draining vessel by balloon inflation. Gastric varices most commonly have a spontaneous gastro-renal (G-R)

shunt with the left adrenal vein targeted as the main draining vessel by balloon inflation. However, gastric varices which are not associated with a G-R shunt have been observed[3,4]. The outflow vessels of gastric varices without a G-R shunt such as the inferior phrenic vein, cardio-phrenic vein, pericardial vein, retroperitoneal vein and intercostal vein are anatomically listed[5]. We present a patient who underwent BRTO performed by catheterization *via* the intercostal vein for gastric varices with a gastro-subphrenic-intercostal shunt.

The institutional review board at our hospital did not require approval for this retrospective case.

CASE REPORT

A 55-year-old man with chronic liver disorder due to hepatitis B virus infection was introduced to our hospital because the family doctor had diagnosed a liver tumor. Laboratory data revealed Child-Pugh A liver dysfunction (Child-Pugh score 5) and high α-fetoprotein (AFP) and protein induced vitamin K absence or antagonist Ⅱ (PIVKA-Ⅱ) values of 230 ng/mL and 273780 mAU/mL, respectively. Dynamic computed tomography (CT) demonstrated gastric varices with no G-R shunt and a large hepatocellular carcinoma (HCC) of 13 cm in diameter in the right lobe (Figure 1A).

In the multidisciplinary conference which included surgeons, interventional radiologists and hepatologists, the patient was scheduled to receive PTO for gastric varices, percutaneous transhepatic portal vein embolization (PTPE) and thereafter, right hepatectomyas the volume of the medial and lateral segment was too small to tolerate right lobe hepatectomy, and PTPE was anticipated to deteriorate gastric varices due to secondary portal hypertention[6-8]. Under ultrasound guidance, the posterior inferior subsegment of the portal vein branch was punctured using an 18 gauge needle and a 4 Fr sheath was inserted. Percutaneous transhepaticsplenography using a 4 Fr pigtail catheter revealed that the inflow vessel of the gastric varices was the posterior gastric vein and the outflow vessel was the dilated cardio-phrenic vein and narrow inferior phrenic vein. Then, PTO of the posterior gastric vein for gastric varices was attempted. A micro-balloon catheter was advanced through the sheath to the posterior gastric vein and under micro-balloon inflation, 50% glucose, 5% ethanolamine oleate-iopamidol (EOI) and microcoils were used for occlusion of the posterior gastric vein. PTPE of the anterior and posterior segments using lipiodol, gelatin sponge particles and microcoils was conducted *via* the same transhepatic access route (Figure 1B). However, enhanced CT one month later demonstrated that patent gastric varices remained, and the medial and lateral segments did not enlarge as expected. Laboratory tests also revealed no improvement in the indocyanine green retention ratio of 15 min (ICG-R15) (9% to 8%). Therefore, instead of surgical hepatectomy, the patient underwent single photon emission computed tomography-based three-dimensional conformal radiotherapy (SPECT-B-3D-CRT) targeting the large HCC to a total dose of 45 Gy/18 fractions with transcatheter arterial chemoembolization (TACE) resulting in tumor shrinkage with marked decreases in AFP and PIVKA-Ⅱ values (18.7 ng/mL and 120 mAU/mL, respectively).

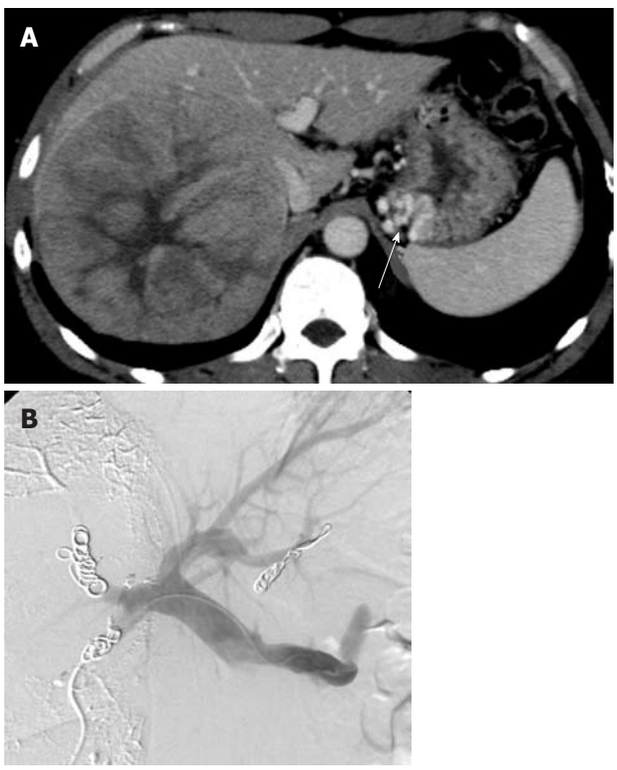

Figure 1 A 55-year-old man with gastric varices due to hepatitis B liver cirrhosis. A: Hepatocellular carcinoma of 13 cm in the right lobe. Gastric varices were also demonstrated (arrow); B: Percutaneous transhepatic obliteration of the posterior gastric vein using 5% ethanolamine oleate-iopamidol and microcoils was performed to occlude the gastric varices. Percutaneous transhepatic portal vein embolization of the right posterior and anterior segments of the portal vein using lipiodol, gelatin sponge particles and microcoils was conducted using the same transhepatic catheter route in order to enlarge the left hepatic lobe for possible right hepatectomy.

Follow-up gastrointestinal endoscopy demonstrated the presence of gastric varices and a new small gastric cancer. Endoscopic ultrasoundscopy revealed that the gastric cancer was limited to the submucosal layer, however, gastric varices were observed beneath the gastric cancer. The surgeon asked for the gastric varices to be eradicated in order to undertake endoscopic submucosal dissection (ESD) to remove the early gastric cancer. Dynamic CT demonstrated gastric varices with no G-R shunt, however, the presence of the narrow left inferior phrenic vein and dilated cardio-phrenic vein were noted. Catheterization of the inferior phrenic vein was attempted but was difficult due to the narrowness of the vein. We inserted a micro-balloon catheter into the pericardial vein *via* the left jugular vein and left innominate vein. Micro-balloon-occluded pericardial venography (Figure 2A) revealed the narrow subphrenic vein, dilatation of the cardio-phrenic vein and the subphrenicbranch veins but did not delineate the gastric varices. We then inserted

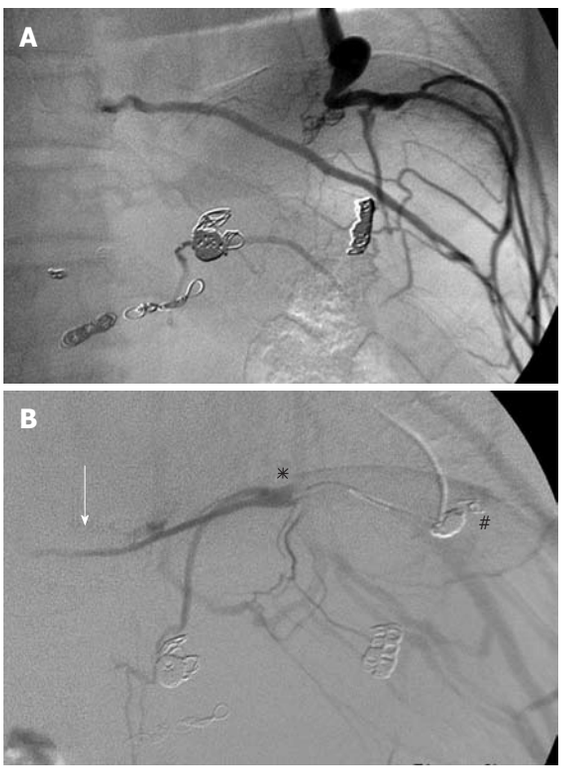

Figure 2 Micro-balloon-occluded pericardial venography. A: Micro-balloon occluded venography (M-BOV) of the pericardial vein demonstrated the development of the cardio-phrenic vein and phrenic branch veins; B: Embolization of the cardio-phrenic vein using 9 microcoils (#) was conducted in order to reduce the collateral vessels. However, M-BOV of the left subphrenic vein (asterisk) followed by coil embolization demonstrated the narrow outlet of the subphrenic vein (arrow) and the dilated phrenic branches but not gastric varices. Further advancement of the micro-balloon catheter was difficult.

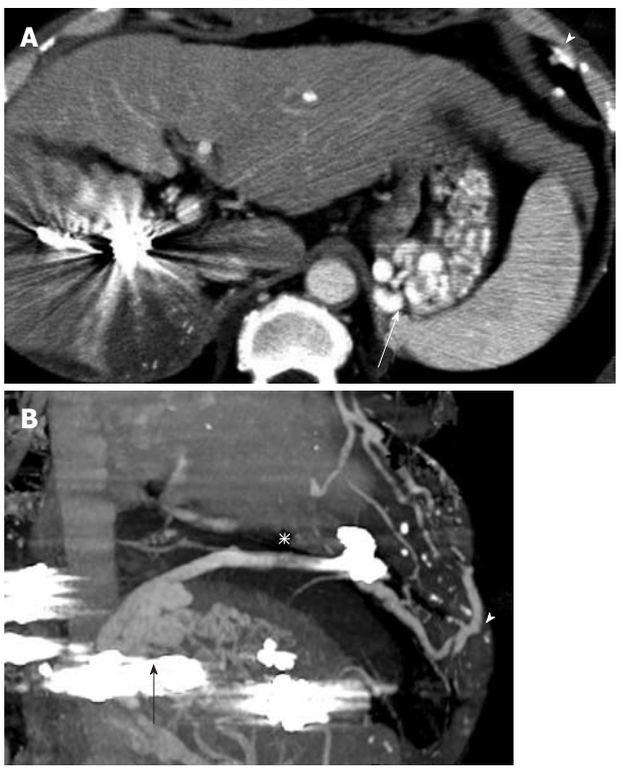

Figure 3 Portal phase of dynamic computed tomography images using contrast medium before balloon-occluded retrograde transvenous obliteration. A: Axial image demonstrated enlargement of gastric varices (arrow) and intercostal vein (arrowhead) with marked shrinkage of hepatocellular carcinoma; B: Multi-planar reconstruction computed tomography image demonstrated the gastric varices (arrow) and the dilated phrenic branch (asterisk) communicating with intercostal vein (arrowhead).

a balloon catheter into the left subphrenic vein followed by coil embolization of the cardio-phrenic vein to reduce the collateral pathways. However, micro-balloon-occluded subphrenic venography (Figure 2B) revealed still no delineation of gastric varices. Further catheterization using the micro-balloon catheter toward the gastric vein was difficult. As growth of the early gastric cancer was slow, we waited one month anticipating development of the inferior phrenic vein and hoped that simultaneous micro-balloon inflations of the subphrenic vein and pericardial vein might lead to delineation of the gastric varices.

Beyond our expectation, axial and sagittal oblique images of multi-planar reconstruction enhanced CT medium one month later (Figure 3), revealed the gastric varices draining to the development gastrosubphrenic-intercostal shunt. BRTO for gastric varices *via* the intercostal vein was then carried out. Under ultrasound guidance, the 7th inter-costal vein was punctured using an 18-gauge needle, and a 6 French guiding catheter (ELWAY C2 type, Terumo Clinical Supply, Gifu, Japan) was inserted followed by advancement of a 0.035 inch guidewire (Surf, Piolax, Yokohama, Japan). The patient complained of slight pain during catheterization because the catheter contacted with the rib and friction arose during respiration. Drip infusion of the analgesic (pentazocine hydrochloride) was effective in relieving pain. A micro-balloon catheter (Iiguman, 7 mm diameter, Fuji System, Fukushima, Japan) was coaxially inserted through the guiding catheter and advanced using a microwire (HI-LEX, Hyogo, Japan) to the retroperitoneal vein which directly drained the gastric varices *via* the subphrenic vein. Micro-balloon inflation was not enough to interrupt the blood flow because the diameter of the draining vein was too large. Thus, a micro-balloon was inserted into the neck of the gastric varices and then inflated, resulting in the stagnation of blood flow. BRTO was conducted using 5% EOI mixed with 10% ethanolamine oleate (Oldamine, Fuji Chemical, Toyama, Japan) and the same dose of contrast medium (Iopamidol, 300 mg iodine) (Figure 4). Intravenous drip infusion of 4000 units of human hepatoglobin (Benesis, Kyoto, Japan) was administered for approximately 30 min before BRTO. To reduce the dose of the sclerosing agent to a minimum, 10 mL of 50% glucose was infused initially and a total of 7.5 mL of 5% EOI was infused into the gastric varices *via* the microcatheter under balloon inflation. However, we realized that stagnation of EOI was temporary due to the presence of other small outflow channels. Ethanol 99% mixed with lipiodol (4:1) was also injected to occlude the channels. After confirmation of the disappearance of the channels, another 7.5 mL of 5% EOI was infused resulting in satisfactory stagnation.

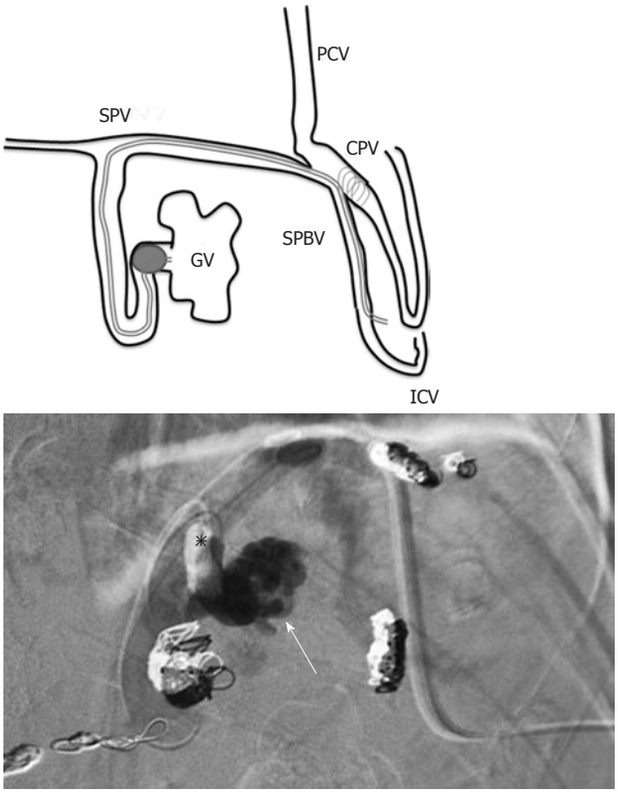

Figure 4 The strategy and actual images of balloon-occluded retrograde transvenous obliteration *via* the intercostal vein. A: Schema of the micro-balloon catheter inserted *via* the 7th intercostal vein (ICV) and advanced to the gastric varices (GV) through the subphrenic branch vein (SPBV) and subphrenic vein (SPV); B: After balloon inflation (asterisk), balloon-occluded retrograde transvenous obliteration (BRTO) using 5% ethanolamine oleate-iopamidol (EOI) and ethanol mixed with lipiodol was conducted. The radiograph immediately after BRTO showed the accumulation of EOI corresponding to the gastric varices (arrow). PCV: Pericardial vein; CPV: Cardio-phrenic vein.

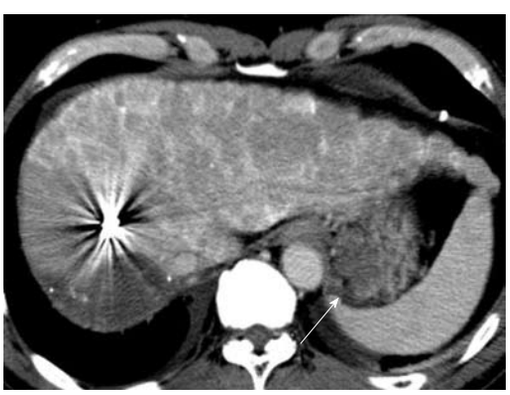

Figure 5 Dynamic computed tomography the following day showed no enhancement of gastric varices (arrow).

Micro-balloon inflation was maintained overnight in the ward, and the thrombosed gastric varices were confirmed the following day by contrast-enhanced CT. Thereafter, the puncture route of the intercostal vein was occluded completely using microcoils (COOK Europe, Bjaeverskov, Denmark) of 2 to 6 mm in diameter. Enhanced CT the following day revealed no delineation of gastric varices (Figure 5), which allowed the patient to receive ESD.

DISCUSSION

Gastric varices draining into a G-R shunt occur with a high incidence of 84 to 97%[3,5]. When a G-R shunt, as the main draining vein from gastric varices is present, collateral outflows such as the left subphrenic vein, pericardio-phrenic vein, gonadal vein and retroperitoneal veins are often observed. These collateral outflows are anticipated to develop in cases of gastric varices without a G-R shunt. Kameda *et al*[3] demonstrated that as the draining vessel from gastric varices without a G-R shunt, the subphrenic vein is the most important followed by the pericardial vein and paraesophageal vein. In the present study involving a patient with gastric varices without a GR shunt, the inflow vessel was the posterior gastric vein and the outflow vessels were the dilated cardio-phrenic vein and the narrow subphrenic vein. The narrow subphrenic vein and coil embolization of the cardio-phrenic vein developed the draining route of the gastrosubphrenic-intercostal shunt.

Chikamori *et al*[9] attempted to treat gastric varices with a gastropericardiac shunt using PTO of the posterior gastric vein which resulted in the successful shrinkage of gastric varices. Despite PTO of the posterior gastric vein, the occlusion of gastric varices was not satisfactory in the present case. In order to perform ESD for early gastric cancer safely, the eradication of gastric varices was requested. Subphrenic venography under inflation of the micro-balloon catheter followed by coil embolization of the cardio-phrenic vein did not lead to delineation of gastric varices. One month later, following the development of a gastrosubphrenic-intercostal shunt, BRTO *via* the intercostal vein was performed resulting in complete thrombosis of gastric varices. To the best of our knowledge, BRTO for gastric varices *via* the intercostal vein route has not been documented.

The insertion of a catheter into an intact intercostal vein is generally difficult because of its narrow diameter. In this case, a dilated intercostal vein developed and under ultrasound guidance, puncture and catheter insertion were performed without difficulty. The friction of the catheter on the rib during respiration caused slight pain which resolved with the administration of analgesics. Pressure hemostasis by hand at the intercostal vein puncture site after withdrawal of the catheter was difficult. Microcoil embolization was then carried out adjacent to the puncture site resulting in no recurrent bleeding.

This patient suffered from a giant HCC of 13 cm in diameter. Shirai*et al*[10] reported that the combination of SPECT-B-3D-CRT and TACE achieved a median survival of 13.5 mo in HCC patients with portal vein tumor thrombus which was comparable to that (13.6 mo) reported in a surgical hepatectomy series. The patient survived more than 2 years following SPECT-B-3D-CRT and TACE.

We conclude that in this case, the draining route of the gastrosubphrenic-intercostal shunt was developed by the narrow subphrenicvein and coil embolization of the cardio-phrenic vein, and BRTO for gastric varices *via* the intercostal vein resulted in eradication of gastric varices.

REFERENCES

1 **Rössle M**, Deibert P, Haag K, Ochs A, Olschewski M, Siegerstetter V, Hauenstein KH, Geiger R, Stiepak C, Keller W, Blum HE. Randomised trial of transjugular-intrahepatic-portosystemic shunt versus endoscopy plus propranolol for prevention of variceal rebleeding. *Lancet* 1997; **349**: 1043-1049

2 **Kanagawa H**, Mima S, Kouyama H, Gotoh K, Uchida T, Okuda K. Treatment of gastric fundal varices by balloon-occluded retrograde transvenous obliteration. *J Gastroenterol Hepatol* 1996; **11**: 51-58

3 **Kameda N**, Higuchi K, Shiba M, Kadouchi K, Machida H, Okazaki H, Tanigawa T, Watanabe T, Tominaga K, Fujiwara Y, Nakamura K, Arakawa T. Management of gastric fundal varices without gastro-renal shunt in 15 patients. *World J Gastroenterol* 2008; **14**: 448-453

4 **Kiyosue H**, Mori H, Matsumoto S, Yamada Y, Hori Y, Okino Y. Transcatheter obliteration of gastric varices. Part 1. Anatomic classification. *Radiographics* 2003; **23**: 911-920

5 **Maeda H**, Hirota S, Yamamoto S, Kobayashi K, Arai K, Miyamoto Y, Fukuda T, Sugimoto K, Nakao N. Radiologic variations in gastrorenal shunts and collateral veins from gastric varices in images obtained before balloon-occluded retrograde transvenous obliteration. *Cardiovasc Intervent Radiol* 2007; **30**: 410-414

6 **Abulkhir A**, Limongelli P, Healey AJ, Damrah O, Tait P, Jackson J, Habib N, Jiao LR. Preoperative portal vein embolization for major liver resection: a meta-analysis. *Ann Surg* 2008; **247**: 49-57

7 **Tanaka H**, Hirohashi K, Kubo S, Shuto T, Higaki I, Kinoshita H. Preoperative portal vein embolization improves prognosis after right hepatectomy for hepatocellular carcinoma in patients with impaired hepatic function. *Br J Surg* 2000; **87**: 879-882

8 **Arai H**, Abe T, Takagi H, Mori M. Efficacy of balloon-occluded retrograde transvenous obliteration, percutaneous transhepatic obliteration and combined techniques for the management of gastric fundal varices. *World J Gastroenterol* 2006; **12**: 3866-3873

9 **Chikamori F**, Kuniyoshi N, Kawashima T, Shibuya S, Takase Y. Percutaneous transhepatic obliteration for isolated gastric varices with gastropericardiac shunt: case report. *Abdom Imaging* 2006; **31**: 249-252

10 **Shirai S**, Sato M, Suwa K, Kishi K, Shimono C, Sonomura T, Kawai N, Tanihata H, Minamiguchi H, Nakai M. Feasibility and efficacy of single photon emission computed tomography-based three-dimensional conformal radiotherapy for hepatocellular carcinoma 8 cm or more with portal vein tumor thrombus in combination with transcatheter arterial chemoembolization. *Int J Radiat Oncol Biol Phys* 2010; **76**: 1037-1044

S- Editor Cheng JX **L- Editor** Webster JR **E- Editor** Xiong L

World Journal of Radiology

Online Submissions: http://www.wjgnet.com/1949-8470office
wjr@wjgnet.com
www.wjgnet.com

World J Radiol 2012 March 28; 4(3): I
ISSN 1949-8470 (online)

Acknowledgments to reviewers of *World Journal of Radiology*

Many reviewers have contributed their expertise and time to the peer review, a critical process to ensure the quality of *World Journal of Radiology*. The editors and authors of the articles submitted to the journal are grateful to the following reviewers for evaluating the articles (including those published in this issue and those rejected for this issue) during the last editing time period.

Tommaso Bartalena, MD, PhD, Radiology, S. Orsola University Hospital, Via Massarenti 9, 40138 Bologna, Italy

Rivka R Colen, Dr., Department of Radiology, Brigham and Women's Hospital/Harvard Medical School, 150 Brookline Ave Apt 703, Boston, MA 02215, United States

Sergio Casciaro, PhD, Institute of Clinical Physiology - National Research Council, Campus Universitario Ecotekne, Via Monteroni, 73100 Lecce, Italy

Aaron Cohen-Gadol, MD, MSc, Clinical Assistant Professor, Indiana University Department of Neurosurgery, Clarian Neuroscience Center, 1801 North Senate Blvd, Suite 610, Indianapolis, IN 46202, United States

Shigeru Ehara, MD, Professor, Chair, Iwate Medical University School of Medicine, Morioka 020-8505, Japan

Mohamed Abou El-Ghar, MD, Radiology department, Urology and Nephrology center-Mansoura University,72 El-gomhoria st, Mansoura 35516, Egypt

Tayfun Hakan, MD, Neurosurgery Clinic, Haydarpasa Numune Teaching and Research Hospital, Tibbiye Caddesi, Uskudar 34668, Istanbul, Turkey

Takao Hiraki, MD, **Assistant Professor,** Department of Radiology, Okayama University Medical School, 3-5-1 Shikatacho, Okayama 700-0861, Japan

Tarik F Massoud, MB, BCh, BAO, LRCPI, LRCSI, MA, MD, PhD, FRCR, Department of Radiology, University of Cambridge, Addenbrooke's Hospital, Box 219, Hills Road, Cambridge CB2 2QQ, United Kingdom

Tilo Niemann, MD, Department of Radiology, University Hospital Basel, Petersgraben 4, CH-4031 Basel, Switzerland

Kazushi Numata, MD, PhD, Associate Professor, Gastroenterological Center, Yokohama City University Medical Center, 4-57 Urafune-cho, Minami-ku, Yokohama, Kanagawa 232-0024, Japan

Tetsu Niwa, MD, PhD, Department of Radiology, Kanagawa Children's Medical Center, 2-138-4 Mutsukawa, Minamiku, Yokohama 252-8555, Japan

Farideh Nejat, MD, MPH, Department of Neurosurgery, Children's Hospital Medical Center, Tehran University of Medical Sciences, Gharib Street, Mail Box 14155-7854, Tehran, Iran

Paul V Puthussery, MD, DMRD, MNAMS, DNB, Assistant Professor, Department of Radiodiagnosis, Government Medical College, Kochi 683571, India

Zhonghua Sun, PhD, Discipline of Medical Imaging, Department of Imaging and Applied Physics, Curtin University of Technology, GPO Box U 1987, Perth, Western Australia 6845, Australia

Hadi Rokni Yazdi, MD, Associate Professor, Department of Radiology, Central Radiology, Imam Khomeini Hospital, Tehran University of Medical Sciences, Keshavarz Blvd, Tehran 1419733141, Iran

WJR World Journal of Radiology

Online Submissions: http://www.wjgnet.com/1949-8470office
wjr@wjgnet.com
www.wjgnet.com

World J Radiol 2012 March 28; 4(3): I
ISSN 1949-8470 (online)

Events Calendar 2012

January 3-7, 2012
Imaging at Bachelor Gulch
Beaver Creek, CO 81620,
United States

January 12-14, 2012
IROS 2012: Interventionell
Radiologischen Olbert Symposium
Salzburg, Austria

January 26-29, 2012
American Society of Neuroimaging
2012 35th Annual Meeting
Miami, FL 33169, United States

February 9-11, 2012
JIM joint interventional meeting
2012
Rome, Italy

February 13-16, 2012
Emergency Radiology
Palm Beach, FL 33480, United States

February 16-19, 2012
ASSR 2012 Annual Symposium
Miami Beach, FL 33169,
United States

February 19-23, 2012
Internal Derangements of Joints:
Advanced and Intensive MR
Imaging/With a Special Symposium
on Ankle and Foot
Coronado, CA 92118, United States

February 21-24, 2012
MRI in Practice
Oslo, Norway

March 1-5, 2012
ECR 2012
Vienna, Austria

March 7-10, 2012
ISCD's 18th Annual Meeting
Los Angeles, CA 90001,
United States

March 7-11, 2012
7th Annual Fundamentals of
Musculoskeletal Ultrasound
San Diego, CA 92111, United States

March 25-30, 2012
Diseases of the Brain, Head and
Neck Spine
Davos, Switzerland
April 13-15, 2012
ACR 35th National Conference on
Breast Cancer
Hollywood, FL 33019, United States

April 22-24, 2012
Euroson 2012
Madrid, Spain

April 24-27, 2012
MRI in Practice
Aalst, Belgium

April 25-28, 2012
ECIO 2012 - Third European
Conference on Interventional
Oncology
Florence, Italy

May 15-18, 2012
EURO PCR
Paris, France

May 19-23, 2012
ECTS 2012
Stockholm, Sweden

May 28-June 01, 2012
The International Congress of
Pediatric Radiology
Athens Greece

June 7-9, 2012
ASCI 2012 6th Congress of Asian
Society of Cardiovascular Imaging
Bangkok, Thailand

June 14-16, 2012
ICCIR 2012 – International
Conference on Complications in
Interventional Radiology
Poertschach, Austria

June 16-19, 2012
2nd IDKD Hong Kong 2012,
Diseases of the Abdomen and Pelvis
Hong Kong, China

June 17-20, 2012
14th Annual International
Symposium on Multidetector-Row
CT
San Francisco, CA **94103,**
United States

June 27-30, 2012
CARS 2012
Pisa, Italy

July 1-3, 2012
16th Symposium Mammographicum
Harrogate, United Kingdom

July 19-22, 2012
Society of Cardiovascular Computed
Tomography 6th Annual Scientific
Meeting
Baltimore, Maryland

August 30-2, 2012
14th Asian Oceanian Congress of
Radiology
Sydney, Australia

September 6-8, 2012
Update in Abdominal and
Urogenital Imaging
Bruges, Belgium

September 12-15, 2012
ISS 2012
Rome, Italy

September 13-15, 2012
4th ESMINT Congress
Nice, France

September 13-16, 2012
18th Annual Symposium ESUR
Edinburgh, United Kingdom

September 15-19, 2012
CIRSE 2012
Lisbon, Portugal

September 20-23, 2012
2012 SDMS Annual Conference
Seattle, WA 98113, United States

September 24-27, 2012
MRI in Practice
Ballerup, Denmark

October 4-6, 2012
ESMRMB congress 2012 29th Annual
Scientific Meeting
Lisbon, Portugal

October 12-13, 2012
EUSOBI Annual Scientific Meeting
2012
Barcelona, Spain

October 26-28, 2012
22th Annual Meeting of the Society
of Radiologists in Ultrasound
Baltimore, MD 21213, United States

November 10-14, 2012
13th congress of WFITN
Buenos Aires, Agentina

November 14-17, 2012
BSIR Annual Meeting 2012
Bournemouth, United Kingdom

November 27- December 03, 2012
IEEE Nuclear Science Symposium
and Medical Imaging Conference
Anaheim, CA 92805, United States

December 2-4, 2012
ICI 2012 - Innovations in
Cardiovascular Interventions
Meeting
Tel Aviv, Israel

December 4-8, 2012
34rd San Antonio Breast Cancer
Symposium,
San Antonio, TX 78258 ,
United States

WJR World Journal of Radiology

Online Submissions: http://www.wjgnet.com/1949-8470office
wjr@wjgnet.com
www.wjgnet.com

World J Radiol 2012 March 28; 4(3): I-V
ISSN 1949-8470 (online)

INSTRUCTIONS TO AUTHORS

GENERAL INFORMATION

World Journal of Radiology (*World J Radiol*, *WJR*, online ISSN 1949-8470, DOI: 10.4329), is a monthly, open-access (OA), peer-reviewed journal supported by an editorial board of 319 experts in Radiology from 40 countries.

The biggest advantage of the OA model is that it provides free, full-text articles in PDF and other formats for experts and the public without registration, which eliminates the obstacle that traditional journals possess and usually delays the speed of the propagation and communication of scientific research results. The open access model has been proven to be a true approach that may achieve the ultimate goal of the journals, i.e. the maximization of the value to the readers, authors and society.

Maximization of personal benefits

The role of academic journals is to exhibit the scientific levels of a country, a university, a center, a department, and even a scientist, and build an important bridge for communication between scientists and the public. As we all know, the significance of the publication of scientific articles lies not only in disseminating and communicating innovative scientific achievements and academic views, as well as promoting the application of scientific achievements, but also in formally recognizing the "priority" and "copyright" of innovative achievements published, as well as evaluating research performance and academic levels. So, to realize these desired attributes of *WJR* and create a well-recognized journal, the following four types of personal benefits should be maximized. The maximization of personal benefits refers to the pursuit of the maximum personal benefits in a well-considered optimal manner without violation of the laws, ethical rules and the benefits of others. (1) Maximization of the benefits of editorial board members: The primary task of editorial board members is to give a peer review of an unpublished scientific article via online office system to evaluate its innovativeness, scientific and practical values and determine whether it should be published or not. During peer review, editorial board members can also obtain cutting-edge information in that field at first hand. As leaders in their field, they have priority to be invited to write articles and publish commentary articles. We will put peer reviewers' names and affiliations along with the article they reviewed in the journal to acknowledge their contribution; (2) Maximization of the benefits of authors: Since *WJR* is an open-access journal, readers around the world can immediately download and read, free of charge, high-quality, peer-reviewed articles from *WJR* official website, thereby realizing the goals and significance of the communication between authors and peers as well as public reading; (3) Maximization of the benefits of readers: Readers can read or use, free of charge, high-quality peer-reviewed articles without any limits, and cite the arguments, viewpoints, concepts, theories, methods, results, conclusion or facts and data of pertinent literature so as to validate the innovativeness, scientific and practical values of their own research achievements, thus ensuring that their articles have novel arguments or viewpoints, solid evidence and correct conclusion; and (4) Maximization of the benefits of employees: It is an iron law that a first-class journal is unable to exist without first-class editors, and only first-class editors can create a first-class academic journal. We insist on strengthening our team cultivation and construction so that every employee, in an open, fair and transparent environment, could contribute their wisdom to edit and publish high-quality articles, thereby realizing the maximization of the personal benefits of editorial board members, authors and readers, and yielding the greatest social and economic benefits.

Aims and scope

The major task of *WJR* is to rapidly report the most recent improvement in the research of medical imaging and radiation therapy by the radiologists. *WJR* accepts papers on the following aspects related to radiology: Abdominal radiology, women health radiology, cardiovascular radiology, chest radiology, genitourinary radiology, neuroradiology, head and neck radiology, interventional radiology, musculoskeletal radiology, molecular imaging, pediatric radiology, experimental radiology, radiological technology, nuclear medicine, PACS and radiology informatics, and ultrasound. We also encourage papers that cover all other areas of radiology as well as basic research.

Columns

The columns in the issues of *WJR* will include: (1) Editorial: To introduce and comment on major advances and developments in the field; (2) Frontier: To review representative achievements, comment on the state of current research, and propose directions for future research; (3) Topic Highlight: This column consists of three formats, including (A) 10 invited review articles on a hot topic, (B) a commentary on common issues of this hot topic, and (C) a commentary on the 10 individual articles; (4) Observation: To update the development of old and new questions, highlight unsolved problems, and provide strategies on how to solve the questions; (5) Guidelines for Basic Research: To provide guidelines for basic research; (6) Guidelines for Clinical Practice: To provide guidelines for clinical diagnosis and treatment; (7) Review: To review systemically progress and unresolved problems in the field, comment on the state of current research, and make suggestions for future work; (8) Original Articles: To report innovative and original findings in radiology; (9) Brief Articles: To briefly report the novel and innovative findings in radiology; (10) Case Report: To report a rare or typical case; (11) Letters to the Editor: To discuss and make reply to the contributions published in *WJR*, or to introduce and comment on a controversial issue of general interest; (12) Book Reviews: To introduce and comment on quality monographs of radiology; and (13) Guidelines: To introduce consensuses and guidelines reached by international and national academic authorities worldwide on the research in radiology.

Name of journal

World Journal of Radiology

ISSN

ISSN 1949-8470 (online)

Editor-in-Chief

Editorial Office

World Journal of Radiology
Editorial Department: Room 903, Building D,
Ocean International Center, No. 62 Dongsihuan Zhonglu,
Chaoyang District, Beijing 100025, China

E-mail: wjr@wjgnet.com
http://www.wjgnet.com
Telephone: +86-10-59080039
Fax: +86-10-85381893

Indexed and Abstracted in
PubMed Central, PubMed, Digital Object Identifer, and Directory of Open Access Journals.

Published by
Baishideng Publishing Group Co., Limited.

SPECIAL STATEMENT

All articles published in this journal represent the viewpoints of the authors except where indicated otherwise.

Biostatistical editing
Statisital review is performed after peer review. We invite an expert in Biomedical Statistics from to evaluate the statistical method used in the paper, including *t*-test (group or paired comparisons), chi-squared test, Ridit, probit, logit, regression (linear, curvilinear, or stepwise), correlation, analysis of variance, analysis of covariance, *etc*. The reviewing points include: (1) Statistical methods should be described when they are used to verify the results; (2) Whether the statistical techniques are suitable or correct; (3) Only homogeneous data can be averaged. Standard deviations are preferred to standard errors. Give the number of observations and subjects (*n*). Losses in observations, such as drop-outs from the study should be reported; (4) Values such as ED50, LD50, IC50 should have their 95% confidence limits calculated and compared by weighted probit analysis (Bliss and Finney); and (5) The word 'significantly' should be replaced by its synonyms (if it indicates extent) or the *P* value (if it indicates statistical significance).

Conflict-of-interest statement
In the interests of transparency and to help reviewers assess any potential bias, *WJR* requires authors of all papers to declare any competing commercial, personal, political, intellectual, or religious interests in relation to the submitted work. Referees are also asked to indicate any potential conflict they might have reviewing a particular paper. Before submitting, authors are suggested to read "Uniform Requirements for Manuscripts Submitted to Biomedical Journals: Ethical Considerations in the Conduct and Reporting of Research: Conflicts of Interest" from International Committee of Medical Journal Editors (ICMJE), which is available at: http://www.icmje.org/ethical_4conflicts.html.

Sample wording: [Name of individual] has received fees for serving as a speaker, a consultant and an advisory board member for [names of organizations], and has received research funding from [names of organization]. [Name of individual] is an employee of [name of organization]. [Name of individual] owns stocks and shares in [name of organization]. [Name of individual] owns patent [patent identification and brief description].

Statement of informed consent
Manuscripts should contain a statement to the effect that all human studies have been reviewed by the appropriate ethics committee or it should be stated clearly in the text that all persons gave their informed consent prior to their inclusion in the study. Details that might disclose the identity of the subjects under study should be omitted. Authors should also draw attention to the Code of Ethics of the World Medical Association (Declaration of Helsinki, 1964, as revised in 2004).

Statement of human and animal rights
When reporting the results from experiments, authors should follow the highest standards and the trial should conform to Good Clinical Practice (for example, US Food and Drug Administration Good Clinical Practice in FDA-Regulated Clinical Trials; UK Medicines Research Council Guidelines for Good Clinical Practice in Clinical Trials) and/or the World Medical Association Declaration of Helsinki. Generally, we suggest authors follow the lead investigator's national standard. If doubt exists whether the research was conducted in accordance with the above standards, the authors must explain the rationale for their approach and demonstrate that the institutional review body explicitly approved the doubtful aspects of the study.

Before submitting, authors should make their study approved by the relevant research ethics committee or institutional review board. If human participants were involved, manuscripts must be accompanied by a statement that the experiments were undertaken with the understanding and appropriate informed consent of each. Any personal item or information will not be published without explicit consents from the involved patients. If experimental animals were used, the materials and methods (experimental procedures) section must clearly indicate that appropriate measures were taken to minimize pain or discomfort, and details of animal care should be provided.

SUBMISSION OF MANUSCRIPTS

Manuscripts should be typed in 1.5 line spacing and 12 pt. Book Antiqua with ample margins. Number all pages consecutively, and start each of the following sections on a new page: Title Page, Abstract, Introduction, Materials and Methods, Results, Discussion, Acknowledgements, References, Tables, Figures, and Figure Legends. Neither the editors nor the publisher are responsible for the opinions expressed by contributors. Manuscripts formally accepted for publication become the permanent property of Baishideng Publishing Group Co., Limited, and may not be reproduced by any means, in whole or in part, without the written permission of both the authors and the publisher. We reserve the right to copy-edit and put onto our website accepted manuscripts. Authors should follow the relevant guidelines for the care and use of laboratory animals of their institution or national animal welfare committee. For the sake of transparency in regard to the performance and reporting of clinical trials, we endorse the policy of the ICMJE to refuse to publish papers on clinical trial results if the trial was not recorded in a publicly-accessible registry at its outset. The only register now available, to our knowledge, is http://www.clinicaltrials.gov sponsored by the United States National Library of Medicine and we encourage all potential contributors to register with it. However, in the case that other registers become available you will be duly notified. A letter of recommendation from each author's organization should be provided with the contributed article to ensure the privacy and secrecy of research is protected.

Authors should retain one copy of the text, tables, photographs and illustrations because rejected manuscripts will not be returned to the author(s) and the editors will not be responsible for loss or damage to photographs and illustrations sustained during mailing.

Online submissions
Manuscripts should be submitted through the Online Submission System at: http://www.wjgnet.com/1949-8470office. Authors are highly recommended to consult the ONLINE INSTRUCTIONS TO AUTHORS (http://www.wjgnet.com/1949-8470/g_info_20100316162358.htm) before attempting to submit online. For assistance, authors encountering problems with the Online Submission System may send an email describing the problem to wjr@wjgnet.com, or by telephone: +86-10-85381892. If you submit your manuscript online, do not make a postal contribution. Repeated online submission for the same manuscript is strictly prohibited.

MANUSCRIPT PREPARATION

All contributions should be written in English. All articles must be submitted using word-processing software. All submissions must be typed in 1.5 line spacing and 12 pt. Book Antiqua with ample margins. Style should conform to our house format. Required information for each of the manuscript sections is as follows:

Title page
Title: Title should be less than 12 words.

Running title: A short running title of less than 6 words should be provided.

Authorship: Authorship credit should be in accordance with the standard proposed by International Committee of Medical Journal Editors, based on (1) substantial contributions to conception and design, acquisition of data, or analysis and interpretation of data; (2) drafting the article or revising it critically for important intellectual content; and (3) final approval of the version to be published. Authors should meet conditions 1, 2, and 3.

Institution: Author names should be given first, then the complete name of institution, city, province and postcode. For example, Xu-Chen Zhang, Li-Xin Mei, Department of Pathology, Chengde Medical College, Chengde 067000, Hebei Province, China. One author may be represented from two institutions, for example, George Sgourakis, Department of General, Visceral, and Transplantation Surgery, Essen 45122, Germany; George Sgourakis, 2nd Surgical Department, Korgialenio-Benakio Red Cross Hospital, Athens 15451, Greece

Author contributions: The format of this section should be: Author contributions: Wang CL and Liang L contributed equally to this work; Wang CL, Liang L, Fu JF, Zou CC, Hong F and Wu XM designed the research; Wang CL, Zou CC, Hong F and Wu XM performed the research; Xue JZ and Lu JR contributed new reagents/analytic tools; Wang CL, Liang L and Fu JF analyzed the data; and Wang CL, Liang L and Fu JF wrote the paper.

Supportive foundations: The complete name and number of supportive foundations should be provided, e.g., Supported by National Natural Science Foundation of China, No. 30224801

Correspondence to: Only one corresponding address should be provided. Author names should be given first, then author title, affiliation, the complete name of institution, city, postcode, province, country, and email. All the letters in the email should be in lower case. A space interval should be inserted between country name and email address. For example, Montgomery Bissell, MD, Professor of Medicine, Chief, Liver Center, Gastroenterology Division, University of California, Box 0538, San Francisco, CA 94143, United States. montgomery.bissell@ucsf.edu

Telephone and fax: Telephone and fax should consist of +, country number, district number and telephone or fax number, e.g., Telephone: +86-10-85381892 Fax: +86-10-85381893

Peer reviewers: All articles received are subject to peer review. Normally, three experts are invited for each article. Decision for acceptance is made only when at least two experts recommend an article for publication. Reviewers for accepted manuscripts are acknowledged in each manuscript, and reviewers of articles which were not accepted will be acknowledged at the end of each issue. To ensure the quality of the articles published in *WJR*, reviewers of accepted manuscripts will be announced by publishing the name, title/position and institution of the reviewer in the footnote accompanying the printed article. For example, reviewers: Professor Jing-Yuan Fang, Shanghai Institute of Digestive Disease, Shanghai, Affiliated Renji Hospital, Medical Faculty, Shanghai Jiaotong University, Shanghai, China; Professor Xin-Wei Han, Department of Radiology, The First Affiliated Hospital, Zhengzhou University, Zhengzhou, Henan Province, China; and Professor Anren Kuang, Department of Nuclear Medicine, Huaxi Hospital, Sichuan University, Chengdu, Sichuan Province, China.

Abstract

There are unstructured abstracts (no more than 256 words) and structured abstracts (no more than 480). The specific requirements for structured abstracts are as follows:

An informative, structured abstracts of no more than 480 words should accompany each manuscript. Abstracts for original contributions should be structured into the following sections. AIM (no more than 20 words): Only the purpose should be included. Please write the aim as the form of "To investigate/study/…; MATERIALS AND METHODS (no more than 140 words); RESULTS (no more than 294 words): You should present *P* values where appropriate and must provide relevant data to illustrate how they were obtained, e.g. 6.92 ± 3.86 *vs* 3.61 ± 1.67, $P < 0.001$; CONCLUSION (no more than 26 words).

Key words

Please list 5-10 key words, selected mainly from *Index Medicus*, which reflect the content of the study.

Text

For articles of these sections, original articles and brief articles, the main text should be structured into the following sections: INTRODUCTION, MATERIALS AND METHODS, RESULTS and DISCUSSION, and should include appropriate Figures and Tables. Data should be presented in the main text or in Figures and Tables, but not in both. The main text format of these sections, editorial, topic highlight, case report, letters to the editors, can be found at: http://www.wjgnet.com/1949-8470/g_info_20100313183720.htm.

Illustrations

Figures should be numbered as 1, 2, 3, *etc*., and mentioned clearly in the main text. Provide a brief title for each figure on a separate page. Detailed legends should not be provided under the figures. This part should be added into the text where the figures are applicable. Figures should be either Photoshop or Illustrator files (in tiff, eps, jpeg formats) at high-resolution. Examples can be found at: http://www.wjgnet.com/1007-9327/13/4520.pdf; http://www.wjgnet.com/1007-9327/13/4554.pdf; http://www.wjgnet.com/1007-9327/13/4891.pdf; http://www.wjgnet.com/1007-9327/13/4986.pdf; http://www.wjgnet.com/1007-9327/13/4498.pdf. Keeping all elements compiled is necessary in line-art image. Scale bars should be used rather than magnification factors, with the length of the bar defined in the legend rather than on the bar itself. File names should identify the figure and panel. Avoid layering type directly over shaded or textured areas. Please use uniform legends for the same subjects. For example: Figure 1 Pathological changes in atrophic gastritis after treatment. A: ...; B: ...; C: ...; D: ...; E: ...; F: ...; G: …*etc*. It is our principle to publish high resolution-figures for the printed and E-versions.

Tables

Three-line tables should be numbered 1, 2, 3, *etc*., and mentioned clearly in the main text. Provide a brief title for each table. Detailed legends should not be included under tables, but rather added into the text where applicable. The information should complement, but not duplicate the text. Use one horizontal line under the title, a second under column heads, and a third below the Table, above any footnotes. Vertical and italic lines should be omitted.

Notes in tables and illustrations

Data that are not statistically significant should not be noted. $^{a}P < 0.05$, $^{b}P < 0.01$ should be noted ($P > 0.05$ should not be noted). If there are other series of *P* values, $^{c}P < 0.05$ and $^{d}P < 0.01$ are used. A third series of *P* values can be expressed as $^{e}P < 0.05$ and $^{f}P < 0.01$. Other notes in tables or under illustrations should be expressed as ^{1}F, ^{2}F, ^{3}F; or sometimes as other symbols with a superscript (Arabic numerals) in the upper left corner. In a multi-curve illustration, each curve should be labeled with ●, ○, ■, □, ▲, △, *etc*., in a certain sequence.

Acknowledgments

Brief acknowledgments of persons who have made genuine contributions to the manuscript and who endorse the data and conclusions should be included. Authors are responsible for obtaining written permission to use any copyrighted text and/or illustrations.

REFERENCES

Coding system

The author should number the references in Arabic numerals ac-

cording to the citation order in the text. Put reference numbers in square brackets in superscript at the end of citation content or after the cited author's name. For citation content which is part of the narration, the coding number and square brackets should be typeset normally. For example, "Crohn's disease (CD) is associated with increased intestinal permeability[1,2]". If references are cited directly in the text, they should be put together within the text, for example, "From references[19,22-24], we know that..."

When the authors write the references, please ensure that the order in text is the same as in the references section, and also ensure the spelling accuracy of the first author's name. Do not list the same citation twice.

PMID and DOI

Pleased provide PubMed citation numbers to the reference list, e.g. PMID and DOI, which can be found at http://www.ncbi.nlm.nih.gov/sites/entrez?db=pubmed and http://www.crossref.org/SimpleTextQuery/, respectively. The numbers will be used in E-version of this journal.

Style for journal references

Authors: the name of the first author should be typed in bold-faced letters. The family name of all authors should be typed with the initial letter capitalized, followed by their abbreviated first and middle initials. (For example, Lian-Sheng Ma is abbreviated as Ma LS, Bo-Rong Pan as Pan BR). The title of the cited article and italicized journal title (journal title should be in its abbreviated form as shown in PubMed), publication date, volume number (in black), start page, and end page [PMID: 11819634 DOI: 10.3748/wjg.13.5396].

Style for book references

Authors: the name of the first author should be typed in bold-faced letters. The surname of all authors should be typed with the initial letter capitalized, followed by their abbreviated middle and first initials. (For example, Lian-Sheng Ma is abbreviated as Ma LS, Bo-Rong Pan as Pan BR) Book title. Publication number. Publication place: Publication press, Year: start page and end page.

Format

Journals

English journal article (list all authors and include the PMID where applicable)

1 **Jung EM**, Clevert DA, Schreyer AG, Schmitt S, Rennert J, Kubale R, Feuerbach S, Jung F. Evaluation of quantitative contrast harmonic imaging to assess malignancy of liver tumors: A prospective controlled two-center study. *World J Gastroenterol* 2007; **13**: 6356-6364 [PMID: 18081224 DOI: 10.3748/wjg.13.6356]

Chinese journal article (list all authors and include the PMID where applicable)

2 **Lin GZ**, Wang XZ, Wang P, Lin J, Yang FD. Immunologic effect of Jianpi Yishen decoction in treatment of Pixu-diarrhoea. *Shijie Huaren Xiaohua Zazhi* 1999; **7**: 285-287

In press

3 **Tian D**, Araki H, Stahl E, Bergelson J, Kreitman M. Signature of balancing selection in Arabidopsis. *Proc Natl Acad Sci USA* 2006; In press

Organization as author

4 **Diabetes Prevention Program Research Group**. Hypertension, insulin, and proinsulin in participants with impaired glucose tolerance. *Hypertension* 2002; **40**: 679-686 [PMID: 12411462 PMCID:2516377 DOI:10.1161/01.HYP.0000035706.28494.09]

Both personal authors and an organization as author

5 **Vallancien G**, Emberton M, Harving N, van Moorselaar RJ; Alf-One Study Group. Sexual dysfunction in 1, 274 European men suffering from lower urinary tract symptoms. *J Urol* 2003; **169**: 2257-2261 [PMID: 12771764 DOI:10.1097/01.ju.0000067940.76090.73]

No author given

6 21st century heart solution may have a sting in the tail. *BMJ* 2002; **325**: 184 [PMID: 12142303 DOI:10.1136/bmj.325.7357.184]

Volume with supplement

7 **Geraud G**, Spierings EL, Keywood C. Tolerability and safety of frovatriptan with short- and long-term use for treatment of migraine and in comparison with sumatriptan. *Headache* 2002; **42** Suppl 2: S93-99 [PMID: 12028325 DOI:10.1046/j.1526-4610.42.s2.7.x]

Issue with no volume

8 **Banit DM**, Kaufer H, Hartford JM. Intraoperative frozen section analysis in revision total joint arthroplasty. *Clin Orthop Relat Res* 2002; (**401**): 230-238 [PMID: 12151900 DOI:10.1097/00003086-200208000-00026]

No volume or issue

9 Outreach: Bringing HIV-positive individuals into care. *HRSA Careaction* 2002; 1-6 [PMID: 12154804]

Books

Personal author(s)

10 **Sherlock S**, Dooley J. Diseases of the liver and billiary system. 9th ed. Oxford: Blackwell Sci Pub, 1993: 258-296

Chapter in a book (list all authors)

11 **Lam SK**. Academic investigator's perspectives of medical treatment for peptic ulcer. In: Swabb EA, Azabo S. Ulcer disease: investigation and basis for therapy. New York: Marcel Dekker, 1991: 431-450

Author(s) and editor(s)

12 **Breedlove GK**, Schorfheide AM. Adolescent pregnancy. 2nd ed. Wieczorek RR, editor. White Plains (NY): March of Dimes Education Services, 2001: 20-34

Conference proceedings

13 **Harnden P**, Joffe JK, Jones WG, editors. Germ cell tumours V. Proceedings of the 5th Germ cell tumours Conference; 2001 Sep 13-15; Leeds, UK. New York: Springer, 2002: 30-56

Conference paper

14 **Christensen S**, Oppacher F. An analysis of Koza's computational effort statistic for genetic programming. In: Foster JA, Lutton E, Miller J, Ryan C, Tettamanzi AG, editors. Genetic programming. EuroGP 2002: Proceedings of the 5th European Conference on Genetic Programming; 2002 Apr 3-5; Kinsdale, Ireland. Berlin: Springer, 2002: 182-191

Electronic journal (list all authors)

15 Morse SS. Factors in the emergence of infectious diseases. Emerg Infect Dis serial online, 1995-01-03, cited 1996-06-05; 1(1): 24 screens. Available from: URL: http://www.cdc.gov/ncidod/eid/index.htm

Patent (list all authors)

16 **Pagedas AC**, inventor; Ancel Surgical R&D Inc., assignee. Flexible endoscopic grasping and cutting device and positioning tool assembly. United States patent US 20020103498. 2002 Aug 1

Statistical data

Write as mean ± SD or mean ± SE.

Statistical expression

Express *t* test as *t* (in italics), *F* test as *F* (in italics), chi square test as χ^2 (in Greek), related coefficient as *r* (in italics), degree of freedom as υ (in Greek), sample number as *n* (in italics), and probability as *P* (in italics).

Units

Use SI units. For example: body mass, m (B) = 78 kg; blood pressure, p (B) = 16.2/12.3 kPa; incubation time, t (incubation) = 96 h, blood glucose concentration, c (glucose) 6.4 ± 2.1 mmol/L; blood CEA mass concentration, p (CEA) = 8.6 24.5 μg/L; CO_2 volume fraction, 50 mL/L CO_2, not 5% CO_2; likewise for 40 g/L formaldehyde, not 10% formalin; and mass fraction, 8 ng/g, *etc.* Arabic numerals such as 23, 243, 641 should be read 23 243 641.

The format for how to accurately write common units and quantums can be found at: http://www.wjgnet.com/1949-8470/g_info_20100313185816.htm.

Abbreviations

Standard abbreviations should be defined in the abstract and on first mention in the text. In general, terms should not be abbreviated unless they are used repeatedly and the abbreviation is helpful to the reader. Permissible abbreviations are listed in Units, Symbols and Abbreviations: A Guide for Biological and Medical Editors and Authors (Ed. Baron DN, 1988) published by The Royal Society of Medicine, London. Certain commonly used abbreviations, such as DNA, RNA, HIV, LD50, PCR, HBV, ECG, WBC, RBC, CT, ESR, CSF, IgG, ELISA, PBS, ATP, EDTA, mAb, can be used directly without further explanation.

Italics

Quantities: *t* time or temperature, *c* concentration, *A* area, *l* length, *m* mass, *V* volume.
Genotypes: *gyrA*, *arg* 1, *c myc*, *c fos*, *etc.*
Restriction enzymes: *Eco*RI, *Hin*dI, *Bam*HI, *Kbo* I, *Kpn* I, *etc.*
Biology: *H. pylori*, *E coli*, *etc.*

Examples for paper writing

Editorial: http://www.wjgnet.com/1949-8470/g_info_20100313182341.htm

Frontier: http://www.wjgnet.com/1949-8470/g_info_20100313182448.htm

Topic highlight: http://www.wjgnet.com/1949-8470/g_info_20100313182639.htm

Observation: http://www.wjgnet.com/1949-8470/g_info_20100313182834.htm

Guidelines for basic research: http://www.wjgnet.com/1949-8470/g_info_20100313183057.htm

Guidelines for clinical practice: http://www.wjgnet.com/1949-8470/g_info_20100313183238.htm

Review: http://www.wjgnet.com/1949-8470/g_info_20100313183433.htm

Original articles: http://www.wjgnet.com/1949-8470/g_info_20100313183720.htm

Brief articles: http://www.wjgnet.com/1949-8470/g_info_20100313184005.htm

Case report: http://www.wjgnet.com/1949-8470/g_info_20100313184149.htm

Letters to the editor: http://www.wjgnet.com/1949-8470/g_info_20100313184410.htm

Book reviews: http://www.wjgnet.com/1949-8470/g_info_20100313184803.htm

Guidelines: http://www.wjgnet.com/1949-8470/g_info_20100313185047.htm

SUBMISSION OF THE REVISED MANUSCRIPTS AFTER ACCEPTED

Please revise your article according to the revision policies of *WJR*. The revised version including manuscript and high-resolution image figures (if any) should be re-submited online (http://www.wjgnet.com/1949-8470office/). The author should send the copyright transfer letter, responses to the reviewers, English language Grade B certificate (for non-native speakers of English) and final manuscript checklist to wjr@wjgnet.com.

Language evaluation

The language of a manuscript will be graded before it is sent for revision. (1) Grade A: priority publishing; (2) Grade B: minor language polishing; (3) Grade C: a great deal of language polishing needed; and (4) Grade D: rejected. Revised articles should reach Grade A or B.

Copyright assignment form

Please download a Copyright assignment form from http://www.wjgnet.com/1949-8470/g_info_20100313185522.htm.

Responses to reviewers

Please revise your article according to the comments/suggestions provided by the reviewers. The format for responses to the reviewers' comments can be found at: http://www.wjgnet.com/1949-8470/g_info_20100313185358.htm.

Proof of financial support

For paper supported by a foundation, authors should provide a copy of the document and serial number of the foundation.

Links to documents related to the manuscript

WJR will be initiating a platform to promote dynamic interactions between the editors, peer reviewers, readers and authors. After a manuscript is published online, links to the PDF version of the submitted manuscript, the peer-reviewers' report and the revised manuscript will be put on-line. Readers can make comments on the peer reviewer's report, authors' responses to peer reviewers, and the revised manuscript. We hope that authors will benefit from this feedback and be able to revise the manuscript accordingly in a timely manner.

Science news releases

Authors of accepted manuscripts are suggested to write a science news item to promote their articles. The news will be released rapidly at EurekAlert/AAAS (http://www.eurekalert.org). The title for news items should be less than 90 characters; the summary should be less than 75 words; and main body less than 500 words. Science news items should be lawful, ethical, and strictly based on your original content with an attractive title and interesting pictures.

Publication fee

WJR is an international, peer-reviewed, Open-Access, online journal. Articles published by this journal are distributed under the terms of the Creative Commons Attribution Non-commercial License, which permits use, distribution, and reproduction in any medium, provided the original work is properly cited, the use is non commercial and is otherwise in compliance with the license. Authors of accepted articles must pay a publication fee. The related standards are as follows. Publication fee: 1300 USD per article; Reprints fee: 350 USD per 100 reprints, including postage cost. Editorial, topic highlights, book reviews and letters to the editor are published free of charge.